

© [2020]

PENGFEE XIE

ALL RIGHTS RESERVED

LABEL-FREE ELECTRONIC DETECTION OF BIOMARKERS
USING NANOWELL IMPEDANCE SENSOR

By

PENGFEEI XIE

A dissertation submitted to the

School of Graduate Studies

Rutgers, The State University of New Jersey

In partial fulfillment of the requirements

For the degree of

Doctor of Philosophy

Graduate Program in Electrical and Computer Engineering

Written under the direction of

Dr. Mehdi Javanmard

And approved by

New Brunswick, New Jersey

October, 2020

ABSTRACT OF THE DISSERTATION

Label-free Electronic Detection and Quantification of Biomarkers Using Nanowell Impedance Sensor

By Pengfei Xie

Dissertation Director: Dr. Mehdi Javanmard

The application of lab-on-a-chip or microfluidic technologies to perform protein assays is an emerging field and has the potential to be used for point-of-care devices. High-sensitivity and general-use biosensors play a crucial role in achieving this goal. The quantification of protein provides a crucial perspective of pathology, drug treatment, and understanding of the disease.

Label-free electronic affinity-based immunosensing is an attractive candidate as a platform technology for analyzing biomarkers due to the ease of miniaturization and the minimal use of reagents. Electronic-based sensing approaches, however, have lagged behind their optical counterparts in terms of detection limit, selectivity, and reliability. In addition, the matrix-dependent nature of electronic sensing modalities makes the analysis of biomarkers in high salt concentration samples, such as the serum, difficult due to charge screening.

In this dissertation, I present a novel impedance-based nanowell biosensor and its application in multiple novel solutions for detecting protein biomarkers in purified

buffers and serum matrixes using a micro-sized biochip. I discuss sensor fabrication, sample preparation, theoretical considerations, data analysis, and various experiments.

In the first chapter, I introduce the fundamental perspective of protein studies and protein quantification and summarize and review the gold standard and state-of-the-art techniques of protein quantification. Next, I introduce the impedance-based biosensors used in protein detection. In the second chapter, I introduce the theory and modeling of the proposed nanowell sensor, including the systematic analysis, determination of the parameters, results of the simulations, and the derivation of the formula. In the third chapter, I propose the nanowell-based label-free assay for the quantitative assessment of cytokine levels, present the results of a series of experiments, and discuss the validity and novelty of the technique. In the fourth chapter, I present multiplexed protein assay measurements achieved using an embedded microprocessor. The standard titration curves of multiple proteins are also presented, followed by the correlation analysis between the nanowell sensor and the Luminex technique and the results of the nanowell sensor to the characteristic biological parameters. In the fifth chapter, I present the most recent results on the analysis of mouse clinical samples with inflammatory arthritis. The results of different experiments with different treatments, a comparison between the standard titration curves of different techniques, and the correlation curves of all samples are presented in this chapter. And in the sixth chapter, the results of human clinical samples including the titration curve of different biomarkers, cytokine levels of different patient samples were introduced.

Keywords:

Biosensing, protein assay, label-free detection, impedance sensor, biomarker detection

ACKNOWLEDGEMENT:

I would like to extend my sincere and heartfelt thanks to all those who have helped me in this endeavor. Without their advice, guidance, help, and cooperation I would not have completed this dissertation.

I am deeply indebted to my academic advisor Dr. Mehdi Javanmard for all his valuable advice, encouragement, and discussions not only regarding specific academic problems but also academic spirit, attitude, and life.

I am extremely thankful to all the committee members involved in the different stages of this dissertation—Dr. Mark Allen, Dr. Michael Wu, Dr. Umer Hassan, Dr. Yicheng Lu, Dr. Manish Chhowalla, Dr. Laleh Najafizadeh, and Dr. Michael Caggiano. I am extremely grateful for their insightful advice and guidance regarding my research.

I extend my gratitude to the Electrical Engineering department at Rutgers University for providing me the opportunity to complete the Ph.D. program and for all the help during this long journey. I also wish to thank my parents and all my family members who have always supported and encouraged me.

Last but not least, thanks go to all my friends and colleagues who directly or indirectly helped me to complete this degree.

Any omission in this brief statement of acknowledgment does not mean a lack of gratitude.

Thank you!

Table of Contents

Abstract	ii
Acknowledgments.....	v
Table of Contents	vi
List of Figures	viii
Chapter 1: Introduction	1
1.1. Protein and its functions	1
1.2. Protein study types and objectives	2
1.3. Current protein detection techniques	4
1.4. Impedance based biosensors used in protein detections	12
Chapter 2: Nanowell impedance sensor modeling	15
2.1. Introduction of modeling of impedance sensor	15
2.2. Modeling of nanowell impedance sensor	15
2.3. Results of modeling of nanowell sensor	24
Chapter 3: Label-free Assay for Quantitatively Assessment of Cytokine levels	28
3.1. Introduction	28
3.2. Nanowell Array Impedance Sensor	32

3.3. Materials and Methods	34
3.4. Results and Discussion	38
3.5	
Conclusion	48
Chapter 4: Multiplexed protein assay measurements with embedded micro-processor	50
4.1. Introduction	50
4.2. Material and Methods	54
4.3. Results and Discussion	58
4.4. Conclusion	67
Chapter 5: Quantification of mouse clinical samples with rheumatoid arthritis	69
5.1. Introduction	69
5.2. Standard titration curve of mouse cytokines IL6, TNF- α , and IL10.....	71
5.3. Study of Clinical sample of the mouse with rheumatoid arthritis	74
5.4.	
Conclusion	81
Chapter 6: Quantification of human clinical samples with inflammatory arthritis	83
6.1. Introduction	83
6.2. Modeling and standard titration curve	84

6.3. Quantification of cytokine level with human samples	93
6.4. Conclusion	97
Chapter 7: Conclusion and Future works	99
References	100

List of Figures

Figure 2-1) Equivalent circuit model of nanowell device	16
Figure 2-2) COMSOL simulation results of the normalized electrical field of nanowell sensor	18
Figure 2-3) Impedance Spectrum information of nanowell model	19
Figure 2-4) Binding site number on sensor surface at different bulk concentration	24
Figure 2-5) Resistance change of nanowell sensor at different bulk concentration of IL6	25
Figure 2-6) Resistance change of nanowell sensor at different bulk concentration of TNF- α	25
Figure 2-7) Resistance change of nanowell sensor at different well size	26
Figure 3-1) Nanowell Array Label-free Impedance sensor schematic	33
Figure 3-2) Measurement setup using lock-in-amplifier	34

Figure 3-3) Microscopic images of micro-fabricated sensors of differing sizes and array size and density. A) 9 well and B) 144 well array device	35
Figure 3-4) Magnitude and Phase of Impedance spectrum of device. Device starts out capacitive at low frequencies and response becomes dominated by solution resistance as frequency is increased beyond 100 KHZ	36
Figure 3-5) Real component and imaginary component of device impedance	37
Figure 3-6) Output voltage of lock-in amplifier as PBS is added to an empty channel	39
Figure 3-7) Output voltage of lock-in amplifier as blank PBS is added (negative control)	39
Figure 3-8) Output current of lock-in amplifier as adsorption of IgG to sensor surface	40
Figure 3-9) Input current of lock-in amplifier as binding of leptin to anti-leptin IgG	41
Figure 3-10) Output voltage of lock-in amplifier as extra antibodies removed from well	42
Figure 3-11) Output voltage of lock-in amplifier as PBS re-injected	42
Figure 3-12) Input current of lock-in amplifier as blank PBS injected as negative control	43
Figure 3-13) Output voltage of lock-in amplifier as non-target cytokine injected (negative control)	44

Figure 3-14) Illustration of experimental protocol for device validation and resulting percentage changes in impedance. Antibody adsorption and protein binding inside well results in decrease in impedance. Negative control steps (adding blank samples or non-targeted protein) results in positive change in current	44
Figure 3-15) Relationship between sensor response to protein binding and well diameter (Left) measured in triplicate over 3 different well sizes and (Right) the current across the electrodes verses time for 2 μm , 3 μm , and 4 μm diameter wells	45
Figure 3-16) Sensor response to the sample spiked with i) target protein (TNF- α) at 1 pM and non-target proteins (IL6 and IL4) at 1 nM and ii) Negative control (serum spiked with non-target protein 1nM of IL6 an TNF- α)	47
Figure 3-17) Titration curve for concentrations ranging from 60 pM to 6 fM	48
Figure 4-1) Nanowell Array Label-free Impedance sensor schematic	52
Figure 4-2) Nanowell Array Label-free Impedance sensor with antibodies and proteins	53
Figure 4-3) Nanowell Sensor Array photo	54
Figure 4-4) Device Sensor photo of 5*5 nanowells	54
Figure 4-5) Normalized impedance measured using lock-in amplifier as adsorption of IL6 antibody to sensor surface	58
Figure 4-6) Normalized impedance measured using lock-in amplifier as binding of IL6 to IL6 antibodies	59

Figure 4-7) Input current of lock-in amplifier as the buffer without target cytokines	59
Figure 4-8) Impedance data measured by lock-in amplifier of multiple target proteins. A) TNF- α , B) IL6, C) IL4, and D) Comparison among the listed 3 proteins	60
Figure 4-9) Titration curve of multiple proteins with comparison of nanowell sensor and Luminex. A) TNF- α , B) IL6, and C) IL4	62
Figure 4-10) Regression models of multiple proteins from 1 pg/ml to 10 ng/ml. A) TNF- α , B) IL6, and C) IL4	63
Figure 4-11) Output voltage of lock-in amplifier as the protein injected during the whole experiment process. A) TNF- α , B) IL6, and C) IL4.....	65
Figure 4-12) Temporal cytokine profiling with embedded computer controlled 7 sensors array	67
Figure 5-1) Output voltage response to different concentration of mouse IL6 samples. A) 1 nM, B) 100 pM, C) 10 pM, D) 1 pM, E) 100 nM, and F) 10 nM	72
Figure 5-2) Titration curve of mouse IL6	73
Figure 5-3) Titration curve of mouse TNF- α	73
Figure 5-4) Titration curve of mouse IL10	73
Figure 5-5) Regression model curve of mouse IL6 with A) Nanowell and B) Luminex.....	75
Figure 5-6) Regression model curve of mouse TNF- α with A) Nanowell and B) Luminex	76

Figure 5-7) Regression model curve of mouse IL10 A) Nanowell and B) Luminex	77
Figure 5-8) Correlation curve between predicted concentration with nanowell sensor and with Luminex	79
Figure 5-9) Comparison between prediction of standard concentration sample using nanowell sensor and Luminex	79
Figure 5-10) Response of nanowell sensor wrt ankle thickness of clinical mouse samples	80
Figure 5-11) Response of nanowell sensor wrt clinical score of clinical mouse samples	81
Figure 6-1) Titration curves of human TNF- α with nanowell sensor and Luminex	84
Figure 6-2) Titration curves of human IL6 with nanowell sensor and Luminex	85
Figure 6-3) Titration curves of human IL10 with nanowell sensor and Luminex	85
Figure 6-4) regression model curve of TNF- α with nanowell sensor	87
Figure 6-5) regression model curve of TNF- α with Luminex	88
Figure 6-6) regression model curve of IL6 with nanowell sensor	89
Figure 6-7) regression model curve of IL6 with Luminex	89
Figure 6-8) regression model curve of IL10 with nanowell sensor	90
Figure 6-9) regression model curve of IL10 with Luminex	91
Figure 6-10) Prediction of standard concentration sample of TNF- α	91

Figure 6-11) Prediction of standard concentration sample of IL6	92
Figure 6-12) Prediction of standard concentration sample of IL10	92
Figure 6-13) Representative results of all 3 proteins of single patient	93
Figure 6-14) Comparison of nanowell sensor and Luminex	94
Figure 6-15) Comparison of TNF- α concentration of stim and sham group	94
Figure 6-16) Comparison of IL6 concentration of stim and sham group	95
Figure 6-17) Comparison of IL10 concentration of stim and sham group	95
Figure 6-18) Correlation between nanowell sensor and Luminex of TNF- α	96
Figure 6-19) Correlation between nanowell sensor and Luminex of IL6	96
Figure 6-20) Correlation between nanowell sensor and Luminex of IL10	97

Chapter 1: Introduction

1.1 Protein and its functions

Proteins perform a massive array of functions at intervals organisms, as well as catalyzing metabolic reactions [1][2], responding to stimuli [3], providing structure to cells and organisms, and transporting molecules from one location to a different. Any listing of major analysis topics in biology, like DNA replication [4], transcription [5], translation [6], splicing [7], secretion [8], cell cycle control [9], signal transduction [10], and intermediary metabolism, is additionally a list of processes during which macromolecule complexes are involved as essential parts. The protein, the overall macromolecule content of 1 specific biological system, is extremely dynamic and is continually dynamical in step with completely different stimuli [11][12]. Proteomics includes the structural and purposeful data of proteins, however additionally the quantification of their abundance[13], the research of their modifications [14], the interactions between them [15], and the study of their localization [16]. Throughout the numerous stages of disease diagnosis and the purpose of point to care, proteins will act as ideal indicators [17]. Protein analysis may be applied for the systematic look for new marker proteins and peptides, so fast the event of assays may be vital support [18]. Subsequently, accurate and reliable analytical methodologies may be developed and valid to discover the antecedently known marker proteins/peptides. Protein studies are the cornerstone of the understanding the pathology behind it and one of the most effective methods.

1.2 Protein study types and objectives

Depending on the final objective, most proteomic studies will be divided into 3 completely different areas, which are qualitative proteomics (protein characterization and identification), differential/quantitative proteomics, and functional proteomics [19][20]. The goal of qualitative proteomics is to spot and characterize the entire set of proteins present in an experimental sample, which might include the characterization of the macromolecule post-translational modifications (PTMs). This systematic investigation will be centered on an entire protein (e.g., all the proteins comprising a sample) [21], or on a selected set of the proteins (e.g., sarcoplasmic proteins [22]; gluten proteins [23]; glycosylated proteins [24]). The two commonest approaches for macromolecule identification are peptide mass fingerprinting (PMF) and protein mass fingerprinting (PMF), each of which needs enzymatic digestion of the studied proteins [25][26]. For all such approaches, the presence within the database of the sequence information of the corresponding macromolecule, or a homologous one, is needed. The huge array of various samples is probably going to end in the absence of the many peptides/proteins in current databases. Intentional caution and scrutiny are usually needed, even once operating with easy samples. Meanwhile, PTMs play an important role, as they affect protein activity and stability [27]. PTMs will occur along with a wide range of biological signals. More than 300 different types of PTMs are known; however, but solely some are being extensively investigated, such as phosphorylation, acetylation, glycosylation, and oxidation, which also brings challenges to the study [28]. Quantitative information at the protein level, such as the relative abundance of some certain proteins between different samples or the absolute

level of a protein can be very helpful once studying for variations between completely different conditions. Relative quantification can be achieved with different methodologies, which can be classified as gel-based, label-based, and label-free [29]. Gel-based methods include the separation of proteins by two-dimensional electrophoresis and the comparison of protein abundance determined as the spot volume between different samples [30]. Every sample being compared will be run on a distinct gel, or as an alternative, up to a few samples will be differentially labeled and run on identical gel exploitation distinction gel electrophoresis technology, therefore increasing confidence within the detection and quantification of variations in protein abundance [31]. Within the label-based strategies, proteins or peptides are antecedently labeled with a mass tag, and relative quantification is then obtained from the Mass Spectroscopy or MS/MS read-outs. In label-free approaches, the macromolecule quantity is mostly calculated supported the MS extracted ion current signal of the peptides/proteins throughout liquid chromatography (LC) run [32]. Quantitative proteomic methodologies are greatly improved with the introduction of select reaction observation (SRM) experiments, a sensitive LC-MS/MS acquisition mode usually employed in medical analysis to verify and validate candidate biomarker proteins [33].

Functional proteomics studies the useful interaction between proteins or between a protein and different molecules and also the consequences of these interactions. There also are an outsized variety of transient protein-protein interactions, that successively management an outsized variety of cellular processes. All modifications of proteins essentially involve such transient protein-protein interactions. These embody the

interactions of protein kinases, protein phosphatases, glycosyltransferases, acyl group transferases, proteases, etc. with their substrate proteins.

Protein-protein interactions have a large variety of measurable effects. First, they will alter the kinetic properties of proteins, which may be reflected within the altered binding of substrates and altered chemical catalysis. Second, protein-protein interactions are the most common mechanism to permit substrate channeling. Several similar samples of metabolic channeling are incontestable both between different subunits of a complex and between different domains of a single multifunctional polypeptide. Third, protein-protein interactions may result in the formation of a replacement binding web site. Fourth, protein-protein interactions will inactivate a protein. Fifth, protein-protein interactions will modification the specificity of a protein for its substrate.

1.3 Current protein detection techniques

Proteins act as mediators and modulators at intervals extremely localized environments and regulate immunologic responses, hemopoietic development, cell-to-cell communication, host responses to infectious agents, and inflammatory stimuli [34]. They interact with each other in advanced ways in which could also be additive, synergistic, or antagonistic or which will involve the induction of one by the others. The physiological effects of cytokines usually depend upon the relative concentrations of many proteins. This illustrates the importance of recognizing that proteins influence physiology via networks. Elevated concentrations of proteins indicate activation of protein pathways related to inflammation or disease

progression. Therefore, amount measurements are vital, as these proteins are widely used as biomarkers to know and predict disease progression and monitor the results of treatment. Thus, the determination of their concentration is of explicit interest [35].

The selection of the proper protein detection technique is extremely necessary because the measurements might have to live quantitative changes in expression levels in biological samples. Ideally, the detection limit ought to be as low as potential with associated best signal/noise. For correct quantification of proteins in typical proteomics samples, the detection technique ought to have a wide dynamic range and the linear relationship among the number of proteins and also the staining intensity. The procedure ought to be straightforward and quick, non-toxic, environmentally friendly, and not too pricey.

To date, dozens of exciting protein microarrays are studied. They'll be classified into two main regimes, labeled and label-free. Every regime has its advantages and downsides. In this paper, we tend to target 5 candidate label detection strategies, namely, fluorescent labeling [36], isotopic labeling [37], chemiluminescent labeling [38], electrochemically active probe labeling [39], and nanoparticle labeling [40], and five candidate label-free detection methods, namely, mass spectrometry (MS) [41], microcantilevers [42], quartz-crystal microbalance (QCM) [43], surface plasmon resonance (SPR) and localized surface plasmon resonance (LSPR) [44][45], and anomalous reflections of the gold surface (AR) [46]. The features of the different methods concerning their availability for protein microarrays are summarized and introduced below.

1.3.1 Labeled microarray techniques

A label is typically described as any foreign molecule with chemicals or temporarily attached to the molecule of interest to observe molecular presence or activity, which might probably alter its intrinsic properties. It needs a labeling method as a preparation step that's sometimes low yield, combining synthesis and purification. Covalent bonding is usually the principal method of fluorescent, chemiluminescent, and NP labeling, which is realized through coupling chemistries, whereas some electrochemically active probe labeling needs solely temporary attachment of intermolecular bonding. Isotopic labeling implies the identical elements but with different neutron numbers, being incorporated into target molecules to lead to a detectable distinction. Fluorescent label detection strategies provide the foremost common and convenient techniques to transmit info from the events that happened at the molecule level. Light probes are stable, simply manipulated, and provide sensible sensitivity and resolution. These are particularly necessary once incorporated into microarray technology. Though perturbations in molecular interactions caused by label molecules will result in false-positive signals, massive amounts of information produced from high-throughput studies may be subjected to statistical data-mining processes which will increase analytical accuracy. In the AN protein sandwich assay system, a fluorescein molecule is employed as a secondary protein label. With this method, one will omit an instantaneous non-native result on the molecule of interest. One of the earliest strategies for molecular detection is the utilization of radioisotopes that perform accurate quantification of protein abundance. Though radioactivity is additionally appropriate for analyzing protein activity, significantly for enzymatic phosphorylation because of sensitivity and specificity, and therefore the chance of

fluorescence detection, the utilization of isotope-labeled molecules raises some safety issues. Therefore, within the long-term, these strategies aren't possible to be adopted for a broad vary of biochemistry experiments.

Chemiluminescence is another fast-developing technique, which is informative to convert molecular interactions into quantitatively color info. Utilizing its energy from exoergic reactions, totally different wavelengths are emitted throughout molecular relaxation to its ground state depending on the quantity of energy absorbed (e.g., 150 kJ/mol for the red light, 300 kJ/mol for blue light). A successful demonstration of the detection of tiny and large molecules simultaneously using a microarray immunoassay is also reported. The chemiluminescence signal was amplified employing a poly-horseradish peroxidase complex (polyHRP), leading to low detection limits, microgram, or sub microgram levels for each tiny (<1 kDa) and huge (>10 kDa) molecules. Chemiluminescent probes integrated with a microarray provide an advantage in high sensitivity and an up to 6 orders of magnitude dynamic range of. However, the quantum yield of chemiluminescent probes is less than 1% because of inefficiency within the chemical reaction or poor energy transfer.

The sensing of electrochemical signals originating from molecular surface charges has been reported for high-throughput studies. This detection technique is especially engaging due to its sensitivity and repeatability and because it can be easily miniaturized. The Leiber group has pioneered the multiplex detection of prostate-specific antigen (PSA), PSA-1-anti-chymotrypsin, carcinoembryonic antigen, and mucin-1 (all are cancer biomarkers) at femtomolar concentrations using field-effect transistor (FET) nanowire sensors. Esfandyarpour et al. measured changes in

impedance using nanoneedle sensing electrodes to detect the abundance of charged protein (streptavidin) at single nM concentration.

The use of NPs (Nano-Particles) or metal nanoclusters in molecular detection is sometimes considered as label-free detection methods. However, NPs <10 nm are considered to be probes that assist in molecular detection. The target protein is bound with the NP beforehand, and on molecular interaction events, signal monitoring is dependent on the NP signal. Thus, such small NPs research falls into another class of (macro-) label detection. It is reported that 1.4 nm gold NP probes that were covalently attached to antibodies improved immunodetection. Direct molecular absorption to NPs may induce some molecular distortion that modifies its intrinsic function. In certain cases, a self-assembled monolayer with a suitable functional group is used as a bio-interfacial surface to reduce this effect.

1.3.2 Label-free microarray techniques

Another regime of protein detection techniques is label-free microarrays. Label-free detection only utilizes molecular biophysical properties and molecular charge to detect molecular quantity or activity. Mass Spectroscopy and microcantilever technique utilize the relative molecular mass, SPR, and AR techniques are based on the refractive index. Moreover, these techniques are often utilized to track molecular events during a period manner. During a typical biosensing process, molecular interactions are transduced as mechanical, electrical, or optical signals and are therefore detectable with none label probes. the most advantage of label-free detection is that additional distractive info is avoided because the methods use solely native proteins and ligands.

Mass spectrometry enables us to directly determine the type of proteins of interest using molecular mass or mass ratio once tryptic digestion. However, typical MS has some disadvantages and low throughput. Surface-enhanced laser desorption/ionization (SELDI) TOF-MS is an innovative approach that provides on-chip purification of the proteins of interest and later ionization of the preserved molecules to be detected. SELDI-TOF-MS has been utilized to contribute to the discovery of tumor biomarkers, plant phosphoproteome, and applied to the detection of various proteins in a single chip format. Some studies analyzed enzymatic glycosylation on a centimeter scale microchip comprising an array of more than a dozen peptide spots, and some others also detected the binding of carbonic anhydrase to a benzenesulfonamide ligand as well as the binding of glutathione S-transferase-tagged protein complexes to a glutathione ligand. Many disease-specific marker proteins in clinical biological samples were successfully identified: amyloid β -peptides, rat plasma profiling for biomarker discovery, downregulated biomarker identification, and liver cirrhosis of the liver protein classification. A minimum of two major limitations to the system is, a large and complicated setup, and a calibration curve is important to quantify protein abundance.

Microcantilevers probes were originated from surface characterization in atomic force research. They convert specific biomolecular recognition into nano-mechanical signals, which may be a differential surface stress. Protein interaction causes the cantilever to deform and so interaction will be discovered by observation changes with the cantilevers. The cantilever based assay technique has been applied to DNA-binding proteins, detection of the bioterrorism agent anthrax, to study biomarkers, and

to weigh individual vaccinia viruses and microorganisms. The microcantilever array was developed with the ability of a multichannel measurement method for high-throughput studies assembled with a microfluidic channel. Some studies showed a multiplexed detection of the interactions involving oligonucleotides and antigen-antibody, with a sub-micron spatial resolution device on a chip. At present, many challenges are still to be resolved: (i) integration of cantilever arrays and microfluidic channel networks continues to be underneath development; and (ii) because of the delicate nature of the cantilever, performance variations aren't of a suitable standard for commercialization.

The quartz crystal microbalance technique uses acoustic waves and is considered as a well-established technique for observation mass and film thickness, monitoring molecular adsorption, and discovering surface reactions within the monolayer range via observation of changes in resonant frequency. The effective quartz frequency can modify as substances are adsorbed by the QCM surface (typically a thin gold surface). Because of the piezoelectric principle, this transformation leads to a detectable electric signal. To date, the technique has evidenced valuable for studying surface-related processes in liquids as well as protein adsorption, and numerous biological reactions in the period observation. In contrast to optical techniques, that aren't sensitive to water-associated adsorbable proteins, changes in total coupled mass, such as hydrodynamically coupled water offer the frequency shift of the QCM. A recent extension of the technique shows the simultaneous measurement of energy dissipation and provides new insight into the protein adsorption process. Using QCM, multichannel detection is feasible on a one-chip system.

Surface Plasmon Resonance (SPR) spectroscopy is well-known to allow us to study the kinetics of antigen-antibody, protein-protein, and receptor-ligand interactions in real-time without any labeling molecule. The capture molecules are immobilized on a gold surface and an unlabeled analyte is added. The change in the reflection angle of light indicates the number of target molecules captured on the surfaces. SPR spectroscopy is a versatile tool but enables the analysis of only a few channels in a single experiment. A massive number of samples to have adhered to the gold surfaces of the microassay is usually required for this technique. Very recently, the SPR imaging technique has been rather popular for the detection of molecular interactions in a parallelized fashion. The assay format can be adapted to study hundreds of molecular interactions within a single experiment.

Anomalous reflection (AR) of gold was reported to effectively observe biomolecular interactions. The reductions in reflectivity will considerably change in the range of wavelength of 400-500nm when a molecule layer forms on the gold surface. This enables the detection of molecular interactions by observation for changes in reflectivity. The advantages of the AR technique include, firstly thickness of the dielectric layer on the gold surface is often expected using the transfer matrix technique, therefore enabling quantitative measurement of surface-bound proteins. Secondly, in contrast to plasmon techniques that strictly limit the gold thin-film thickness; the utilization of semi-infinite gold thin-film (practically over 100 nm) is proper for AR detection; Thirdly, it's tolerance in incidence angle, that allows the use of incoherent light source like light-emitting diodes (LEDs); Fourthly, the AR technique doesn't need any complicated optical setup, the miniaturized system is easy

to build; and lastly for microarray functions, the spatial resolution of the AR technique is 10 times smaller than that of SPR. Therefore, the AR technique might offer a promising platform for high-throughput bio-molecular detection. Illumination with LED lights at a certain incidence angle and the direct collection of the reflected light enabled this technique to be the best appropriate for chip-format detection. However, the sensitivity of the technique is about one-tenth that of the SPR technique.

1.4 Impedance based biosensors used in protein detections

Electrical biosensors rely only on the measuring of currents and/or voltages to detect the binding of proteins. Therefore, excludes sensors that need illumination (e.g., SPR or fluorescence), or use mechanical motion (e.g., quartz crystal microbalance or resonant cantilevers), or use magnetic particles, etc. benefits from their low cost, low power, and easy miniaturization, electrical biosensors hold good promise for applications wherever minimizing size and cost is crucial, for example, point-of-care diagnostics and clinical applications.

Electrical biosensors can be categorized as consistent with how the electrical measurement is performed, such as voltammetric, amperometric/coulometric, and electric impedance sensors. Voltammetry and amperometric involve measurement of the current at an electrode as a response of applied electrode-electrolyte voltage, which usually is DC or pseudo-DC and on purpose modification the electrode conditions. In contrast, measuring the electrical impedance of an interface in an AC steady state with constant DC bias conditions is the most common configuration of

impedance biosensors. As mentioned below, most frequently this is often accomplished by imposing a small AC voltage at a specific frequency and measuring the resulting current, the method will be recurrent at several different frequencies. The current-voltage ratio provides the impedance. This approach, called electrochemical impedance spectroscopy (EIS), has been accustomed to study several different electrochemical phenomena over a wide frequency range. If the resistivity of the electrode-solution interface changes once the target analyte is captured by the probe, EIS will be used to observe that resistivity modification. as an alternative, the resistivity or capacitance of the interface could also be measured at some certain frequency. There is no need for special reagents of the impedance measurement, which is amenable to label-free operation as are explained in the latter paragraph. For this review, we tend to define affinity impedance biosensors as techniques for the detection of biological molecules by measurement impedance changes of the capture probe layer.

A closely related however separate category of biosensors operates by field-effect modulation of carriers within a semiconductor due to adjacent charged particles. Ion sensitive field-effect transistors (ISFETs) and other types, such as EnFETs, BioFETs, etc. are the examples with similar principles but different in mechanisms operate in carbon nanotubes (CBTs), electrolyte insulator semiconductor structures, thin-film transistors, and light-sensitive potentiometric sensors. These field-effect sensors depend on the interaction of external charges with carriers that exists in the semiconductor and thus exhibit high sensitivity at low ionic strength where counter ion shielding is reduced, typically explained in a very recent review and proved by

the low salt concentrations often used. Even if the responses of field-effect transistor sensors are often quantified in terms of channel conductance or capacitance of the electrolyte-insulator-semiconductor interface, we tend to limit to cases in which only the impedance of the target biological layer is measured. Some biosensors are also classified as capacitive biosensors, whose measurements are based on the probe insulator semiconductor interfaces, where both inside the semiconductor and also at the intervals would possibly induce the capacitive changes.

Chapter 2: Nanowell impedance sensor modeling

2.1 Introduction to impedance sensor modeling

EIS combines the analysis of both the resistive and capacitive properties of materials based on the perturbation of a system at equilibrium by a small amplitude sinusoidal excitation signal [47]. The potential of EIS is that the impedance of the system can be scanned over a wide range of AC frequencies [48]. The equivalent circuit model analysis provides an informative perspective of the interpretation of impedance spectrum data and demonstrated as a pivot technique for analysis, characterization of coating, batteries, and fuel cells study [49] [50] [51]. It has also been used extensively as a tool to investigate electrode kinetics, conducting polymers, semiconductors, sensors, animal and plant tissues, and general material [52] [53] [54]. Biosensors are constructed to monitor a biological reaction at the surface of electrodes [55]. A variety of biomolecules have been used as basic detection elements of AC impedimetric biosensors with varying degrees of success. Various studies including enzymes, antibodies, DNA/ RNA, cells, and microorganisms have been immobilized onto the surface of electrodes to develop impedimetric biosensors [56].

2.2 Modeling of nanowell sensor

A nanowell impedance sensor consists of a pair of overlapping electrodes with a thin dielectric layer sandwiched in between. An array of wells embedded into the overlapping area creates a conductive path between the top electrode and the bottom

electrode. Probe antibodies are immobilized inside the wells. The impedance between the two electrodes is monitored in real-time. As proteins bind to the antibodies inside the wells, the impedance between the two electrodes increases. This increase is due to the partial occlusion of ions passing between the electrodes. The quantity of target protein present in the serum in the wells will determine the ultimate drop-in current measured between the electrodes. The equivalent circuit model of a nanowell device is shown in Figure 2-1.

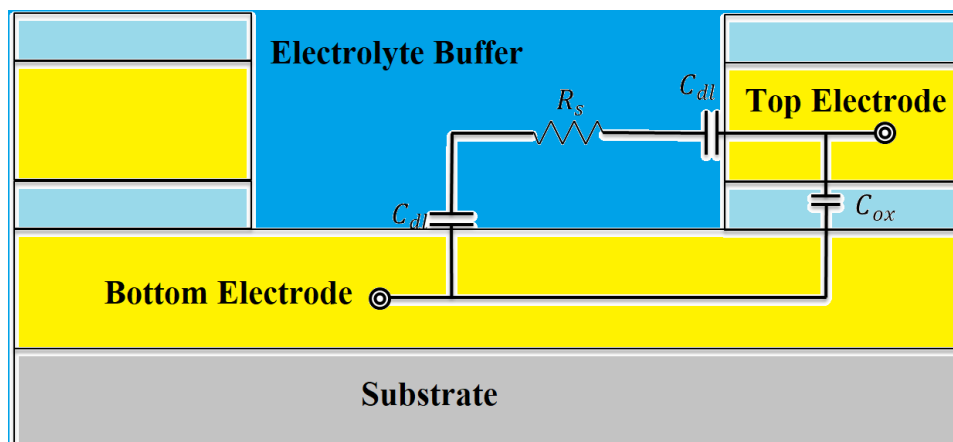


Figure 2-1 Equivalent circuit model of nanowell device

The model consists of the oxide layer capacitance (C_{ox}), which represents the capacitance of the electrical insulation layer between the two electrodes, in parallel with a series structure of two double-layer capacitances (C_{dl}), and the solution resistance (R_s). The oxide layer capacitance and the double-layer capacitances are both constructed of two parallel plates, whose capacitances can be calculated using the following simple formula:

$$C = \frac{\epsilon * A}{d}$$

where ε is the electric constant of the medium, A is the area of overlap of two electrodes, and d is the separation gap between two electrodes.

In the case of the oxide layer capacitance, the area is the overlap area of the sensor, but except for the wells, while d is the thickness of the electrical insulation layer with an electric constant of $\varepsilon_{C_{ox}} = 16.7 \varepsilon_0$, which gives $A_{C_{ox}} = 321.46 \mu\text{m}^2$, $d_{C_{ox}} = 40 \text{ nm}$, and the capacitance of the oxide layer $C_{ox} = 1.188 \times 10^{-12} \text{ F}$. The double-layer capacitances appear at the interface between a conductive electrode and an adjacent liquid electrolyte. At this boundary, two layers of charge with opposing polarity form, one at the surface of the electrode and one in the electrolyte. These two layers, electrons on the electrode, and ions in the electrolyte are typically separated by a single layer of solvent molecules that adhere to the surface of the electrode and act as a dielectric in a conventional capacitor. $A_{C_{dl}}$ is equal to the area of trace A_{trace} , is $63.48 \times 10^{-8} \text{ m}^2$. And the double layer capacitances have 2 components due to the electrolyte, and the oxide layer.

$$C_{dl} = \frac{\varepsilon_{PBS} * A_{trace}}{d_{PBS}} + \frac{\varepsilon_{ox} * A_{trace}}{d_{ox}} = 4.5 \times 10^{-7} \text{ F}$$

where $\varepsilon_{ox} = 16.7 * \varepsilon_0$, $\varepsilon_{PBS} = 80 * \varepsilon_0$, $d_{PBS} = 1 \text{ nm}$ and $d_{ox} = 40 \text{ nm}$.

The resistance of the solution can be calculated by $R_s = \rho \frac{L}{A}$, where ρ is the resistivity of the solution, L is the length of the wire (in this case, the gap between two electrodes), and A is the intersection area of the wire. However, for the nanowell device, the intersection area is not the size of the nanowells because the top electrodes

are patterned with the well structure. The calculation of the effective radius of the wells is necessary. A simulation of the electric potential of the device was run with COMSOL 5.1, and the results are shown below in Figure 2-2.

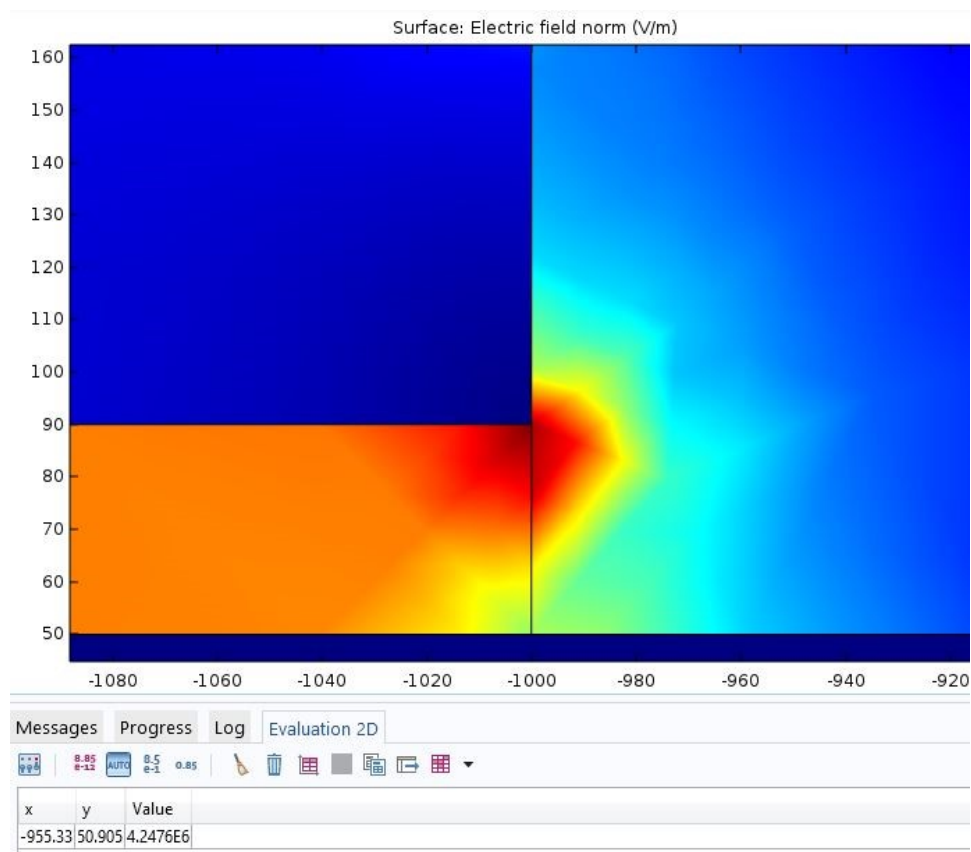


Figure 2-2 COMSOL simulation results of the normalized electrical field of nanowell sensor

The effective radius can be defined as the distance between the sidewall of the well and the point on the sensor surface where the electric potential decreases to $1/e$ of its maximum value. According to the simulation results, the effective radius is 45 nm. Considering an electrical effective well whose area is equal to the ring area of the effective radius, and it results in the electrical effective well size $R' = 296$ nm. Given all the values shown above, the resistance of the solution,

$$R_s = \rho \frac{L}{A'} = \frac{0.625 \cdot 40 \cdot e^{-9}}{25 \cdot \pi \cdot (296e^{-9})^2} = 3.633 \text{ k}\Omega.$$

As shown in Figure 2-1, the impedance of the device can be interpreted in terms of oxide layer capacitance (C_{ox}), double-layer capacitance (C_{dl}), and the solution resistance (R_s). The function of impedance as the varying frequency can be found using the following:

$$T(s) = \frac{-2\omega^2 R_s C_{ox} C_{dl} + \omega^2 R_s C_{dl} (2C_{ox} + C_{dl})}{\omega^4 R_s^2 C_{ox}^2 C_{dl}^2 + \omega^2 (2C_{ox} + C_{dl})^2}$$

$$-j \left(\frac{\omega^3 R_s^2 C_{dl}^2 C_{ox} + 2\omega (2C_{ox} + C_{dl})}{\omega^4 R_s^2 C_{ox}^2 C_{dl}^2 + \omega^2 (2C_{ox} + C_{dl})^2} \right)$$

The frequency spectrum of the system impedance and its real and imaginary components are shown below in Figure 2-3.

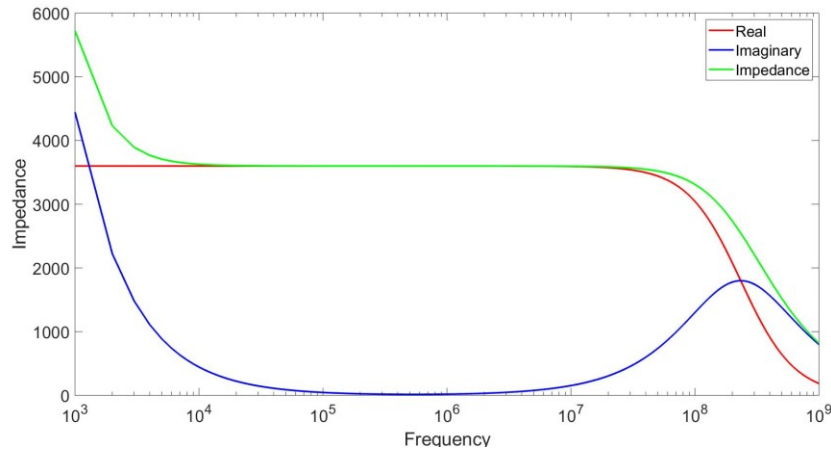


Figure 2-3 Impedance Spectrum information of nanowell model

At $f = 2\pi\omega = 1$ MHz, the real component of the impedance is about 3.6 k Ω , while the imaginary component is 30 Ω , less than 1% of the real component, which shows the system impedance is real component dominant.

As proteins bind to the antibodies inside the wells, the impedance between the two electrodes increases. To be specific, the resistance of the solution R_s would change to $R_s + R_p$, where R_p represents the resistance of binding protein.

Then, the calculation of the resistance of binding protein is the pivot question in the modeling. An analysis with a combination of the assumption of considering the protein size as a sphere and Maxwell's approximation of expression for the effective resistivity has been done to calculate the exact R_p value. The direct calculation or simulation of the impedance of a single protein molecule is quite profound and complicated. We propose an assumption to simplify the question that considering the single protein molecule as a solid sphere whose volume is equal to the equivalent volume of the protein molecule. To be specific, the dimensions of human Interleukin 6 protein are approximately 8.3 nm * 6.1 nm * 5.5 nm, which results in the diameter d_p of the equivalent volume sphere being 8.1 nm. An expression for the effective resistivity ρ_{eff} of a dilute suspension of insulating spheres in a solution of spheres in suspension is introduced in Maxwell's approximation resistivity ρ . Put in terms of the volume fraction f of the spheres in suspension, Maxwell's approximation is $\rho_{eff} = \rho (1 + \frac{3f}{2} + \dots)$. If we consider a 5*5 array of nanowells of diameter D and length d_{gap} filled with a fluid of resistivity ρ , then the resistance approaches

$$R = \frac{\rho * d_{gap}}{25 * \pi * \left(\frac{D}{2}\right)^2} = \frac{4 * \rho * d_{gap}}{25 * \pi * D^2}$$

The resistivity of the medium will change to $\rho_{eff} = \rho \left(1 + \frac{3f}{2} + \dots\right)$ due to the newly introduced particles, where the volume fraction is

$$f = \frac{\frac{4}{3}\pi\left(\frac{d_p}{2}\right)^3}{\pi\left(\frac{D}{2}\right)^2 d_{gap}} = \frac{2d_p^3}{3D^2 d_{gap}}$$

Then, changing the expression of volume fraction into effective resistivity equation, we have,

$$\begin{aligned} R_{new} &= \frac{\rho_{eff} * d_{gap}}{N * \pi * \left(\frac{D}{2}\right)^2} = \frac{4 * d_{gap}}{N * \pi * D^2} * \rho * \left(1 + \frac{3}{2} * \frac{2d_p^3}{3D^2 d_{gap}} + \dots\right) \\ &\approx \frac{4\rho d_{gap}}{N\pi D^2} + \frac{4\rho d_p^3}{N\pi D^4} = R + R_p \end{aligned}$$

Thus, the impedance change of a single protein molecule

$$R_p = \frac{4\rho d_p^3}{N\pi D^4}$$

where d_p is the diameter of an equivalent volume sphere equal to 8.1 nm, N is the number of nanowells (25 in this case), and D is the electrical effective well diameter (592 nm). The impedance change of a single protein molecule based on the sphere model and Maxwell's approximation is 0.1377 Ω .

Then, the quantification of the binding protein amount is also needed. Introducing Damkohler Number here,

$$Da = \frac{k_{on}b_mL}{D\tilde{F}}$$

where b_m is the surface concentration of receptors on the sensor; k_{on} is the binding constant that represents the rate of target protein binding to the receptors on the surface with the units of number/ M·s; L is the sensor length, and D is the diffusion rate of protein with the unit of m² /s. \tilde{F} is the dimensionless collection function, $\tilde{F} = \frac{J_D}{Dc_oW_s}$, which describes the total collection rate against the total diffusion rate. In that function, J_D is the total collection rate in the unit of number/M.

As mentioned previously, the impedance of the device will change due to the binding of the target protein, and it is clear that the impedance response is in proportion to the amount of binding protein. A calculation of the amount of binding protein has been done based on the absorption kinetics. Assume the surface absorption follows the first-order Langmuir kinetics, which makes the following assumptions: 1. the protein molecules are considered as hard spheres and the binding sites are flat and uniform; 2. the molecules are effectively well diluted and uniformly distributed to assume that the variations of the concentration do not affect the properties of the fluid, and 3. the process continues until the surface reaches its dimension limit or saturation. The surface concentration $b(t)$ of receptors that are bound by target molecules obeys

$$\frac{\partial b}{\partial t} = k_{on}c_s(b_m - b) - k_{off}b$$

where b_m is the surface concentration of receptors on the sensor, k_{on} and k_{off} are the binding constant that represents the rate of target protein binding to the receptors on the surface and the rate bound protein strips off from the receptors on the surface with the units of $1/M \cdot s$ and $1/s$, respectively. Binding depends on the concentration of unbound sites ($b_m - b$) and on target protein concentration c_s at the sensor surface, whereas target molecules de-bind in proportion to the bound concentration. For the reaction limits type sensor $c_s \approx c_0$, the bulk concentration of target protein and surface concentration of receptors can be solved from the previous equation, as following,

$$\frac{b(t)}{b_m} = \frac{c_0/K_D}{1 + c_0/K_D} (1 - e^{-(k_{on}c_0 + k_{off})t})$$

where the equilibrium dissociation constant $K_D = k_{on}/k_{off}$ appears as a natural concentration scale. The fraction of bound receptors in equilibrium b_{eq} is given by

$$\frac{b_{eq}}{b_m} = \frac{c_0/K_D}{1 + c_0/K_D} \equiv \frac{\tilde{c}}{1 + \tilde{c}}$$

where $\tilde{c} = c_0/K_D$ is the concentration, non-dimensionalized by the natural concentration scale K_D . The density of active binding sites b_m depends strongly on the immobilization procedure, and extensive effort has been directed toward optimizing binding efficiency. The typical active binding sites' density ranges from $10^9 - 10^{12} / cm^2$. Given a range of active binding sites' density, the fraction of

bound receptors in equilibrium b_{eq} is a function of bulk concentration, as Figure 2-4 shows.

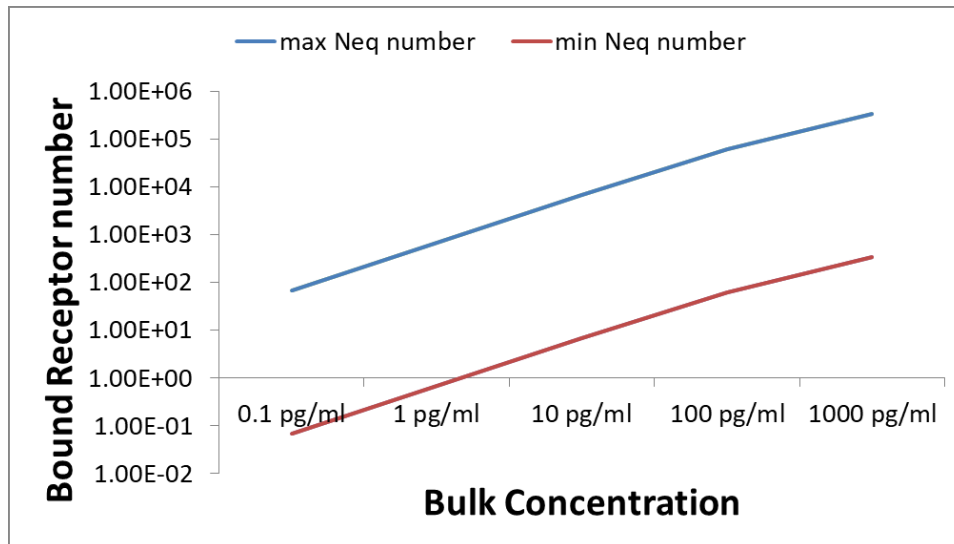


Figure 2-4 Binding site number on sensor surface at different bulk concentration

2.3 Results of modeling of nanowell sensor

The total bound receptors number at equilibrium is,

$$N_{eq} = b_{eq} * b_m * A$$

and the total impedance change is,

$$\Delta R_{total} = N_{eq} * R_p$$

Therefore, the total resistance change can be described as a function of the fraction of bound receptors in equilibrium b_{eq} , which is determined by the bulk concentration, as Figure 2-5 shows.

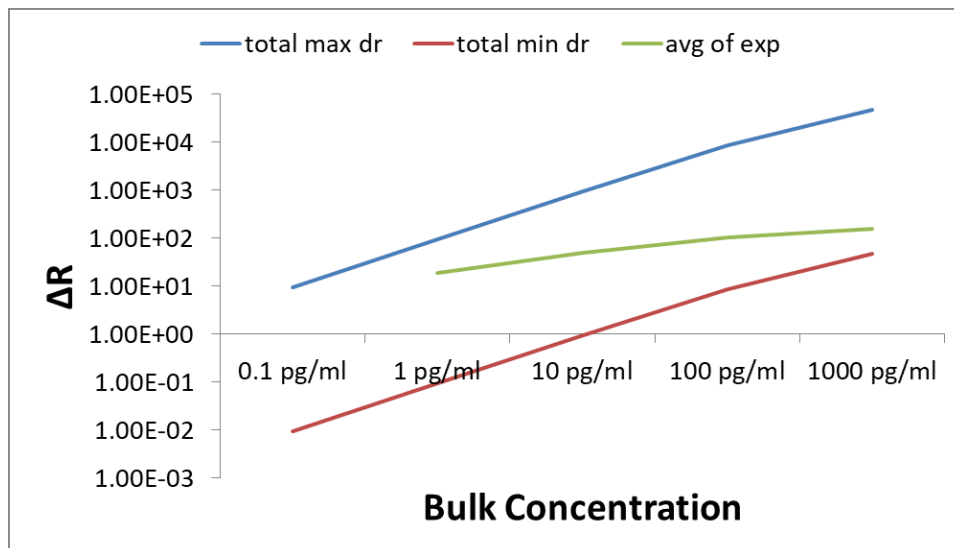


Figure 2-5 Resistance change of nanowell sensor at different bulk concentration of IL6

Figure 2-6 shows the model results for tumor necrosis factor- α (TNF- α).

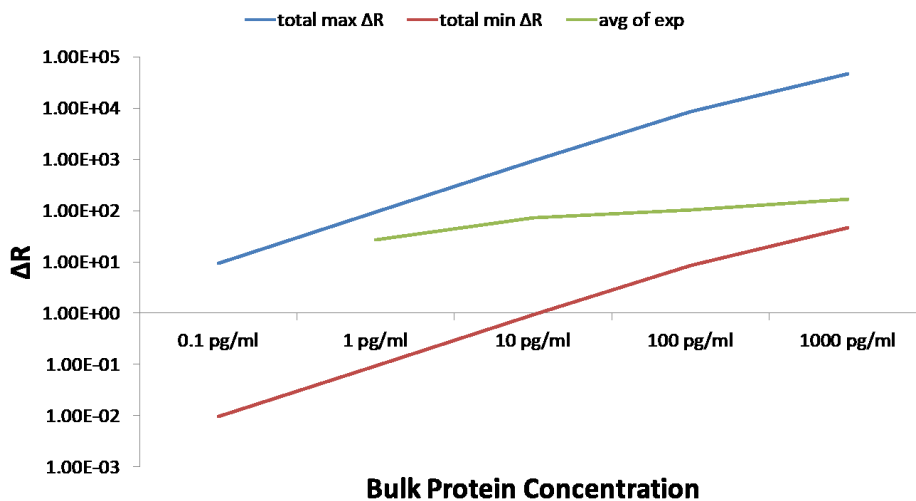


Figure 2-6 Resistance change of nanowell sensor at different bulk concentration of TNF- α

We also studied the quantitative relationship between total impedance change and nanowell diameter. The effective binding area increases with the increment in the nanowell radius. However, the number of wells in the nanowell array decreases in

terms of unit area, which is the dominant factor that results in the total resistance change, which is larger with the smaller nanowell radius, as Figure 2-7 shows.

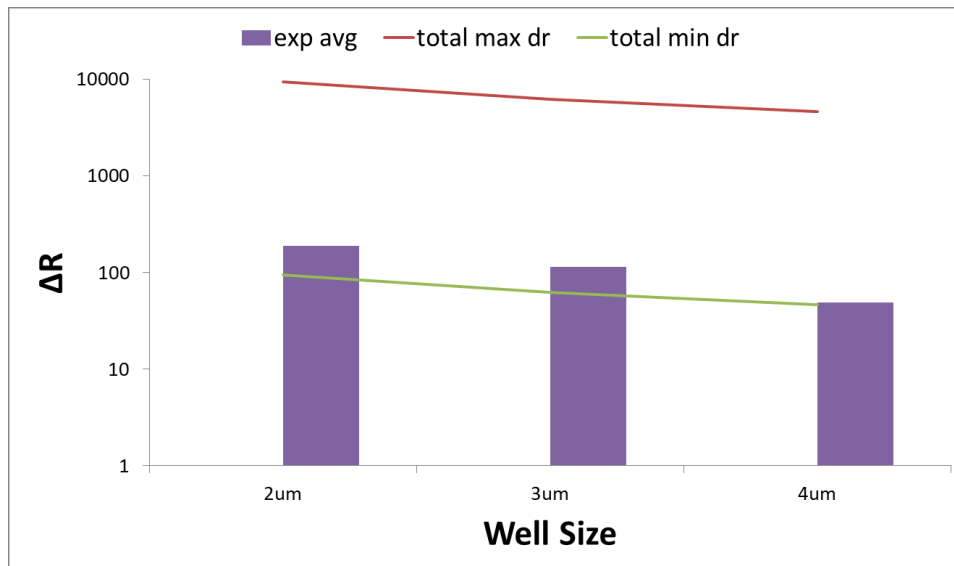


Figure 2-7 Resistance change of nanowell sensor at the different well size

According to the theory, total impedance change is equal to the impedance change due to single protein binding times the binding amount,

$$\Delta R_{total} = N_{eq} * R_p$$

and

$$N_{eq} = b_{eq} * A \text{ and } R_p = \frac{4\rho d_p^3}{N\pi D^4}$$

Given certain concentrations of the target protein, the b_{eq} is a constant. The decrement of the well diameter would affect the effective sensor area A and electrical effective well diameter D .

Defining the well diameter is d with the unit of nm, and then electrical effective well diameter follows,

$$\pi * d^2 - \pi * (d - 45)^2 = \pi * D^2$$

$$D^2 = 90 * d - 45 * 45.$$

We can also see that if d is less than 22.5, D^2 is a negative value, which makes no sense. In a situation where d is less than 22.5, the whole well area is all effective, so the electrical effective well diameter D is the diameter of the well d .

$$D^2 = 90 * d - 45 * 45, \text{ when } d > 22.5$$

$$D = d, \text{ when } d < 22.5$$

The total effective sensor area $A = \pi * D^2 * N$, where N is the number of wells, equals $(10 * 10^3 * d)^2$.

Therefore,

$$\Delta R_{total} = N_{eq} * R_p = b_{eq} * A * \frac{4\rho d_p^3}{N\pi D^4} = b_{eq} * \frac{4\rho d_p^3}{D^2} = \frac{K}{D^2}$$

$$= \frac{K}{90 * d - 45 * 45}, \text{ when } d > 22.5$$

$$\Delta R_{total} = \frac{K}{d^2}, \text{ when } d < 22.5.$$

Therefore, with the decrement of well diameter, the sensitivity of the sensor increases and maximizes out when the well diameter reaches the effective width (~ 22.5 nm).

Beyond this turning point, the sensor would lose sensitivity, as the decrement of well diameter is decreasing the effective area.

Chapter 3: Label-free Assay for Quantitatively Assessment of Cytokine levels

Label-free electronic affinity-based immunosensing is an attractive candidate as a platform technology for analyzing biomarkers due to the ease of miniaturization and the minimal use of reagents. Electronic-based sensing approaches, however, have lagged behind their optical counterparts in terms of detection limit, selectivity, and reliability. In addition, the matrix- dependent nature of electronic sensing modalities analyzes biomarkers in high salt concentration samples such as serum difficult due to charge screening. We present a novel sensing platform, the nanowell sensor, which works by functionalizing nanoscale volume wells with antibodies and monitoring the impedance change inside the wells due to the binding of the target protein. This detection modality is advantageous to many label-free electronic sensors in that signal power scales with increases in salt concentration, thus improving the sensitivity of the platform. We demonstrate real-time label-free quantification of cytokines within 10 minutes at femtoMolar concentrations and a dynamic range of three orders of magnitude in serum samples. We describe the design, fabrication, and characterization of the nanowell sensor in serum samples using inflammatory protein biomarkers.

3.1 Introduction

Affinity based biosensors detect proteins and nucleic acids through the immobilization of probe molecules on a transducer substrate to attain specificity in

the detection of the target macromolecule of interest. In the context of protein detection, protein array technologies provide a valuable platform for functional proteomic analysis [57]. A protein microarray provides a multi-functional platform enabling comprehensive and high throughput studies, which can be widely used in biomarker validation studies [58], a study of protein-protein interactions [59], protein-DNA interactions [60], and detection of various antigens and antibodies [61]. Among affinity-based biosensing technologies, there are two major detection strategies, label-based and label-free. Both approaches have their merits and disadvantages. Label-based technologies typically achieve lower detection limits and higher selectivity, yet require multiple steps. Label-free techniques tend to lag behind their labeled counterparts in terms of detection limit and specificity, yet often can be performed in a single step, while also enabling real-time monitoring and determination of the binding kinetics involved in the interaction [62][63].

Label-free biosensing technologies, both optical and electrical, have shown significant promise in the research setting and the literature [64][65], however, have had difficulty moving beyond the lab and progressing to commercialization, or more importantly clinical translation [66][67]. In the context of protein biomarker detection, exceptions include plasmonic-based technologies like BIAcore [68] and photonic technologies such as BioLayer interferometry [69]. IonTorrent, a commercially available label-free electronic CMOS based technology for DNA sequencing, has shown promise for relatively low-cost genome sequencing [70]. The ability to accurately assay biological samples to the extent where it can be used for reliably attaining measurements in animal or human studies requires minimizing

measurement inconsistency, device variability, and also must be capable of accurate detection of biomarkers in biological matrices like blood, which is highly complex and has high salt concentration. Electronic detection technologies, such as charge based sensing using nanowire FETs and impedance sensing based on Debye layer modulation, often operate effectively in low salt environments [71].

High salt concentration results in charge screening and minimizing the Debye layer thickness to approximately 1 nm, thus making E-fields unable to penetrate beyond the length of the capture antibody (10-20 nm). A novel approach based on incorporating a porous biomolecule permeable layer on the sensor which increases the effective screening length in the region immediately adjacent to the device has also been presented [72]. Using this approach, they detected PSA in 100 mM Phosphate Buffer at a detection limit of 10 nM. The primary challenge faced by label-free technologies stems from measurement variability and inconsistency, thus not being suitable for reliable quantification of molecular levels. The first and foremost reason is that stochastic variation in levels of binding greatly increases as biosensors excessively miniaturize down to the nano regime [73]. The probability of diffusion of the analyte and its subsequent binding to the sensor surface decreases significantly when the sensor active area dimensions are in the nano- regime. Hassibi et al. developed a comprehensive noise model examining the effects of scaling on the solution to the Fokker-Planck equation and analyte binding fluctuation and demonstrated that scaling down significantly reduces the achievable repeatability and dynamic range of biosensors. This can potentially explain one of the reasons why technologies such as BIAcore, BioLayer Interferometry, and IonTorrent, which are all micro-scale

detection technologies, have been successfully commercialized while nanoscale label-free technologies, such as nanowires [64] and Surface-Enhanced Raman Scattering [74], have had difficulty making it out of the lab, despite the promise they have shown in the literature. The problem of inconsistency is even more pronounced in nano-sensors that have been fabricated using bottom-up synthesis approaches, that show great sensitivity, yet repeatability is a major problem resulting from batch to batch fabrication variations. Thus, top-down fabrication approaches have shown promise to work with higher precision. Probe-free detection modalities, such as Surface-Enhanced Raman Scattering (SERS), are highly dependent not only on the binding rate of molecules with the sensor surface but also on the orientation of the binding analyte [75], thus inconsistency is an issue even for precisely patterned sensors using top-down fabrication approaches. Label-free sensing approaches have also lagged behind their fluorescence-label based counterparts due to lack of long-term reliability resulting from electrode corrosion and fouling. Additionally, nanopore-based sensing is an established method for achieving extremely high sensitivity, even at physiological salt concentrations. Functionalized nanopores have been shown to achieve selectivity in protein detection [76]. Label-free protein sensing with low detection limits has been demonstrated using nano-textured materials. Detection of proteins in blood or serum using label-free impedance-based techniques is difficult due to the high salt concentration of the matrix, which results in the screening of the charge of the target proteins. In this work, we describe a novel sensing configuration where sensitivity is enhanced as the salt concentration of the

matrix increases. We demonstrate robust performance through repeated testing in rat serum.

3.2 Nanowell Array Impedance Sensor

The nanowell impedance sensor consists of a pair of overlapping electrodes with a thin dielectric layer sandwiched in between. An array of wells embedded into the overlapping area creates a conductive path between the top electrode and the bottom electrode. Probe antibodies are immobilized inside the wells. The impedance between the two electrodes is monitored in real-time. As proteins bind to the antibodies inside the wells, the impedance between the two electrodes increases. This increase is due to the partial occlusion of ions passing between the electrodes. The quantity of target protein present in the serum will determine the ultimate drop-in current measured between the electrodes. A higher salt concentration results in a larger current and thus higher signal power corresponding to larger changes in the current due to protein binding, making the sensor ideal for the quantification of proteins in high salt content matrices such as serum. Figure 3-1 shows the nanowell array label-free impedance sensor schematic.

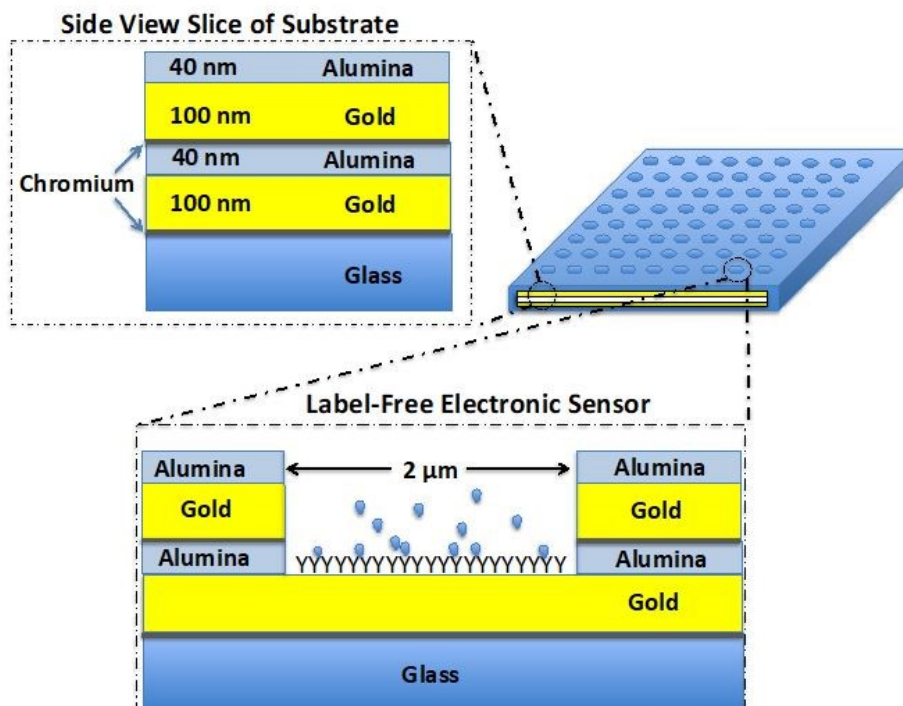


Figure 3-1 Nanowell Array Label-free Impedance sensor schematic

The sensor consists of a stack of two gold electrodes in which the bonding pads accessing each are located on opposite sides of the chip. The two electrodes extend from the bonding pads to the center of the chip such that they overlap each other with an area of $20\ \mu\text{m} \times 20\ \mu\text{m}$. Lock-in-amplification is used to measure the AC current passing through the electrode inside the wells. Figure 3-2 shows the measurement setup using a lock-in amplifier.

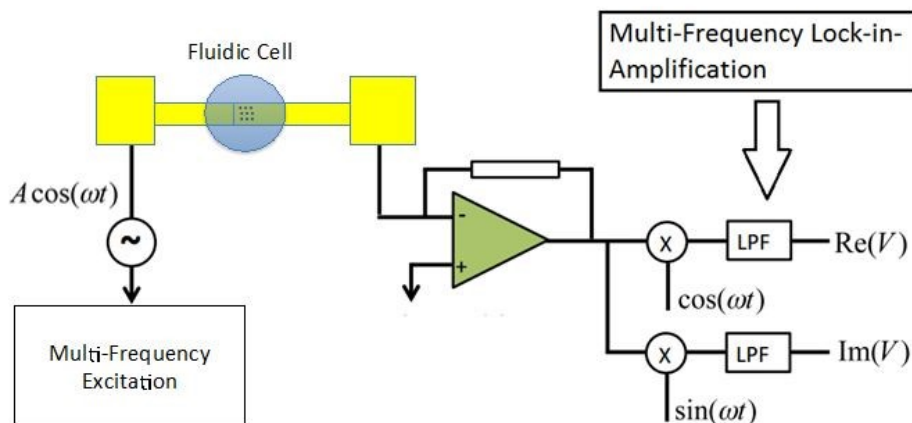


Figure 3-2 Measurement setup using lock-in-amplifier

3.3 Materials and Methods

Sensor fabrication

The following fabrication procedure was used to form the sensors on a glass substrate. The first electrode was fabricated using standard photolithography, electron beam evaporation of gold, and lift-off processing. The metal layer consisted of a 5 nm layer of chromium to enhance the adhesion of the gold film to the substrate and a 100 nm gold layer on top. A 40 nm layer of aluminum oxide was deposited onto the first electrode using atomic layer deposition. The second electrode layer (again consisting of 5 nm chromium and 100 nm gold) was patterned using the same procedure as for the first layer. Another 40 nm layer of aluminum oxide was deposited on top of the second electrode using atomic layer deposition to serve as a protection against

fouling. A layer of photoresist was spin-coated onto the wafer. An array of micron-sized holes was photo-patterned onto the overlapping area of the two electrodes. Multiple wet etch steps were performed to remove the top aluminum oxide layer (buffered oxide etchant), the gold and chromium layer (gold and chromium etchant), and the bottom aluminum oxide layer (buffered oxide etchant) inside the wells. The photoresist was then stripped off. A second photomask was used to pattern photoresist to protect the sensors to be able to etch off various parts of the alumina outside of the sensing region to expose the glass surface. Devices with $20\ \mu\text{m} \times 20\ \mu\text{m}$ and $100\ \mu\text{m} \times 100\ \mu\text{m}$ overlapping areas are shown in Figure 3-3A and Figure 3-3B.

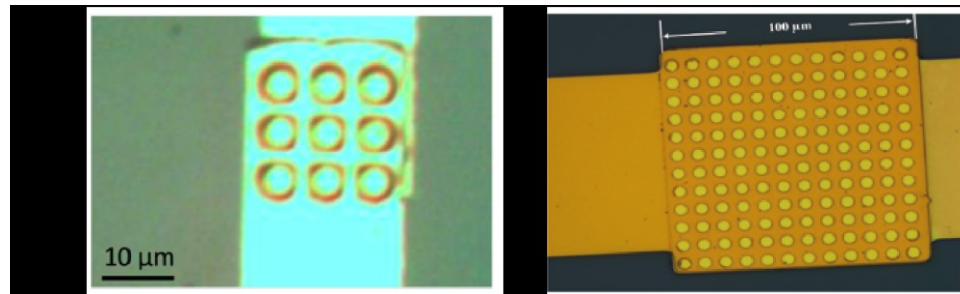


Figure 3-3 Microscopic images of micro-fabricated sensors of differing sizes and array size and density. A) 9 well and B) 144 well array device

A fluidic cell, for confining the liquid, made of PDMS was then bonded on top of the sensor substrate using oxygen plasma treatment. The fluidic cell consists of a millimeter diameter well that allows for fluid to be directly incubated onto the substrate.

Electrical Impedance Spectroscopy Sensor Characterization

It is critical to understand the impedance behavior of the system to determine the optimum frequency region for performing real-time measurements. We used a potentiostat (Gamry Instruments, Warminster, PA, USA) to characterize the impedance spectrum of the biosensor devices, as shown in Figure 3-4. Real and imaginary components of the device's impedance measured at different frequencies are shown in Figure 3.5.

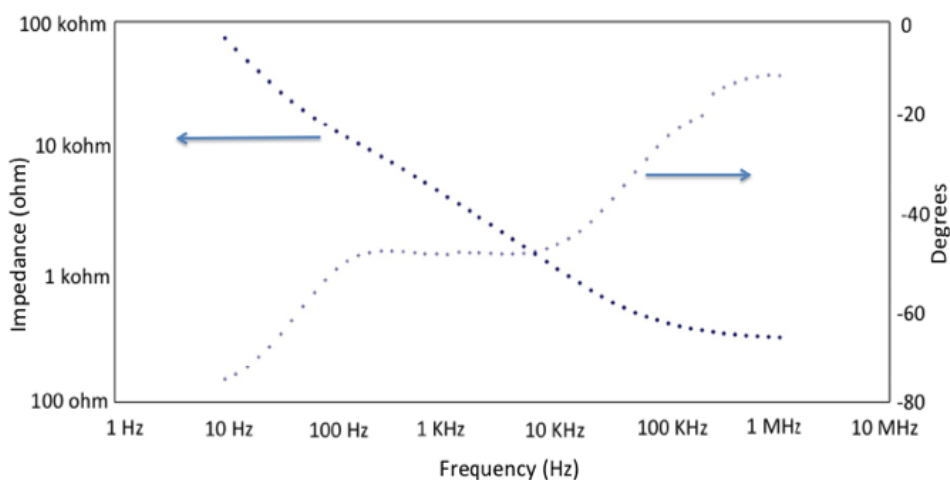


Figure 3-4 Magnitude and Phase of Impedance spectrum of device. Device starts out capacitive at low frequencies and response becomes dominated by solution resistance as frequency is increased beyond 100 KHz

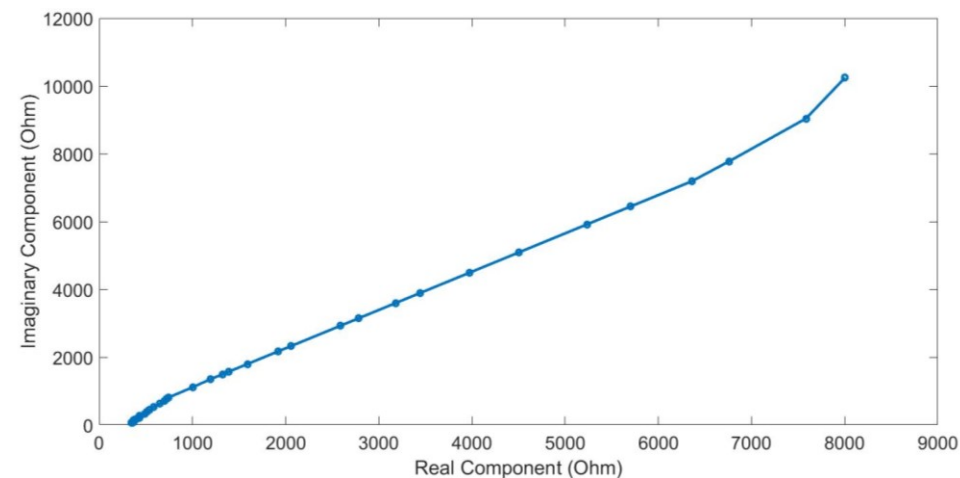


Figure 3-5 Real component and imaginary component of device impedance

We performed impedance measurements on a multitude of fabricated sensors ranging from 10 Hz to 3 MHz. The impedance was dominated by the double-layer capacitance until 100 KHz. Beyond 100 KHz, the impedance flattened out and became dominated by resistance. Therefore, we chose to operate at a frequency of 1 MHz to monitor changes in ionic resistance as a result of antigen-binding.

Reagent Preparation and Antibody Immobilization

Antibodies and target proteins were suspended in phosphate-buffered saline (PBS). Monoclonal anti-human leptin IgG antibodies (MAB510, R & D Systems, Minneapolis, MN, USA) were suspended in PBS at a concentration of 0.2 mg/ml. The target cytokine used in this study, human leptin (510RT, R & D Systems), was suspended in concentrations ranging from 6 nM to 6 fM. During the experiments, the target cytokine buffer was mixed with pure rat serum at a 1:1 ratio. We spiked the target human cytokine in rat serum to test the effects of the background matrix on the sensor while ensuring that the endogenous levels of the rat leptin cytokine that may or

may not be present in the rat serum would not interfere with the sensor during control experiments. The antibodies were physically adsorbed onto the sensor surface by injecting 5 μ l of anti-leptin solution into the sensor well and incubating for 10 minutes.

Real-Time Impedance measurements

Figure 3-2 above shows a schematic of our test setup. We formed a 1 mm sized well on top of the sensor to confine the fluid. Reagents were sequentially added manually to the well, and the complex impedance was monitored in real-time. The impedance inside the nanowells was measured using a multi-frequency lock-in amplifier (Zurich Instruments HF2IS, Zurich, Switzerland). The AC excitation source, providing 0.4 V at a frequency of 1 MHz, was connected to one of the electrodes, and the second electrode was connected to the input of the lock-in amplifier, where the real and imaginary components of the impedance were both acquired.

3.4 Results and Discussion

To perform measurements with maximum sensitivity, it is extremely critical to capture impedance changes occurring in the sensors as biological binding events occur in real-time. Tests were initially performed in purified samples. In Figure 3-6, the output of the lock-in amplifier is shown as an empty well and is filled with PBS.

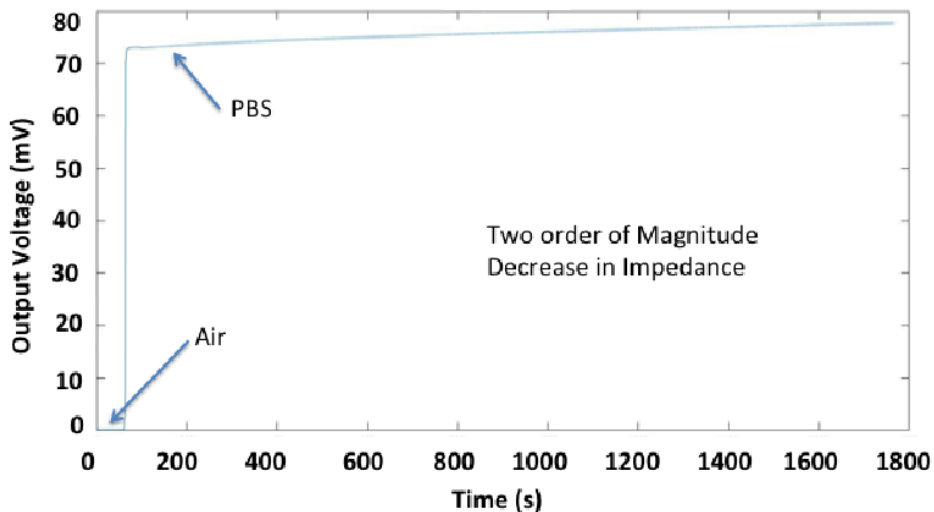


Figure 3-6 Output voltage of lock-in amplifier as PBS is added to an empty channel

The output voltage, or the current across the electrodes, increased by two orders of magnitude. This means the impedance across the electrodes decreased by two orders of magnitude, which is expected because of the high conductivity of the buffer. As a negative control, a blank PBS sample was added to the well, resulting in a minimal shift in baseline in the positive direction, as Figure 3-7 shows.

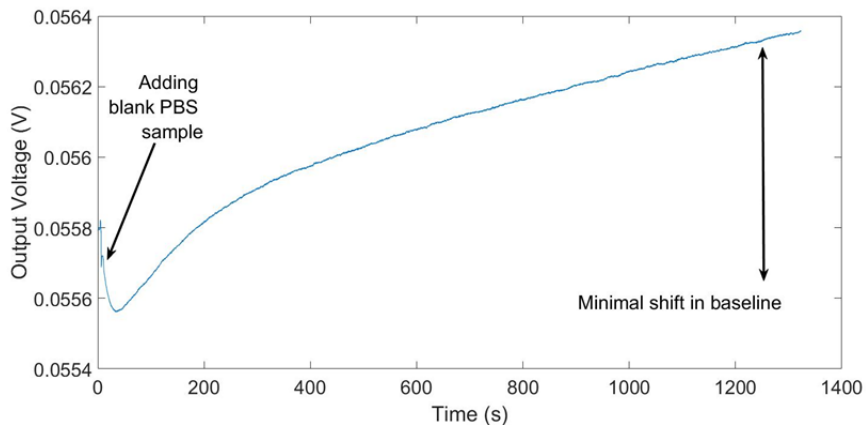


Figure 3-7 Output voltage of lock-in amplifier as blank PBS is added (negative control)

In the next step, anti-leptin antibodies were added to the wells, and the antibodies were physically adsorbed to the gold surface, as Figure 3-8 shows.

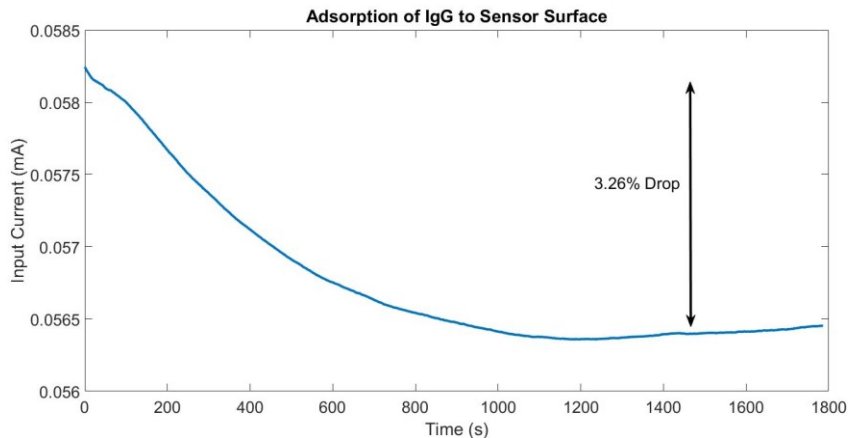


Figure 3-8 Output current of lock-in amplifier as adsorption of IgG to the sensor surface

When the channel becomes filled with PBS and antibodies are added to the mix and adsorb inside the well, a decrease in output voltage or an increase in impedance is observed. This is consistent with our model, where the presence of protein resulted in the occlusion of an ionic current passing between the electrodes, thus increasing resistance, as Figure 3-9 shows.

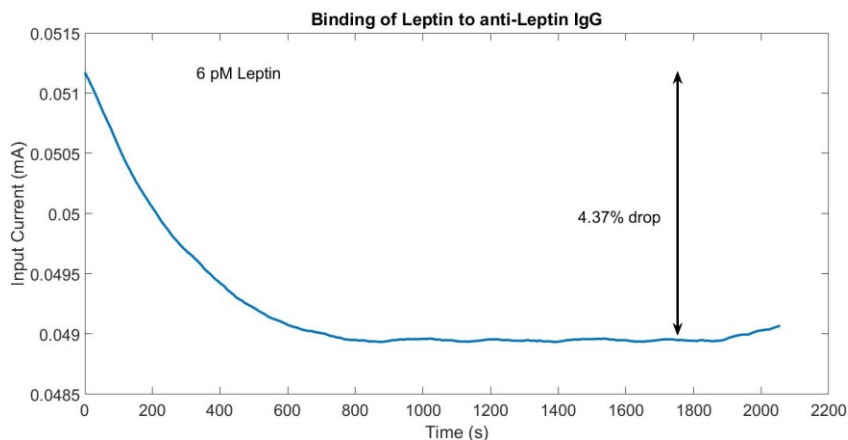


Figure 3-9 Input current of lock-in amplifier as binding of leptin to anti-leptin IgG

A unique exponential pattern to these drops in voltage (or rise in impedance) is observed, which is consistent with time-dependent behavior of antigen-antibody binding. This is similar to the response observed with SPR-based biosensors. The time scale to reach saturation is approximately 10–15 minutes. Figure 3-8 shows representative data of the sensor response with respect to time as the monoclonal antibody (anti-Leptin IgG) physically adsorbed in the channel, resulting in an exponential drop in the baseline. Figure 3-9 shows the sensor response with respect to time as the leptin in the solution bound to the electrode surface-functionalized with anti-leptin IgG, resulting in a 4.37% drop in the current across the electrodes. The fluid in the well was then aspirated, as Figure 3-10 shows, to remove extra antibodies in the solution. PBS was then re-injected, as Figure 3-11 shows.

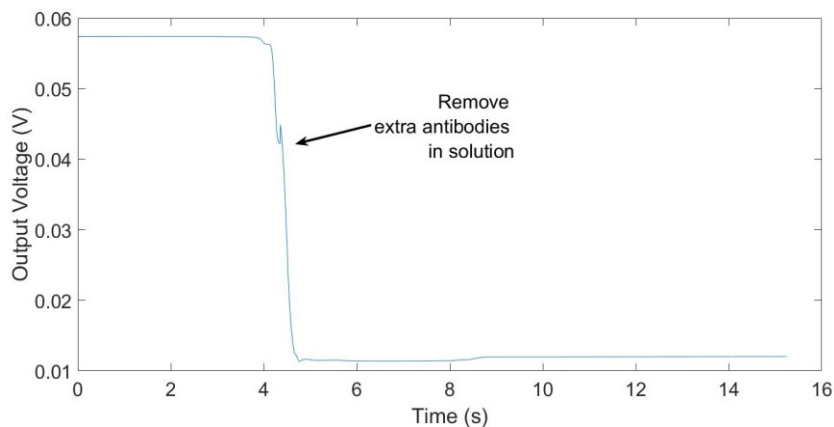


Figure 3-10 Output voltage of lock-in amplifier as extra antibodies removed from well

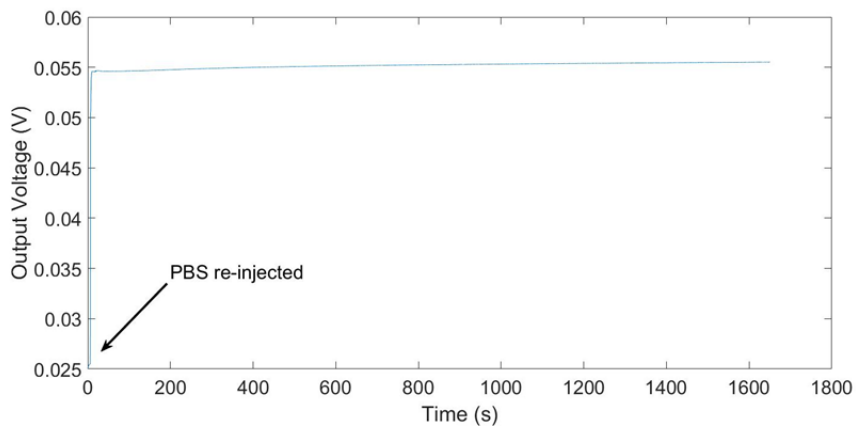


Figure 3-11 Output voltage of lock-in amplifier as PBS re-injected

Again, as a negative control, PBS was added on top of the existing solution. As a negative control, a blank solution of PBS was injected, resulting in a rise in the current (a drop in impedance was observed, likely due to desorption of antibodies), as Figure 3-12 shows.

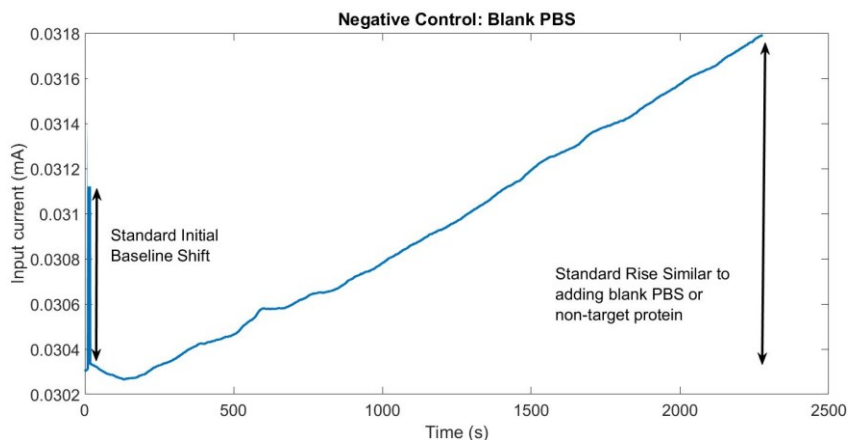


Figure 3-12 Input current of lock-in amplifier as blank PBS injected as the negative control

For negative control experiments, the current across electrodes generally rises by 1%. This was seen with all negative control experiments and is likely due to antibody desorption. The addition of the target antigen (leptin) resulted in an exponential drop in current with a signature similar to that observed during antibody immobilization (Figure 3-9). Accumulation of protein due to non-specific binding increased the ionic resistivity inside the well. A non-target cytokine was injected into the well as a negative control. The current response was similar to that of the addition of a blank PBS sample, as Figure 3-13 shows.

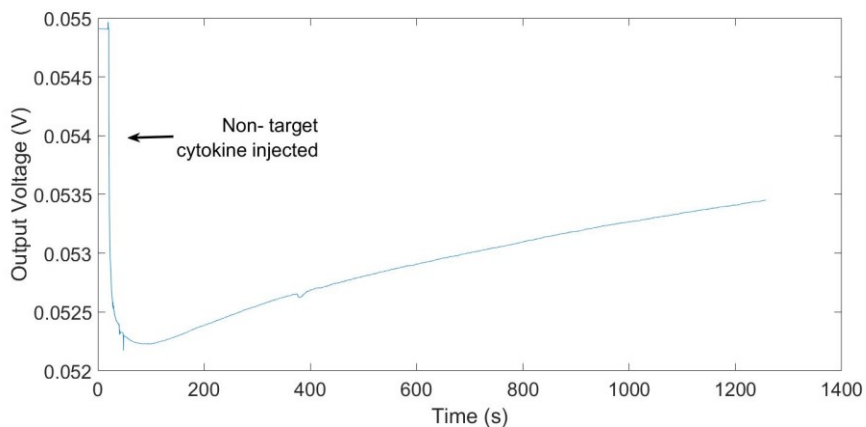


Figure 3-13 Output voltage of the lock-in amplifier as non-target cytokine injected (negative control)

The relative change in impedance observed for each step is illustrated in Figure 3-14.

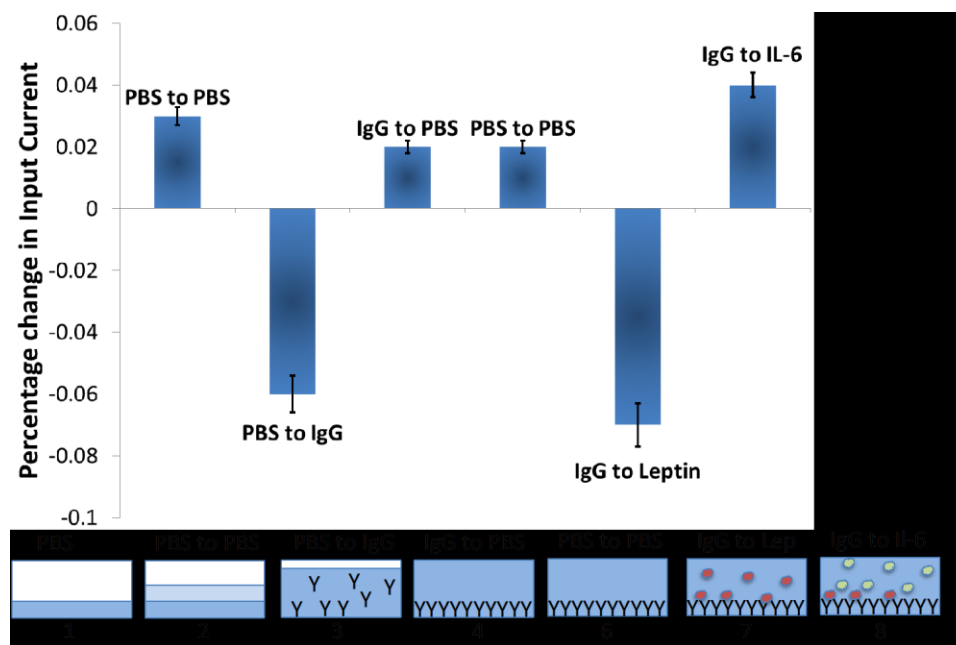


Figure 3-14 Illustration of experimental protocol for device validation and resulting percentage changes in impedance. Antibody adsorption and protein binding inside well

results in decrease in impedance. Negative control steps (adding blank samples or non-targeted protein) results in positive change in current.

After determining the optimum operating frequency and establishing functionality of the device, we set out to determine the optimum device geometry to detect the protein binding in the well. We fabricated devices with nanowells of different diameters. Figure 3-15 shows the results of repeated tests (in triplicate for each diameter) of varying well diameters. We observe that a smaller diameter allows for a larger normalized change in baseline impedance resulting from antibody adsorption inside the well compared to larger diameter wells.

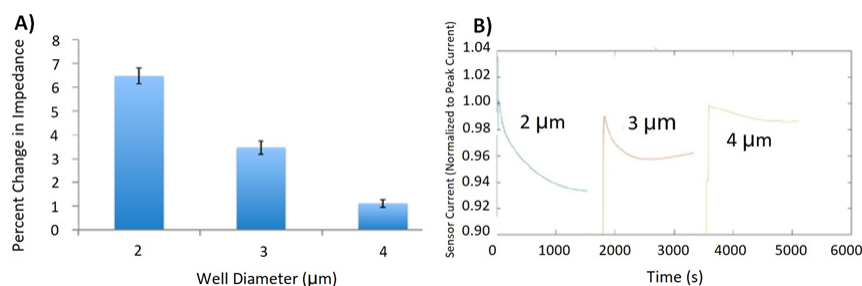


Figure 3-15 Relationship between sensor response to protein binding and well diameter (Left) measured in triplicate over 3 different well sizes and (Right) the current across the electrodes versus time for 2 μm, 3 μm, and 4 μm diameter wells

We also tested devices with oxide thicknesses of 30 nm and 40 nm to determine which provides better sensitivity. The devices with 40 nm thickness showed a larger change in normalized impedance when the antibody physically adsorbed inside the well compared to those with 30 nm thickness. As 40 nm thicknesses already provided

a strong response, further testing was performed using 40 nm thick oxide devices with 2 μm diameter wells.

Upon the successful demonstration of sensor operation in purified samples and the optimization of geometry, we quickly moved on to characterizing sensor performance in spiked serum samples. The procedure to prepare and prime the sensors for the positive and negative control experiments is similar to that illustrated in Figures 3-8, 3-9, and 3-12. In all experiments, a negative control sample of serum from a healthy rat mixed with PBS (1:1 ratio) was used as a negative control, showing a response similar to that of blank samples. Rat serum (Sigma Aldrich, St. Louis, MO, USA) samples spiked with human leptin at a 1:1 ratio with PBS showed a response similar to that of leptin in the purified buffer.

To showcase the agnostic nature of the platform technology, its utility to other target proteins, and its resilience to non-target proteins of higher abundance, we immobilized the sensor with alternate antibodies, including anti-TNF- α IgG (R & D Systems). Figure 3-16 shows the response when testing rat serum spiked with 1 nM of two non-target cytokines, interleukin 6 (IL-6) (R & D Systems) and IL-4 (R & D Systems), both with and without 1 pM of the target protein TNF- α (R & D Systems).

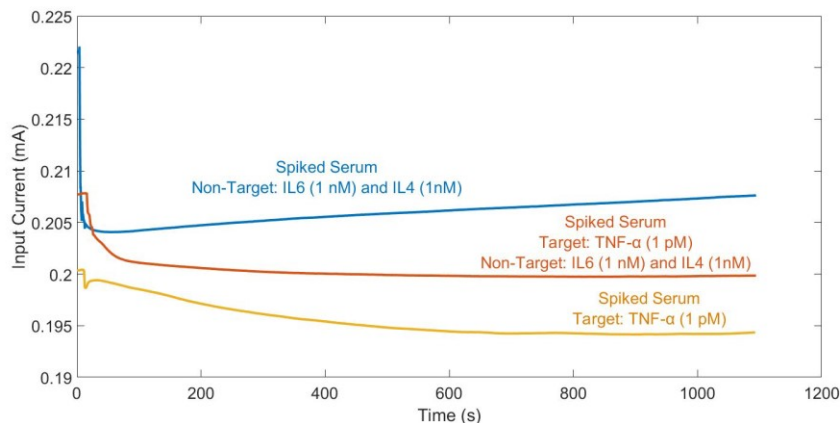


Figure 3-16 Sensor response to the sample spiked with i) target protein (TNF α) at 1 pM and non-target proteins (IL6 and IL4) at 1 nM and ii) Negative control (serum spiked with non-target protein 1nM of IL6 and TNF α)

As seen, when the target protein (TNF- α) is present in the serum, the characteristic exponential decay over a period of minutes until reaching saturation is observed, whereas in the case of the negative control the sensor reaches its minimum value within seconds and then begins rising.

A titration experiment was performed to determine sensor response as a function of analyte concentration. The concentration range tested included human leptin spiked into rat serum 60 pM all the way down to 6 fM. The titration curve for testing 2-micron diameter nanowell sensors is shown below in Figure 3-17.

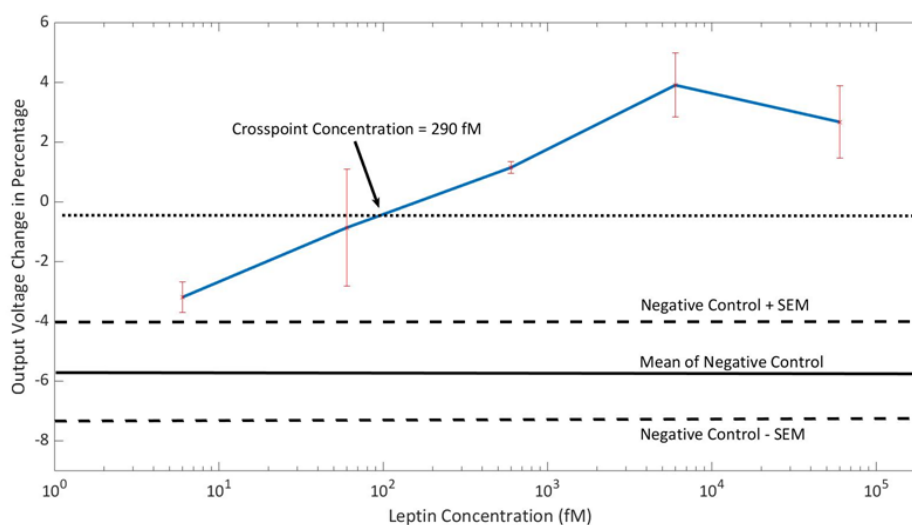


Figure 3-17 Titration curve for concentrations ranging from 60 pM down to 6 fM. Error bars are standard deviation over 3 points. Negative control (NC) is also included. Background level is defined where change in impedance across electrodes is no longer positive. 600 fM is clearly above background. Detection limit is 300 fM.

Reliable detection of leptin is shown 300 fM and higher. All negative control measurements were performed using non-spiked rat serum to ensure that sensor fouling did not result in false-positive signals. As seen in Figure 3-17, the sensor has a dynamic range spanning three orders of magnitude (100 fM to 10 pM). All experiments were performed by spiking leptin into rat serum and were performed in triplicate. All negative control measurements were performed using non-spiked rat serum to ensure that sensor fouling did not result in false-positive signals.

3.5 Conclusion

We present a novel label-free biomolecular sensing modality that consists of an array of antibody functionalized nanoscale wells embedded with electrodes to monitor

changes in ionic resistance as a target protein binds inside the wells. The key novelty and advantage of this sensor geometry are that the high salt concentration of serum serves to improve the sensitivity of the system, as opposed to traditional label-free sensing approaches that work based on changes in capacitance or charge, which are limited by screening. High salt concentration increases the conductivity of the media, which increases the baseline signal power and thus improves the overall signal-to-noise ratio. As a result, we were able to reliably and repeatedly detect target cytokines spiked in serum at concentrations as low as 100 fM with a dynamic range of three orders of magnitude within 10 minutes. In a practical setting, a single step involving a sample injection would be sufficient to perform a sample to answer analysis using the nanowell sensor. This ease of use can enable a plethora of applications ranging from medical diagnostics to environmental monitoring and food safety. We emphasize that while we only demonstrated singleplex detection using a leptin cytokine spiked in serum, the platform can be applied to a wide range of biomarkers. Multiplex analysis can be performed by fabricating an array of sensors, where each sensor is fabricated with antibodies targeting different proteins. The readout electronics utilized in this study consisted of a benchtop lock-in amplifier; however, a miniaturized portable or wearable lock-in amplifier could be used instead, with wireless transmission capabilities and a readout on a smartphone.

Chapter 4: Multiplexed protein assay measurements with embedded micro-processor

Advances in biosensor technologies for in vitro diagnostics have the potential to transform medical research. Many studies with high sensitivity and selectivity have been reported in the biosensor field over the past few decades. However, rare platforms can be ubiquitously performed in the clinical samples with high sensitivity and scalability. A major limitation confounding other technologies is a signal distortion that occurs in various matrices due to heterogeneity in high ion concentrations and a long elapse of time. We developed a nanowell sensor-based multiplexed protein assay that can perform cytokine detection with down to single pico-molar level sensitivity. The assay can be implemented with an embedded processor platform that enables multiple sensors simultaneously and can perform temporal measurements over a long period. We also performed the titration curve for multiple rat cytokines, including TNF- α , IL-4, and IL-10, with a dynamic range of five orders of magnitude.

4.1 Introduction

Medical decision making significantly relies on molecular testing. Quantitative detection of the specific proteins in serum and other bodily fluids is the cornerstone of many diagnostic tests to direct therapy in various areas of clinical medicine. [77][78][79][80] Protein array technologies provide a valuable platform for functional proteomic analysis, enabling comprehensive and high throughput studies. In the vast

majority of protein detection platforms, affinity-based biosensors are the most majority type, which detects proteins through the immobilization of probe molecules on a transducer substrate to attain specificity in detection of the target macromolecule of interest. [81] There are two major detection strategies, label-based and label-free, among affinity-based biosensing technologies. Label-based technologies typically advanced in detection limits and selectivity, yet require multiple steps. ELISAs [82], protein microarrays [83], and quantum dot [84] are some label based detection platforms; the readout is based on a fluorescent or colorimetric signal. Label-free techniques often have fewer steps while lag behind in detection limits and specificity compared to the label-based technique. Nanowires [85], micro-cantilevers [86], carbon nanotubes [87] and electrochemical biosensors [88] are several reported state-of-art techniques [89].

Both optical and electrical-based label-free biosensing technologies have shown significant promise in the laboratory setup and in the research reports, however, have experienced difficulty moving beyond the lab and even progressing to commercialization, or more critical clinical translation [90][91][92]. The ability to accurately assay biological samples to the extent where it can be used for reliably attaining measurements in animal or human studies requires minimizing measurement inconsistency, device variability, and also must be capable of accurate detection of biomarkers in biological matrices like blood, which is highly complex and has high salt concentration [93] [94]. For example, nanowires, micro-cantilevers, carbon nanotubes, and electrochemical biosensors rely on charge-based interactions between the protein or molecule of interest and the sensor, making each system unreliable in

conditions of varying pH and ionic strength. A 0.14 M salt solution (similar to human serum) has sufficient Debye screening, approximately 1 nm, to shield nanowires from detecting protein binding events of the capture antibody (10-20 nm). Accordingly, these sensors require a further step of present the samples in pure water or precisely controlled salt solutions, which brings difficulties to practical settings. For nanowires to detect proteins in serum samples, for example, desalting steps must be performed before detection. Therefore, transiting the highly sensitive and selective protein detection of an ideal buffer environment in the research setup into diverse biological matrices in the clinical settings posts the new challenges and difficulties [95] [96].

Although the complexity of a serum matrix poses challenges, our group developed an impedance-based nanowell sensor that can benefit from the higher salt concentration. A pair of overlapping electrodes has an insulation layer deposited between them. Within the overlapping area, a conductive path between the top electrode and the bottom electrode was created through a well array pattern, as Figure 4-1 shows.

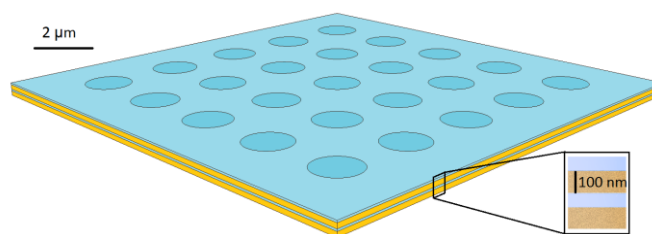


Figure 4-1 Nanowell Array Label-free Impedance sensor schematic

The impedance between the two electrodes is monitored in real-time and is affected by the molecules inside the well. Various types of probe antibodies can be immobilized inside the wells, as Figure 4-2 shows.

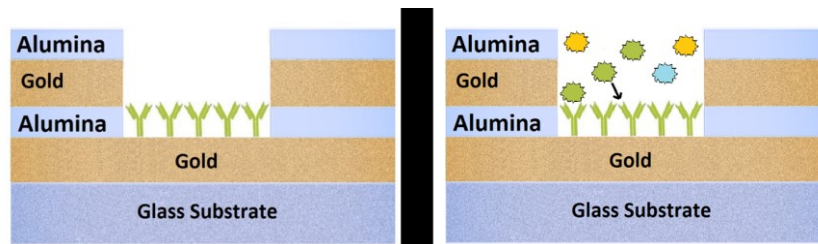
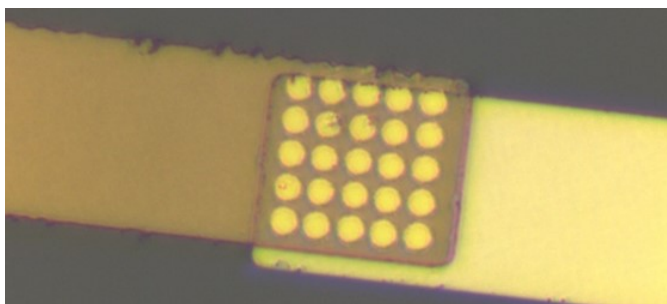


Figure 4-2 Nanowell Array Label-free Impedance sensor with antibodies and proteins

The impedance between the top and bottom electrodes would increase as the target protein molecules bind to the probe antibodies inside the wells, which is due to the partial occlusion of ions being conducted between the electrodes. The quantity of target protein exists in the matrix, and the well size of the array will determine the final amplitude of impedance increment. A higher salt concentration results in a larger current and thus higher signal power corresponding to larger changes in current due to protein binding, making the sensor ideal to quantify proteins in high salt content matrices, such as serum. Using a sensor chip containing an array of up to 28 sensors and implementing with an embedded microprocessor through the MUX chip, we conducted multiplexed cytokine detection and a series of titration experiments for each cytokine. Array photos are shown in Figure 4-3, and a photo of the device photo is shown in Figure 4-4.



Figure 4-3 Nanowell Sensor Array photo



*Figure 4-4 Device Sensor photo of 5*5 nanowells*

4.2 Materials and Methods

Sensor fabrication

The sensor fabrication began with patterning the bottom electrode on a glass wafer. The electrode was fabricated following standard photolithography, electron beam evaporation of metal, and lift-off processing. The metal layer consists of a 5 nm layer of chromium to enhance the adhesion of the gold film to the substrate and a 100 nm gold layer on top. A 40 nm layer of aluminum oxide was deposited onto the bottom electrode using atomic layer deposition. The top electrode (again consisting of 5 nm chromium and 100 nm gold) was patterned using the same procedure as for the bottom one. Another 40 nm layer of aluminum oxide was deposited on top of the top electrode using atomic layer deposition to serve as protection against fouling. A layer

of photoresist was spin-coated onto the wafer. An array of micron-sized holes was photo-patterned onto the overlapping area of the two electrodes. Multiple wet etch steps were performed to remove the top aluminum oxide layer (buffered oxide etchant), the gold and chromium layer (gold and chromium etchant), and the bottom aluminum oxide layer (buffered oxide etchant) inside the wells. The photoresist was then stripped off. A second photomask was used to pattern photoresist to protect the sensors to be able to etch off various parts of the alumina outside of the sensing region to expose the glass surface. Devices with a 20 μm x 20 μm overlapping area are shown in Figure 1D. A fluidic cell array made of PDMS to confine the liquid was then bonded on top of each sensor substrate using oxygen plasma treatment. The array consists of 4*7 single cells, with each fluidic cell being a millimeter in diameter, which allows for fluid to be directly incubated onto the substrate.

Reagent Preparation and Antibody Immobilization

Antibodies and target proteins were suspended in PBS. Monoclonal rat TNF-alpha antibodies (MAB510, R & D Systems) were suspended in PBS at a concentration of 0.5 mg/ml. The target cytokines used in this study were recombinant rat TNF-alpha protein (510RT, R & D Systems), recombinant rat IL-6 protein (506RL, R & D Systems), and recombinant rat IL-4 protein (522RL, R & D Systems) suspended in PBS at concentrations ranging from 10 fM to 1 nM. During the experiments, the target cytokine buffer was mixed with pure rat serum (R9759, Sigma Life Science) at a 1:1 ratio. We spiked the target cytokine in rat serum to test the effects of the background matrix on the sensor while ensuring that the endogenous levels of the

target cytokines (TNF- α , IL-6, and IL-10) that may or may not be present in the rat serum would not interfere with the sensor during control experiments. The antibodies were physically adsorbed onto the sensor surface by injecting 5 μ l of antibodies solution into the sensor well and incubating for 10 minutes.

Real-Time impedance sensor measurements

The real-time impedance sensor experiment started with pipetting 20 μ l 1x PBS into the well, which was made of PDMS to confine the liquid on the sensor. The complex impedance was monitored in real-time. This step changes the sensor environment from air into a high-conductivity electrolyte solution, resulting in a huge impedance decrease. Next, 5 μ l 1x PBS was injected into the well, serving as the negative control in the experiment. This was followed by injecting 5 μ l antibodies solution, 5 μ l non-target cytokines buffer, and 5 μ l target cytokines buffer into the sensor well sequentially. The impedance inside the nanowells was continuously measured using a multi-frequency lock-in amplifier (Zurich Instruments HF2IS). Each step lasted 10 minutes. The AC excitation source, providing 0.4 V at a frequency of 1 MHz, was connected to one of the electrodes, and the second electrode was connected to the input of the lock-in amplifier, where the real and imaginary components of the impedance were both acquired.

Titration curves of rat TNF- α , and IL-4, and IL-6

The titration curves experiment for the impedance sensor consisted of a series of real-time impedance sensor measurements with different concentrations of target

cytokines ranging from 10 fM to 1 nM. All measurements followed the same procedure as mentioned above; the only difference was the concentration of the target cytokine solutions. We also measured the titration curves with the commercially available Luminex kit MILLIPLEX® map high sensitivity t cell magnetic bead panel (MHSTCMAG-70K, EMD Millipore, Burlington, MA). We performed the Luminex test according to the provided protocol with standards run in triplicate and samples in duplicates.

Multiplexed protein assay measurements with embedded micro-processor

For multiplexed protein assay experiments, multiple sensors were activated in sequence via a MUX chip, which was controlled by an embedded microprocessor (Raspberry PI). The processor was programmed to sequentially enable a single output of the MUX chip, gathering the impedance information of the connected sensor one piece at a time. Next, a 1 nM TNF- α , IL- 4, and IL- 6 sample solution was pipetted into three different sensors simultaneously. The impedance information of all sensors was collected over all experiments.

Temporal profiling of cytokines with embedded micro-processor

Seven different concentrations of a TNF- α sample ranging from 1 pg/ml to 1 μ g/ml were pipetted into the sensor at different times in sequence. All sensors were functionalized with TNF- α antibodies using an identical process, each sensor was exclusively enabled via the MUX chip, and the impedance information of the sensor was obtained sequentially. Before adding the target cytokine samples into the sensor,

all sensors went through the non-target cytokine step, eliminating the non-specific binding interference.

4.3 Results and Discussion

Sensor performance characteristics

To evaluate the sensitivity and dynamic range of our assay, we compared titration curves obtained using our impedance sensor arrays to those obtained using the Luminex technique, the current gold standard in protein detection. Here, we decided to detect TNF- α , a well-known biomarker that plays a central role in inflammation, immune system development, apoptosis, and lipid metabolism. We spiked the target protein into a 1x PBS solution. To obtain high specificity, we immobilized a monoclonal capture antibody on a sensor surface, as Figure 4-5 shows.

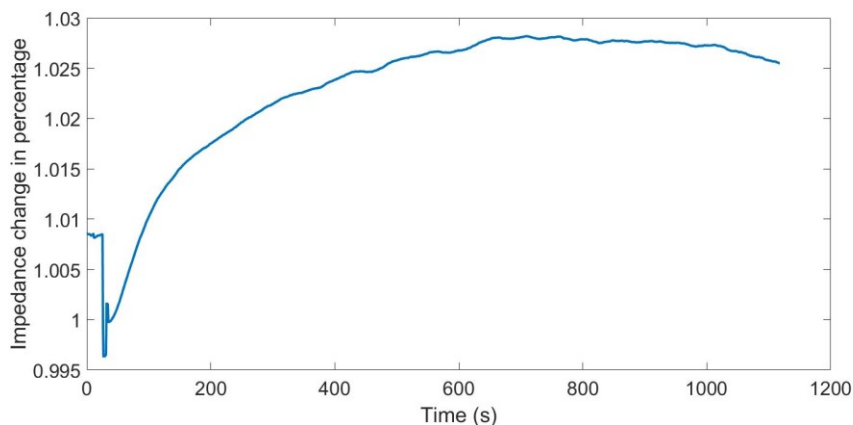


Figure 4-5 Normalized impedance measured using lock-in amplifier as adsorption of IL6 antibody to sensor surface

To eliminate the effects of the background matrix on the sensor, we mixed the spiked target protein solution with a pure rat serum matrix, as Figure 4-6 shows.

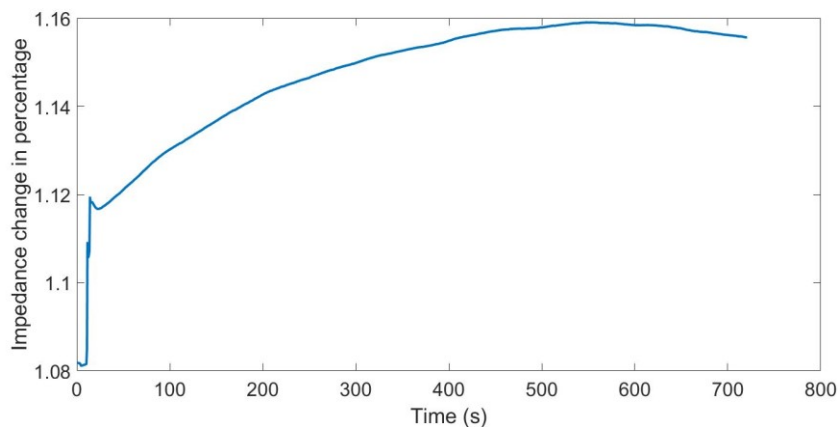


Figure 4-6 Normalized impedance measured using lock-in amplifier as binding of IL6 to IL6 antibodies

In both the Luminex and the impedance sensor assay, we used the same capture and detection antibodies (for the Luminex, the tag was streptavidin–horseradish peroxidase). We performed quantitative protein detection down to the single picogram per microliter. The trends of impedance change are different between the buffer with target cytokines and without target cytokines, as Figure 4-7 shows.

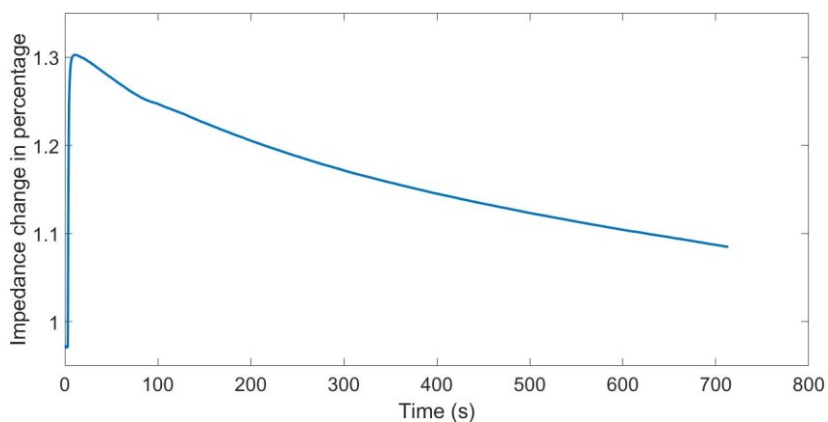


Figure 4-7 Input current of lock-in amplifier as the buffer without target cytokines

The impedance increases by about 3% to 4.5%, depending on the type of cytokine, while the negative control samples and the target cytokine-free samples have about

2% and 2.5% decreases, respectively. This happens in every single experiment, as Figure 4-8 shows.

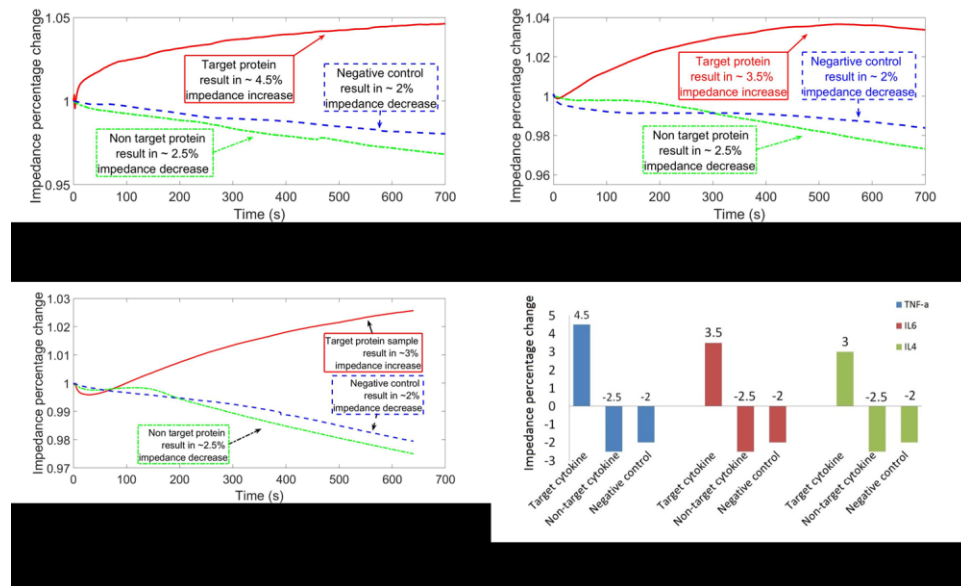


Figure 4-8 Impedance data measured by lock-in amplifier of multiple target proteins. A)

TNF- α , B) IL6, C) IL4, and D) Comparison among the listed 3 proteins

In addition, an examination of these data shows that our impedance nanosensors have linear calibration curves over five orders of magnitude, ranging from single pg/ml to tens ng/ml. We obtained similar performance characteristics in detecting IL-4 and IL-10, both of which play important roles in the acute phase reaction of inflammation.

The sensor response to serum matrix

Various exceptionally sensitive protein detection techniques using a variety of nanosensing technologies have been reported, such as nanowires, micro-cantilevers, carbon nanotubes, magnetic, and bio-barcode assays. A more substantial challenge, however, is the application of such sensitive protein detection to biological samples in non-ideal situations. A serum matrix is highly complex and has a high salt

concentration. This results in charge screening and minimizing the Debye layer thickness to approximately 1 nm, thus making E-fields unable to penetrate beyond the length of the capture antibody (10–20 nm). This represents a bottleneck for various techniques. However, the sensitivity of the impedance-based nanowell sensor benefits from the high salt concentration of the matrix. Higher salt concentration results in a larger current and thus higher signal power corresponding to larger changes in the current due to protein binding. As proteins bind to the antibodies inside the wells, the impedance between the two electrodes increases. This increase is due to the partial occlusion of ions passing between the electrodes. The quantity of target protein present in the serum will determine the ultimate drop-in current measured between the electrodes, as well as the impedance across the sensor electrodes. Furthermore, the blank controls in both PBS and serum yielded the same signal, indicating that the complexity of the serum matrix did not contribute any remarkable background noise to our sensors. These were the first major steps in confirming a matrix-insensitive detection platform.

Assay generalizability, which describes the sensing technique, can be used in different cytokines, such as TNF- α , IL-6, and IL-10. We next investigated the device's generalizability for diverse target cytokines by comparing the detection signal of different cytokines in PBS and serum, a more complex matrix. Detection signals were remarkably similar in the three cytokines over the entire range of protein concentrations tested. As Figure 4-9 a-c shows, IL-6, IL-4, and TNF- α all have a response to the samples whose concentration starting from a single pg/ml level and increase to about 4% impedance change at 100 ng/ml.

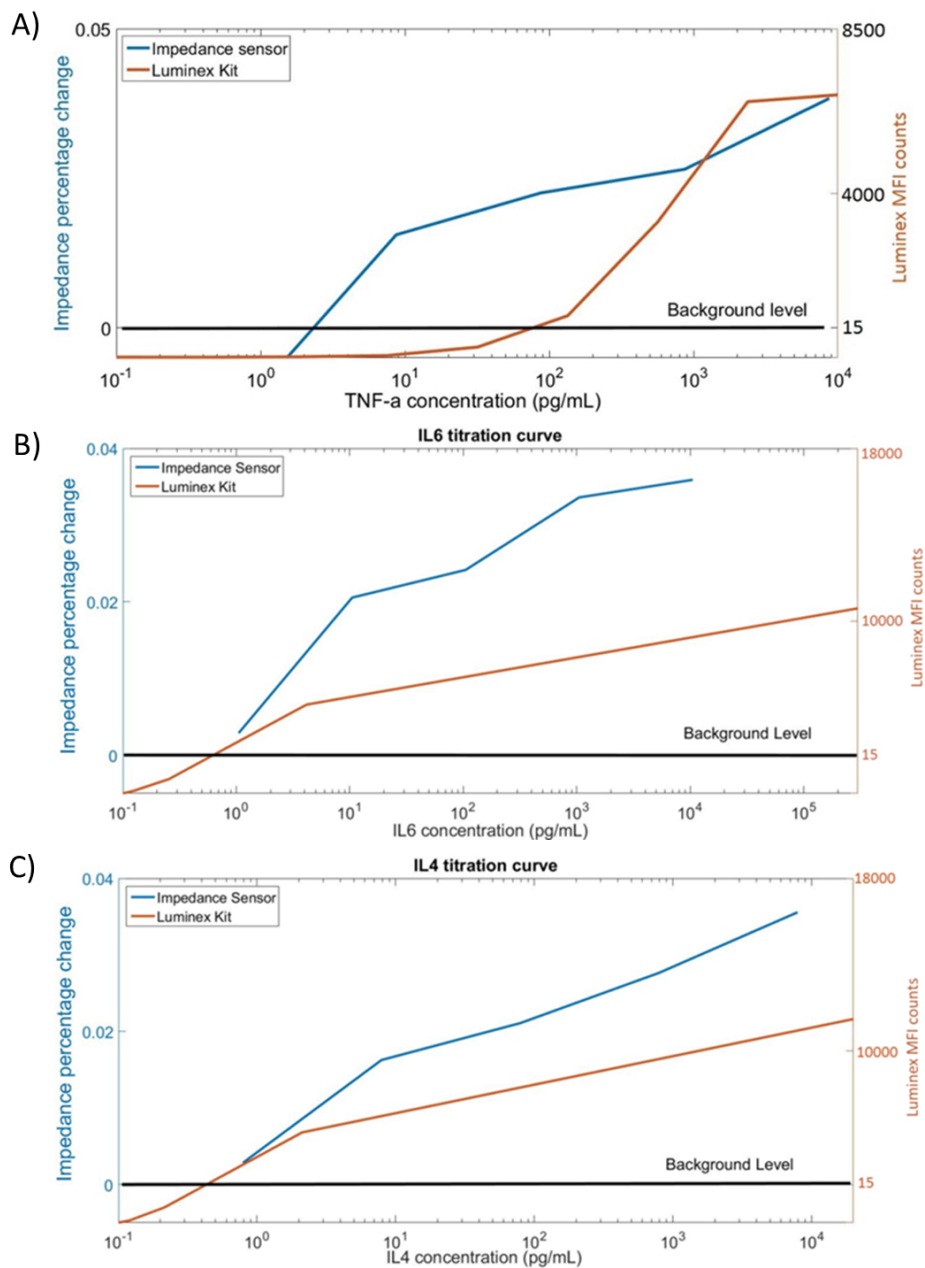


Figure 4-9 Titration curve of multiple proteins with comparison of nanowell sensor and

Luminex. A) TNF- α , B) IL6, and C) IL4

A first-order polynomial regression curve was found for each titration curve respectively and showed in Figure 4-10.

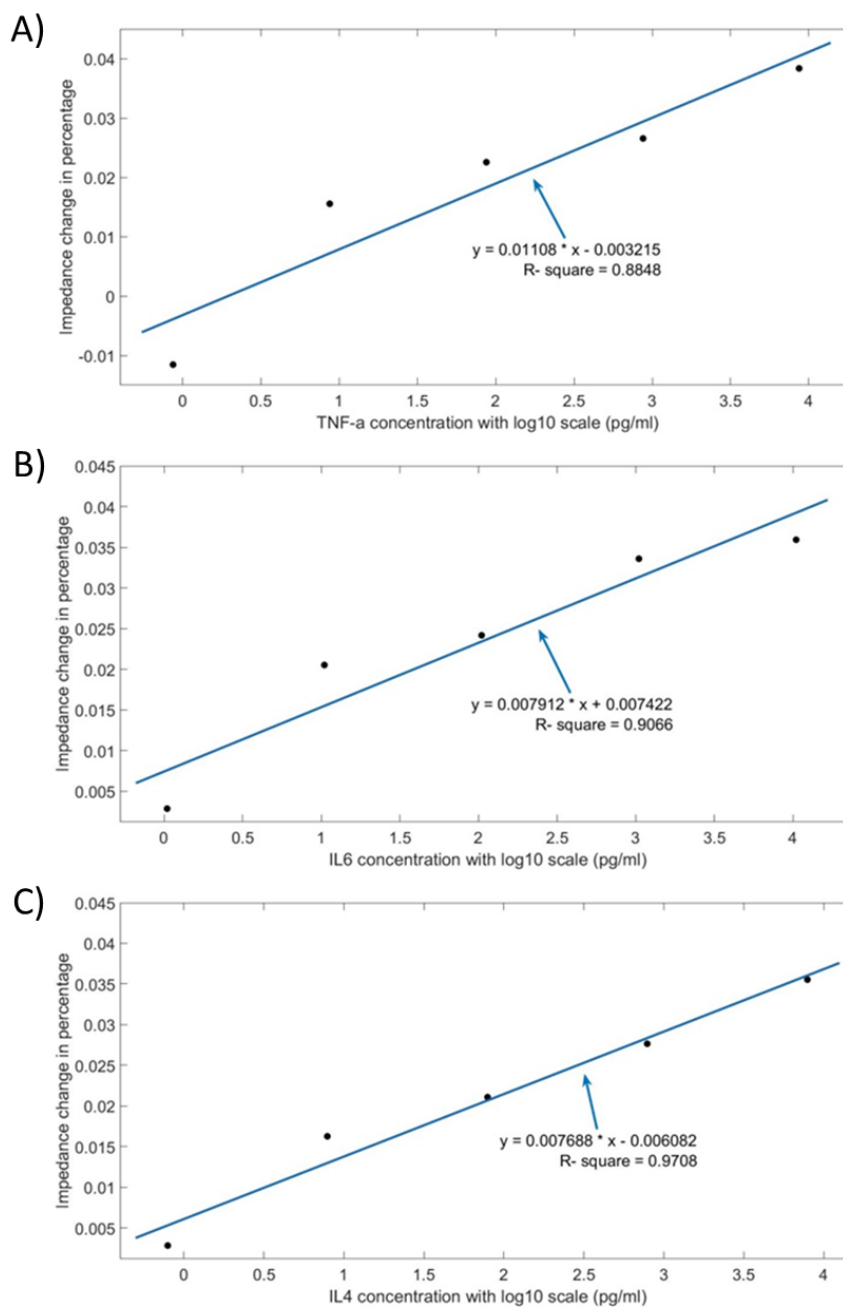


Figure 4-10 Regression models of multiple proteins from 1 pg/ml to 10 ng/ml. A) TNF- α , B) IL6, and C) IL4

Besides the R^2 of each regression curve labeled, the formula of impedance change in percentage (y in the formula) and the concentration of the target cytokine with log 10 scale (x in the formula) is also calculated.

The multiplex cytokines assay detection

A compelling application of our nanowell technology is the multiplex profiling over time of serum tumor markers in individuals with various cytokines. Rapid, sensitive, and multiplex diagnostic tools to monitor the progression of tumors will have a high impact not only on clinical diagnostics but also on biomedical research investigating key components in signaling pathways involved in tumor growth, invasion, and malignant transformation, as well as on monitoring response to therapies. The multiplexed cytokine detection platform we developed consists of three identical nanowell sensors. Each sensor functions with a single type of cytokine antibody, namely TNF- α , IL-4, and IL-6 antibodies for sensors A, B, and C, respectively, and impedance is measured sequentially. The three sensors all showed a virtually identical response when the target cytokine buffer was introduced to the sensor, as Figure 4-11 shows.

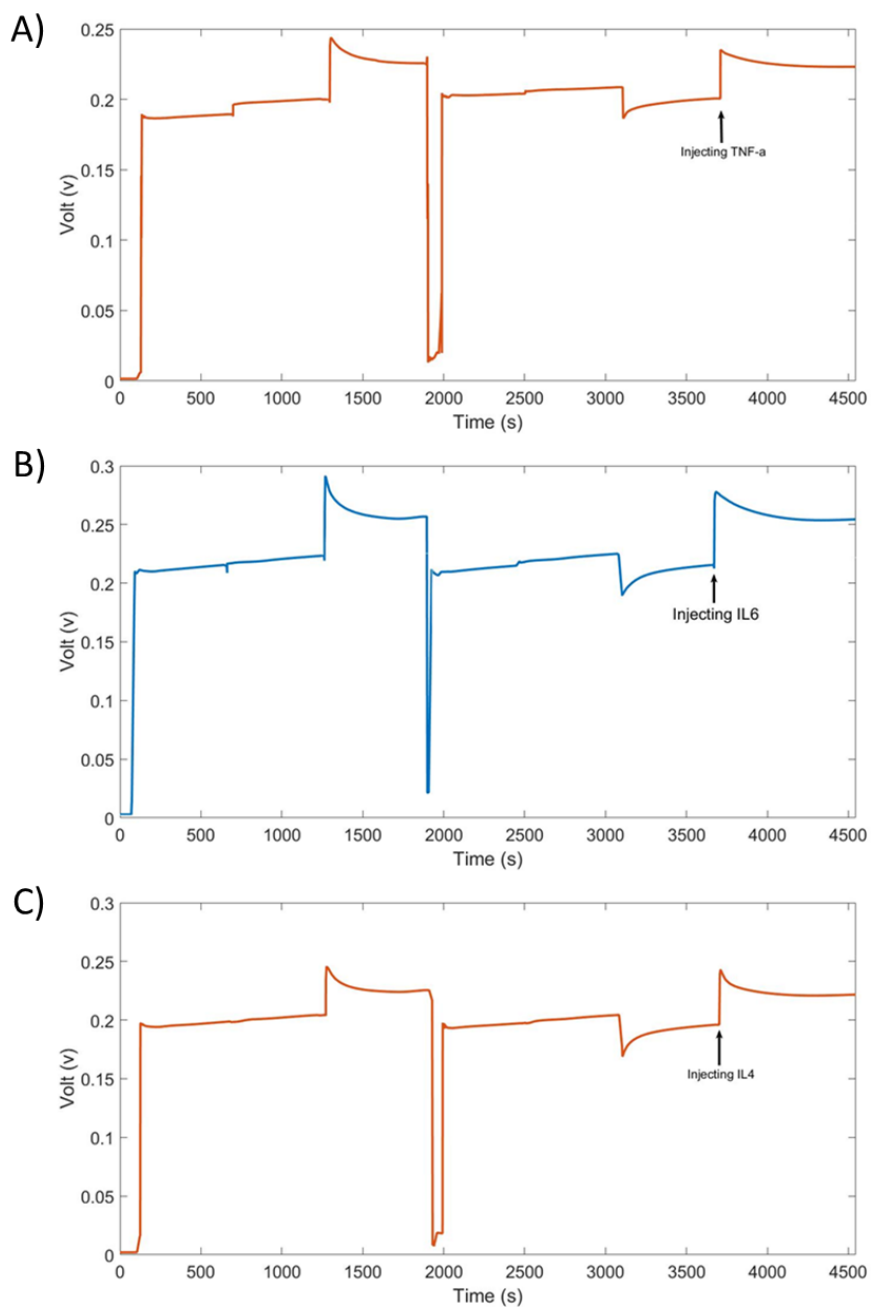


Figure 4-11 Output voltage of lock-in amplifier as the protein injected during the whole experiment process. A) TNF- α , B) IL6, and C) IL4

In addition, as we can see in Figure 4-11, a step of target-cytokine-free serum buffer was also injected into the sensor before the target cytokine spiked sample buffer as the negative control, and give the different pattern to the response of the target

cytokine spiked sample, which indicate the background non- target binding is not a significant disturbance.

Temporal cytokine profiling with embedded computer

We then applied our nanowell sensors to monitor real-time binding events of multiple concentration samples over a long period. We functionalized all the nanowell sensors with TNF- α antibody, a representative biomarker of inflammation, apoptosis, and immune system development. We analyzed a total of seven reaction conditions of the sensors simultaneously with the embedded computer platform. The impedance information of the seven sensors was measured sequentially; this was repeated periodically. The seven sensors were activated at different times by pipetting different cytokine samples into them. Additionally, target cytokine-free samples were introduced as negative controls and did not show a significant response; this means the non-target binding is not misleading the experiments. We observed a clear impedance increment in the sensors with a high concentration of target cytokines (sensors 4–7 in Figure 4-12) and a decrease in impedance for the sensors with a low concentration of target cytokines (sensors 1–3 in Figure 4-12).

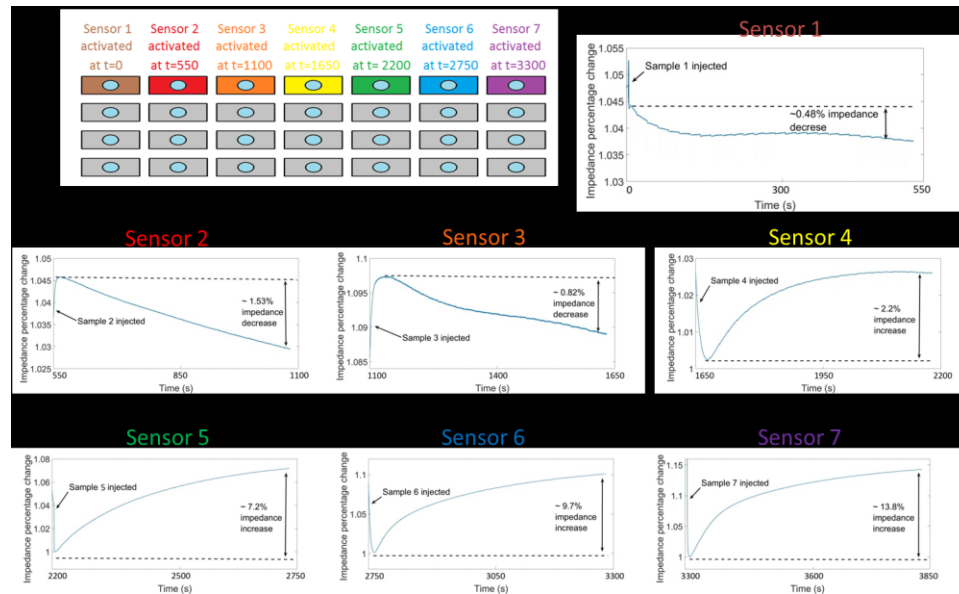


Figure 4-12 Temporal cytokine profiling with embedded computer controlled 7 sensors array

4.4 Conclusion

We present a novel label-free cytokine sensing platform that consists of sensor arrays and an embedded control component. The sensor arrays are made of 4×7 sensors, and each sensor is functionalized with an antibody in the nanowells and embedded with the electrodes which proceeding an impedance measurement as the target protein binds inside the wells. The key advantage of the nanowell sensor is that the sensor can benefit from the high salt concentration of serum, which results in improved sensitivity of the system and the availability of a combination of the technique to the in vivo clinical applications. High salt concentration increases the conductivity of the media, which increases the baseline signal power, thus improving the overall signal-to-noise ratio. In addition, the time-multiplexed measurement can be performed through the embedded control component, which sequentially enables the sensors immobilized with different antibodies. As a result, we were able to reliably and

repeatedly detect three types of multiplexed cytokines spiked in serum at concentrations as low as 300 fM with a dynamic range of three orders of magnitude. We also applied our nanowell sensors to monitor real-time binding events of multiple concentration samples over a long period through the embedded control platform. In a practical setting, a single step involving a sample injection would be sufficient to perform up to four different types of multiplexed samples for analysis using the sensor platform. This ease of use can enable a plethora of applications ranging from medical diagnostics to environmental monitoring and food safety. The readout electronics utilized in this study comprised a benchtop lock-in amplifier; however, a miniaturized portable or wearable lock-in amplifier could be used instead with wireless transmission capabilities and a readout on a smartphone.

Chapter 5: Quantification of mouse clinical samples with rheumatoid arthritis

Rheumatoid arthritis (RA) is an autoimmune and inflammatory disease where the immune system attacks healthy cells by mistake, causing inflammation of synovial cells. Causes and activation factors are still unclear, but CD4⁺ T cells are currently assumed to play a primary role. Cytokines also play indispensable roles in the process; for example, TNF- α and IL-6 contribute to joint inflammation in RA. The quantification of such cytokines can be very useful in monitoring the disease, analyzing the pathway behind it, and assessing the effects of therapy.

In this chapter, we obtained the titration curves of three different mouse cytokines, IL-6, TNF- α , and IL-10, built a regression model, and compared nanowell sensing to the Luminex technique. We tested 20 clinical mouse samples with RA and compared the nanowell sensing results to the other metrics.

5.1 Introduction

Rheumatoid arthritis (RA) is a chronic inflammatory disease characterized by swollen and tender joints and the progressive destruction of cartilage and bone, leading to significant morbidity and increased mortality [97]. The most common treatments are the use of traditional disease-modifying anti-rheumatic drugs (DMARDs), biologic agents, tofacitinib, and glucocorticoids, which usually target defined molecular and NOT adapt to individual treatment. Overdosing and under-dosing are common in such drug-based therapies [98]. The recently discovered cholinergic anti-

inflammatory pathway has been extensively studied because of its role in modulating the mammalian immune response and has enabled the development of a new therapeutic paradigm [99][100]. A robust neural-immune interaction in which peripheral nerves interact and communicate with the local environments and the effects on the activity of the immune system enables this pathway. It is postulated that in response to infection or injury, the parasympathetic vagus nerve transmits signals from the brain to the adrenergic splenic nerve, which interacts with splenic immune cells [101]. When the vagus nerve is stimulated by an electrical current, this neural-immune reflex is triggered, resulting in an inflammatory response to infection or tissue injury [102]. In some previous studies, Vagus nerve stimulation (VNS) has been reported to play a crucial pivot role in the reduction of in vivo cytokine production during endotoxemia in rat and mouse models, to be exact, a significant reduction of TNF, IL-1, and other cytokines. VNS has also been used to treat arthritis in animal models, in studies on inflamed joints, and even to treat RA in human patients [97][103][104]. In addition to implanted electrical stimulation, ultrasound-based therapy has also been shown to be an effective method for the splenic cholinergic anti-inflammatory pathway [105][106]. The quantification of some specific cytokines that play a crucial role in the inflammatory response to infection is a significant and effective method to assess the severity of disease and the effects of therapy.

We collaborated with the team lead by Dr. Hubert H. Lim and Dr. Daniel P. Zachs at the University of Minnesota. They provided 20 RA mouse samples. They applied ultra-sonicated therapeutic methods to these mice and measured them with several

metrics, such as ankle thickness and clinical score. In this study, we used a nanowell impedance sensor to quantify the specific cytokine levels of the clinical mouse samples, exploring the correlations between cytokine levels and the assessments of the corresponding RA mouse sample.

5.2 Titration curves of mouse cytokine IL6, TNF- α , and IL10

The quantification of cytokines, such as TNF- α and IL-6, helps in monitoring disease, the effects of treatment, and the pathology model. The methodology of quantification using the nanowell sensor is obtaining the titration curves of mouse IL-6, IL-10, and TNF- α using the standard concentration sample firstly, and deriving the regression model formula, and then analyzing the mouse serum sample with the nanowell quantification method, compared to other metrics. A series of titration curve experiments that describe the relationship between target protein concentration and sensor response was performed with target proteins (mouse TNF- α , IL-6, and IL-10). In each titration curve, six different concentrations were studied—60 fM, 600 fM, 6 pM, 60 pM, 600 pM, and 6 nM. We used the nanowell sensor to quantify the response at each concentration. The times series data of output voltage of mouse IL-6 as the target protein whose concentration ranging in 6 nM to 60 fM are shown in Figure 5-1 below. Figure 5-1 shows the sensor response to mouse IL-6 at different concentrations; 1a corresponds to 1nM, 1b corresponds to 100 pM, and so on.

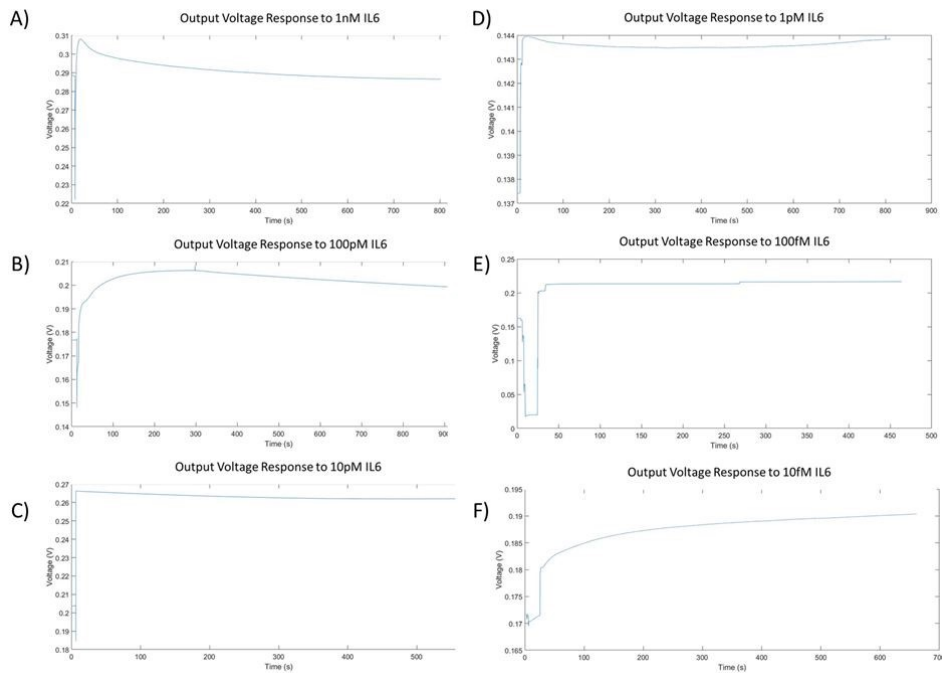


Figure 5-1 Output voltage response to different concentration of mouse IL6 samples. A) 1 nM, B) 100 pM, C) 10 pM, D) 1 pM, E) 100 nM, and F) 10 nM

We also looked at mouse TNF- α and mouse IL-10, both of which play a crucial role in the immune process response to RA. In addition to acquiring the titration curve of three different proteins using the nanowell sensor, we did the same using the gold standard Luminex technique and made a comparison. For the titration curves, we studied the response in terms of output voltage change in percentage for the nanowell sensor and the MFI (Median Fluorescent Intensity) reading for the Luminex technique as Figure 5-2, Figure 5-3, and Figure 5-4 shows. The titration curve of mouse IL-6 was triplicated at each concentration and the error bar was labeled.

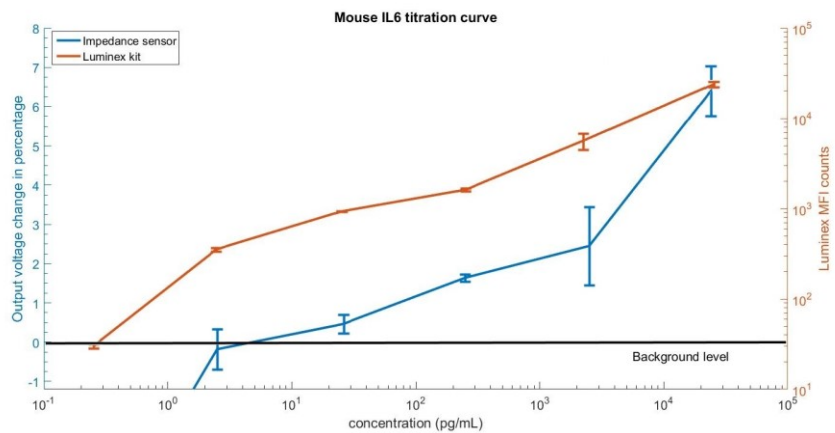


Figure 5-2 Titration curve of mouse IL6

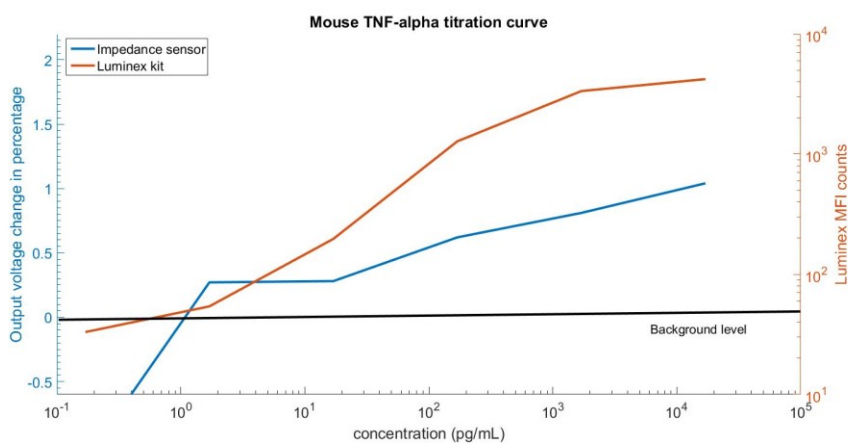


Figure 5-3 Titration curve of mouse TNF- α

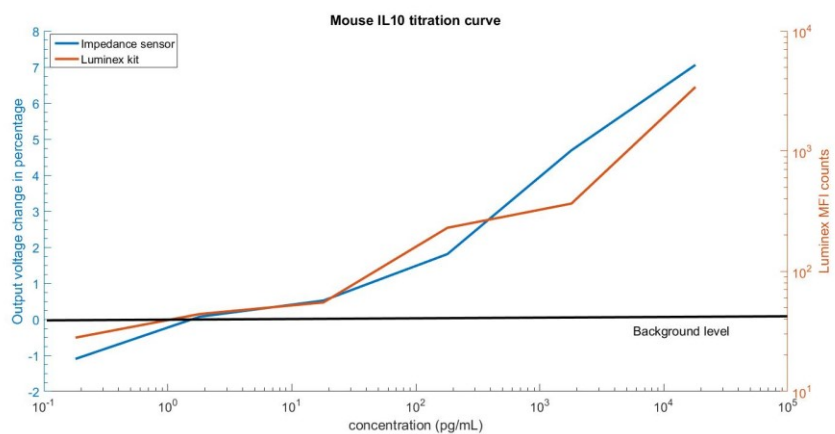


Figure 5-4 Titration curve of mouse IL10

As we can see in the titration curves above, both the nanowell impedance sensor and the Luminex technique show a wide dynamic range from about single pM to single nM. The nanowell impedance sensing is comparable to the Luminex technique.

5.3 Study of Clinical sample of the mouse with rheumatoid arthritis

The study of clinical RA mouse samples requires quantifying the target protein concentration in the samples. A regression model based on the titration curves of specific target proteins shown previously was analyzed using MATLAB to find the optimized fitting curve and formula. Regression models of the Luminex technique were also built for each protein. Figures 5-5, Figure 5-6, and Figure 5-7 below show the regression model of mouse IL-6, TNF- α , and IL-10 using both the nanowell sensor and the Luminex technique.

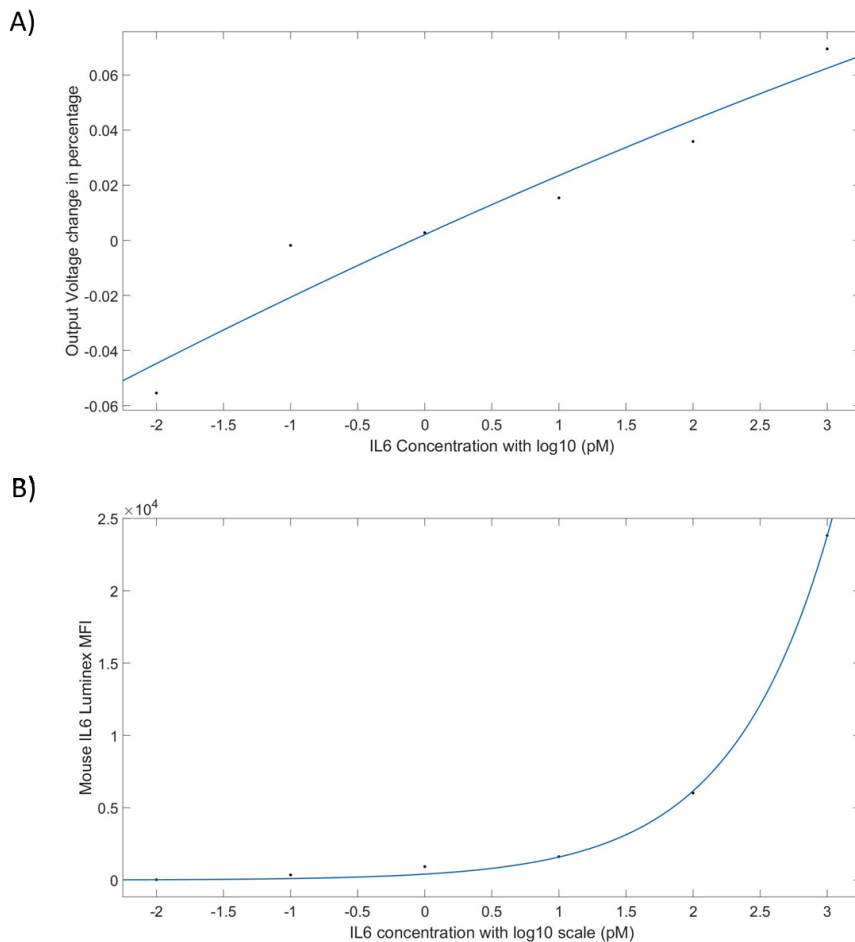


Figure 5-5 Regression model curve of mouse IL6 with A) Nanowell and B) Luminex

The formula of nanowell sensor response in terms of output voltage change in percentage and the concentration is derived based on the regression model using experimental results above.

$$Y = 0.02144 * X + 0.0003245$$

Where Y is the predicted output voltage change in percentage and X is the concentration of IL6 with a log10 scale in pM. $R^2 = 0.9241$ for the above regression model.

The formula of Luminex response in terms of Luminex MFI and the concentration based on the regression model using experimental results above is also derived.

$$Y = 412.8 * e^{1.351 * X}$$

Where Y is the predicted Luminex MFI, and X is the concentration of IL6 with a log10 scale in pM. $R^2 = 0.9992$ for the above regression model.

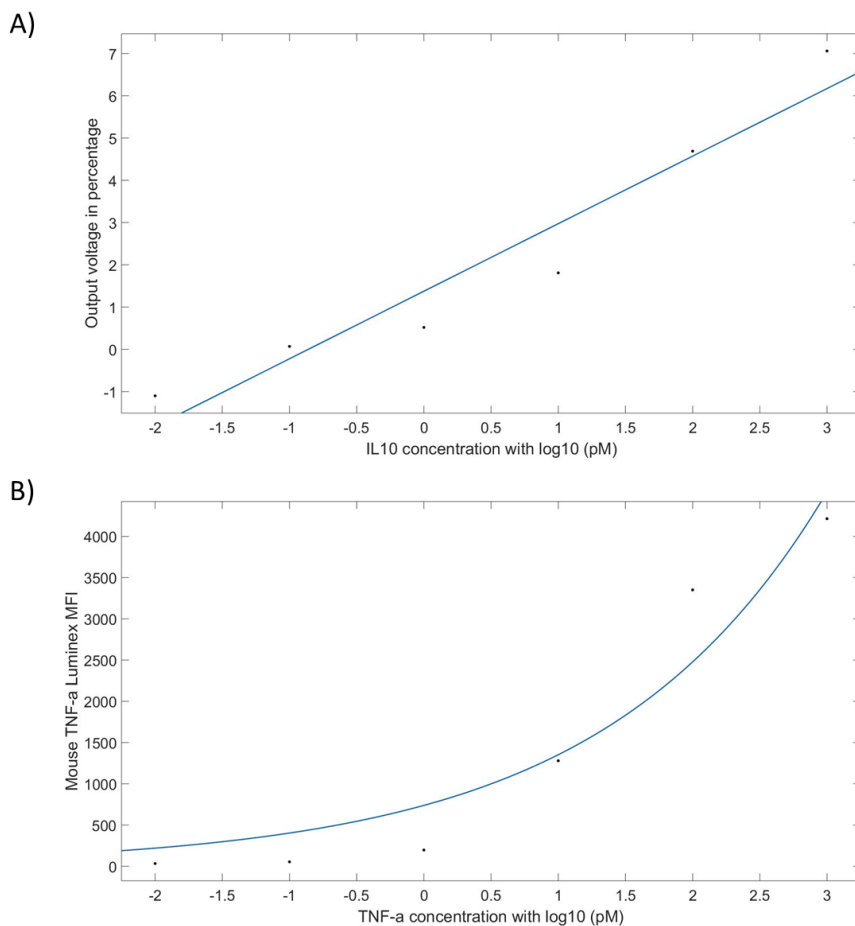


Figure 5-6 Regression model curve of mouse TNF- α with A) Nanowell and B) Luminex

The formula of nanowell sensor response in terms of output voltage change in percentage and the concentration is derived based on the regression model using experimental results above.

$$Y = 0.3601 * X + 0.1368$$

Where Y is the predicted output voltage change in percentage and X is the concentration of TNF- α with log10 scale in pM. $R^2 = 0.9241$ for the above regression model.

The formula of Luminex response in terms of Luminex MFI and the concentration is derived based on the regression model using the experiment results above.

$$Y = 738.1 * e^{0.6056 * X}$$

Where Y is the predicted Luminex MFI, and X is the concentration of TNF- α with a log10 scale in pM. $R^2 = 0.9211$ for the above regression model.

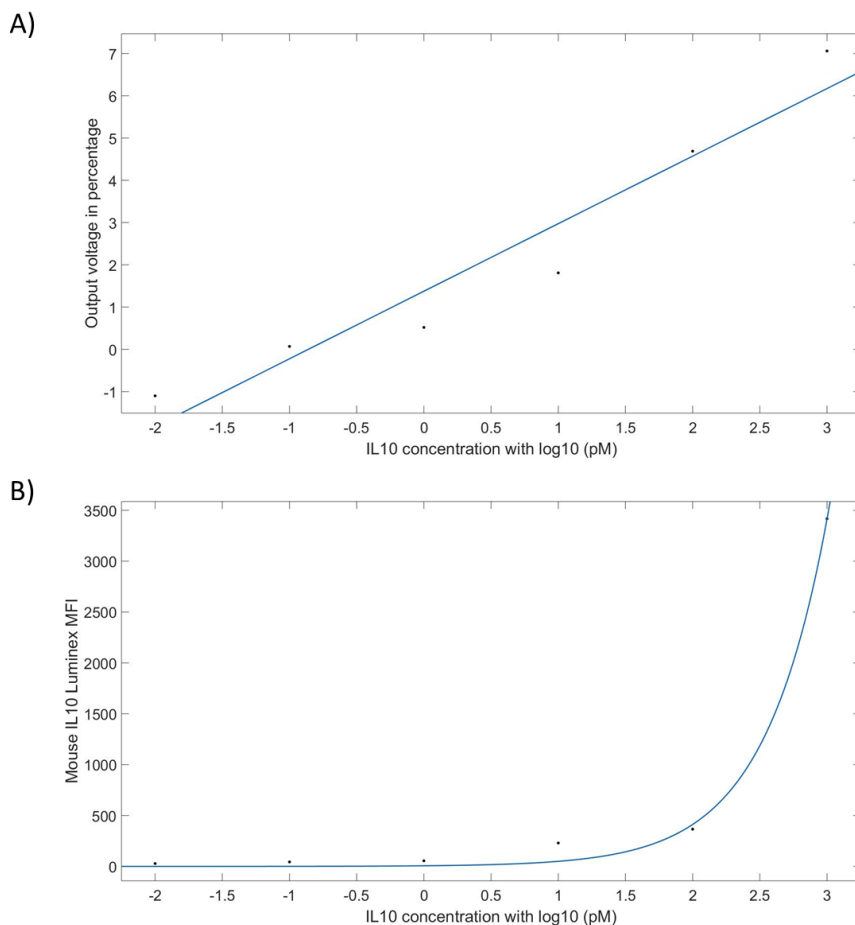


Figure 5-7 Regression model curve of mouse IL10 with A) Nanowell and B) Luminex

The formula of nanowell sensor response in terms of output voltage change in percentage and the concentration is derived based on the regression model using experimental results above.

$$Y = 1.599 * X + 0.1376$$

Where Y is the predicted output voltage change in percentage and X is the concentration of IL10 with log10 scale in pM. $R^2 = 0.9275$ for the above regression model.

The formula of Luminex response in terms of Luminex MFI and the concentration is derived based on the regression model using the experiment results above.

$$Y = 6 * e^{2.115*X}$$

Where Y is the predicted Luminex MFI, and X is the concentration of IL10 with a log10 scale in pM. $R^2 = 0.9956$ for the above regression model.

After achieving the regression model formula for IL-6 with the nanowell sensor and the Luminex technique, we found a correlation curve between predicted concentration with the nanowell sensor and the Luminex technique, as shown in Figure 5-8 below.

We also compared the predicted concentration of the nanowell sensor and the Luminex technique to the standard concentration by putting the standard concentration into the corresponding regression model formula, as shown in Figure 5-9 below.

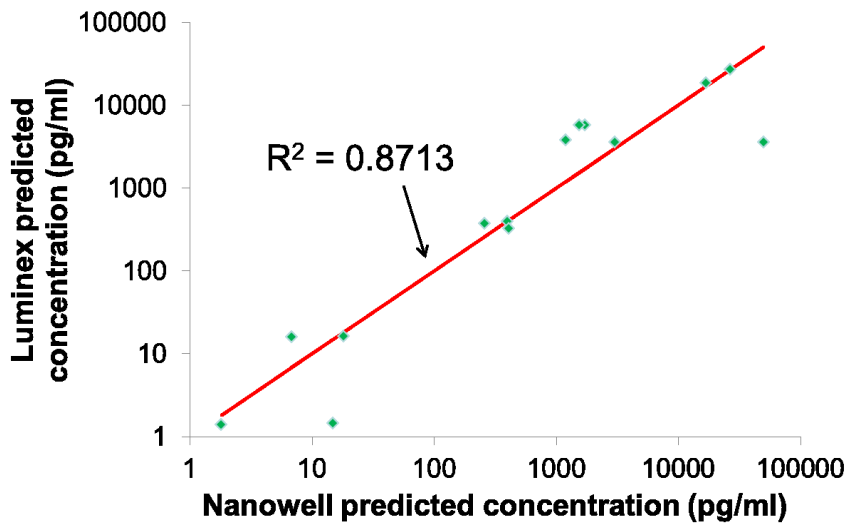


Figure 5-8 Correlation curve between predicted concentration with nanowell sensor and with Luminex

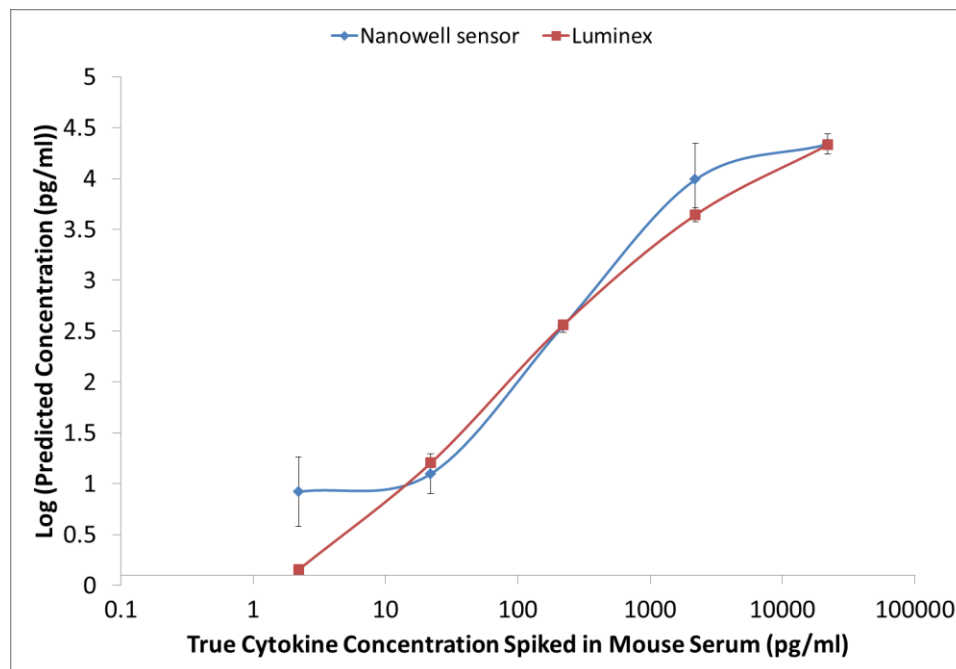


Figure 5-9 Comparison between prediction of standard concentration sample using nanowell sensor and Luminex

We can see that the two methods have a high correlation coefficient, which indicates the methods are comparable and of the same quality in terms of sensitivity.

The mouse clinical samples were provided by the team leaders Dr. Hubert H. Lim and Dr. Daniel P. Zachs at the University of Minnesota. They provided 20 RA mouse samples. They applied ultra-sonicated therapeutic methods to these mice and measured them with several metrics, such as ankle thickness and clinical score.

We then compared the cytokine quantification with ankle thickness and clinical score. Ankle thickness was measured with a caliper, as is standard in rodent models of arthritis. A higher value means severe inflammation. Ankle thickness changes were measured with a caliper, and composite clinical scores were determined based on the established method of assessing rodent arthritis severity on a 0-12 scale; in brief, each paw was assigned a clinical score between 0 and 3, with 0 indicating no swelling. Figure 5-10 shows the response of the nanowell sensor with respect to ankle thickness, and Figure 5-11 shows the response of the nanowell sensor with respect to clinical scores.

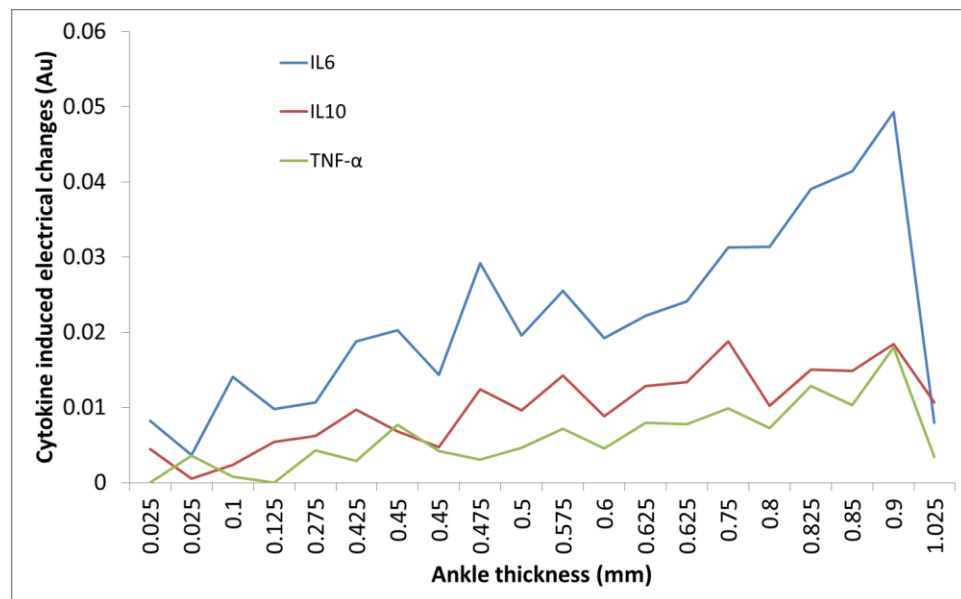


Figure 5-10 Response of nanowell sensor wrt ankle thickness of clinical mouse samples

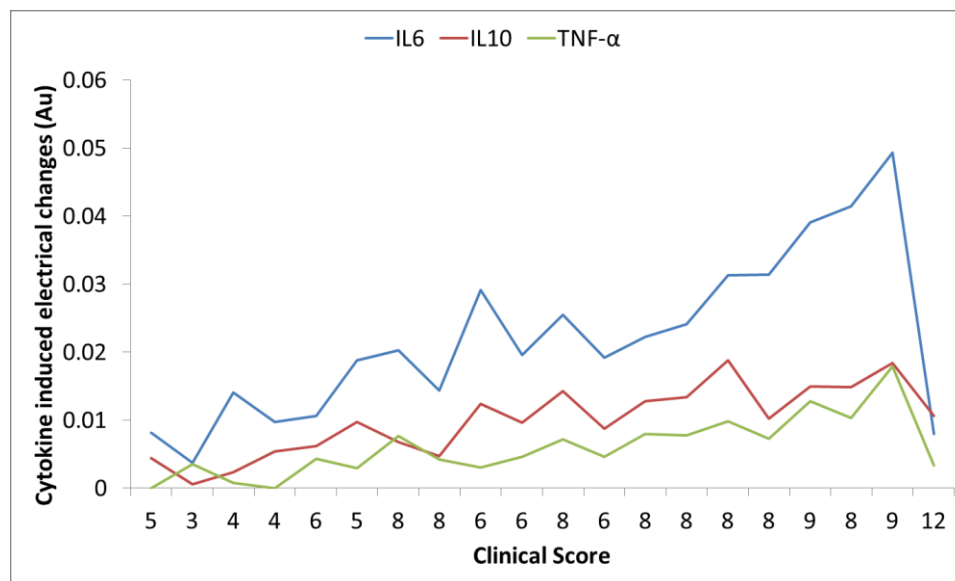


Figure 5-11 Response of nanowell sensor wrt clinical score of clinical mouse samples

The RSQ (Correlation Coefficient) between the cytokine-induced electrical change in IL-6, TNF- α , and IL-10 with respect to ankle thickness is 0.826162178, 0.722093006, and 0.768111568, respectively. The RSQ coefficient between the cytokine-induced electrical change in IL-6, TNF- α , and IL-10 with respect to clinical score is 0.59470324, 0.667842607, and 0.582194163, respectively.

All three types of cytokines show an increasing trend in terms of the increment in ankle thickness, which indicates the severity of arthritis. Mice with severe RA tend to have a higher level of cytokines.

5.4 Conclusion

We obtained the titration curves of mouse IL-6, TNF- α , and IL-10 that describe the relationship between the nanowell sensor responses in terms of output voltage change

and the target protein concentration. All three titration curves showed a wide dynamic range over three orders of magnitude and similar precision and sensitivity compared to the Luminex technique. We also built regression models for the three mouse cytokines and used the model to analyze the clinical mouse samples with arthritis. We also found correlations between the nanowell sensing results and other metrics for all 20 mouse samples.

Chapter 6: Quantification of human clinical samples with inflammatory arthritis

In this chapter, I discuss some of my most recent results of the study on the cytokines TNF- α , IL-6, and IL-10 as biomarkers. The results include the model predictions using the model discussed in Chapter 2, titration curves of each cytokine using standard concentration samples, a comparison of titration curves between the nanowell sensor and the gold standard Luminex technique, the regression model, and concentration prediction formulas based on the titration curves of each cytokine, and the results of human sample measurements.

6.1 Introduction

Inflammatory cytokines and chemokines, such as IL-6, TNF- α , and IL-1, are immediately produced in response to infections and tissue injuries and contribute to host immune through the stimulation of acute-phase responses, hematopoiesis, and immune reactions [107] [108] [109][110]. The serum level of such cytokines and chemokines in patients is an informative indicator of the severity of the disease, including asthma [111], visceral disease [112], arthritis [113] [101], and respiratory syndrome including SARS, MERS, and COVID-19 [114] [115][116]. A rapid, accurate, and reliable protein assay is necessary to quantify the target cytokine level, to observe the effects of drug treatments, to make treatment decisions, and to obtain a better understanding of the disease. A nanowell impedance sensor can be utilized

with different cytokines and provides a single pg/ml level detection in a single step of sample to answer setup, which makes the technique, is a good candidate.

6.2 Modeling and standard titration curve

First, we compared the results of the titration curves of the nanowell sensor and the gold standard Luminex technique for all three types of proteins, TNF- α , IL-6, and IL-10 of humans. Both curves are performed at five different concentrations ranging from 0.1 pg/ml–1000 pg/ml, with triplicate experiments of each concentration. Figures 6-1 through 6-3 show the titration curves of both the nanowell impedance sensor and the Luminex technique for TNF- α , IL-6, and IL-10, respectively. In each figure, the results of the nanowell sensor in terms of impedance change in percentage are indicated by blue columns, while the Luminex results in terms of MFI counts with log scale are indicated by a red line.

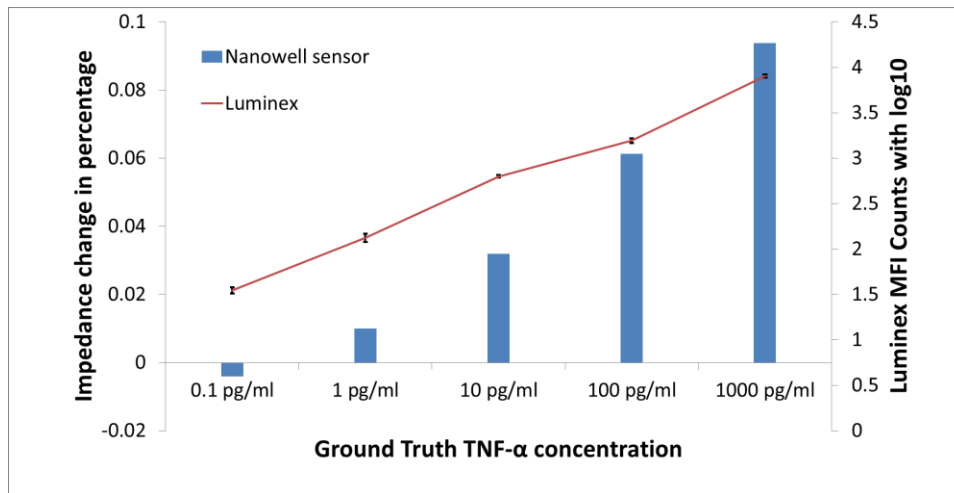


Figure 6-1 Titration curves of human TNF- α with nanowell sensor and Luminex

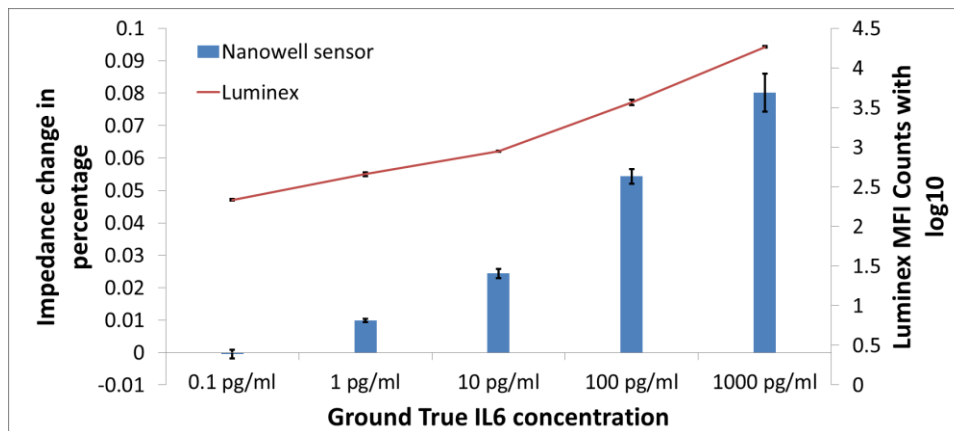


Figure 6-2 Titration curves of human IL6 with nanowell sensor and Luminex

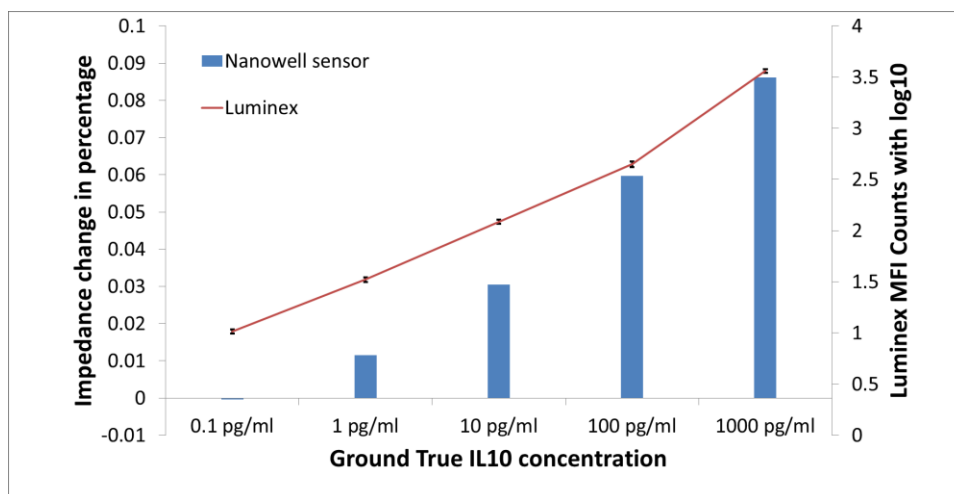


Figure 6-3 Titration curves of human IL10 with nanowell sensor and Luminex

According to the theory, total impedance change is equal to the impedance change due to single protein binding times the binding amount,

$$\Delta R_{total} = N_{eq} * R_p$$

and

$$N_{eq} = b_{eq} * A,$$

where b_{eq} is the surface concentration of bond receptors on the sensor; typical active binding sites' density ranges from 10^9 – $10^{12}/cm^2$. A is the sensor surface area. Given a range of active binding site density, the fraction of bound receptors in equilibrium b_{eq} is a function of bulk concentration,

$$\frac{b_{eq}}{b_m} = \frac{c_0/K_D}{1 + c_0/K_D} \equiv \frac{\tilde{c}}{1 + \tilde{c}}$$

where $\tilde{c} = c_0/K_D$ is the concentration, non-dimensionalized by the natural concentration scale K_D . Thus,

$$N_{eq} = b_{eq} * b_m * A = \frac{c_0/K_D}{1 + c_0/K_D} * b_m * A .$$

However, impedance change due to single protein binding R_p , which derived in chapter 2,

$$R_p = \frac{4\rho d_p^3}{N\pi D^4},$$

where d_p is the diameter of the equivalent volume sphere equals 8.1 nm, N is the number of nanowells (25 in this case), and D is the electrical effective well diameter (592 nm).

Bringing everything together, we have

$$\Delta R_{total} = N_{eq} * R_p = \frac{c_0/K_D}{1 + c_0/K_D} * b_m * A * \frac{4\rho d_p^3}{N\pi D^4} = \frac{c_0}{K_D + c_0} * Const.$$

Total impedance change ΔR is a function of the bulk concentration of the target protein, which follows the format of

$$\Delta R \propto \frac{c_0}{K_D + c_0} * Const = \frac{A * c_0 + B}{C * c_0 + D}.$$

If we quantify the impedance change with percentage, defined as $\Delta R/R_s$, where R_s is the original resistance of the solution, is also a constant. We can find that it is still a function of the bulk concentration of the target protein c_0 , following the format above. The formula of impedance change in percentage and the concentration of TNF- α is then derived based on the regression model using the experiment results above. In

$$Y = \frac{0.1 * X + 0.6369}{X + 72.94}$$

Y is the predicted impedance change in percentage, and X is the concentration of the sample in pg/ml. The regression model curves of TNF- α are shown in Figures 6-4 and 6-5 below.

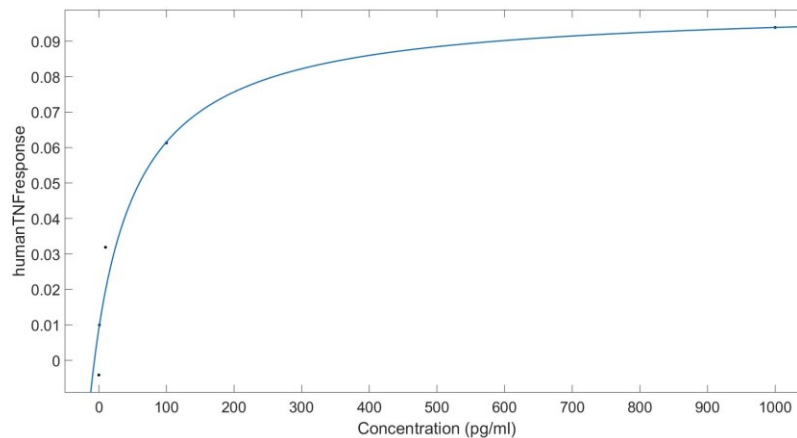


Figure 6-4 regression model curve of TNF- α with nanowell sensor

The formula for the Luminex MFI counts and the concentration is derived based on the regression model using the experiment results above. In

$$Y = \frac{1.578 \times 10^4 * X + 9147}{X + 3.053}$$

Y is the predicted Luminex MFI count, and X is the concentration of the sample in pg/ml.

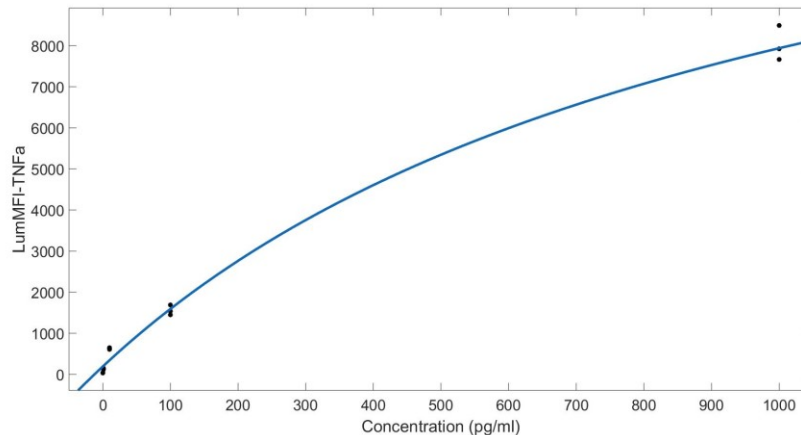


Figure 6-5 regression model curve of TNF- α with Luminex

Likewise, the formula for impedance change in percentage and the concentration of IL-6 is derived based on the regression model using the experiment results above. In

$$Y = \frac{0.08162 * X + 0.4227}{X + 52.94}$$

Y is the predicted impedance change in percentage, and X is the concentration of the sample in pg/ml. The regression model curves of IL-6 are shown in Figures 6-6 and 6-7 below.

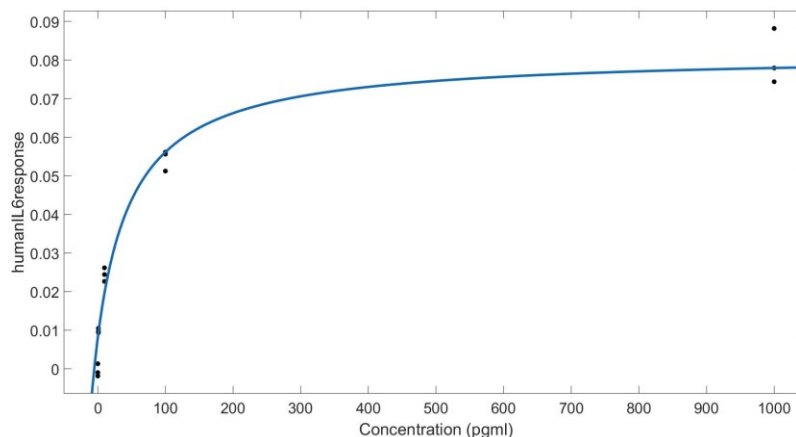


Figure 6-6 regression model curve of IL6 with nanowell sensor

The formula for Luminex MFI counts and the concentration is derived based on the regression model using the experiment results above. In

$$Y = \frac{4.065 \times 10^4 * X + 5.245 \times 10^5}{X + 1209}$$

Y is the predicted Luminex MFI counts of IL-6, and X is the concentration of the sample in pg/ml.

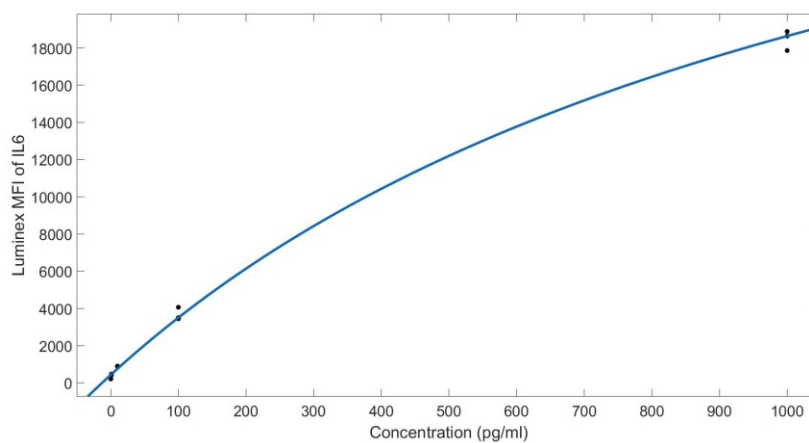


Figure 6-7 regression model curve of IL6 with Luminex

Last, the formula of impedance change in percentage and the concentration of IL-10 is derived based on the regression model using the experiment results above. In

$$Y = \frac{0.08463 * X + 0.1588}{X + 29.9}$$

Y is the predicted impedance change in percentage, and X is the concentration of the sample in pg/ml. The regression model curves of TNF- α are shown in Figures 6-8 and 6-9 below.

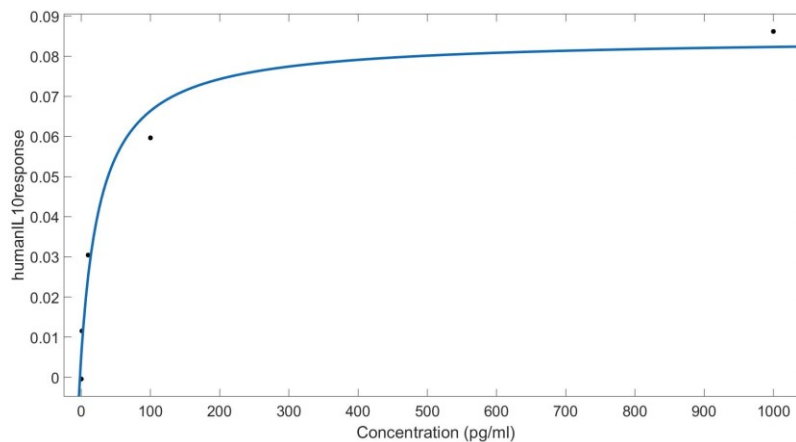


Figure 6-8 regression model curve of IL10 with nanowell sensor

The formula for Luminex MFI counts with a log10 scale and the concentration is derived based on the regression model using the experiment results above. In

$$Y = \frac{2.023 \times 10^4 * X + 1.811 \times 10^5}{X + 4804}$$

Y is the predicted Luminex MFI counts of IL-10, and X is the concentration of the sample in pg/ml.

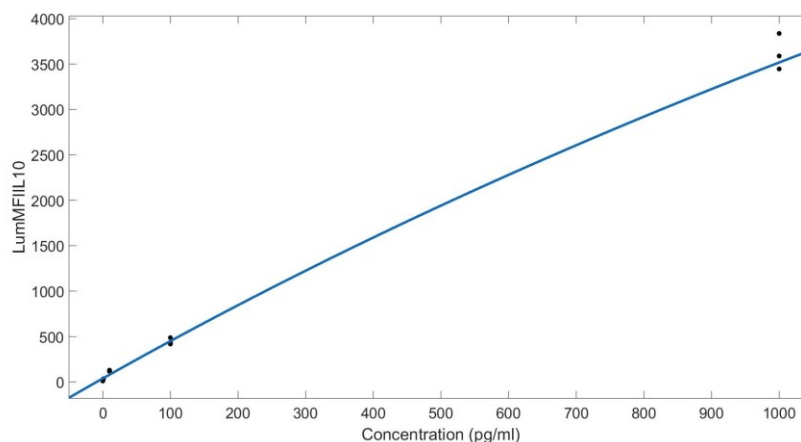


Figure 6-9 regression model curve of IL10 with Luminex

After deriving the formula of each protein and method, we plugged the standard concentration into the formula to show its accuracy, as Figures 6-10, 6-11, and 6-12 show. The horizontal axis is the ground truth concentration ranging from 0.1 pg/ml–1000 pg/ml, while the vertical axis is the predicted concentration with a log₁₀ scale in pg/ml.

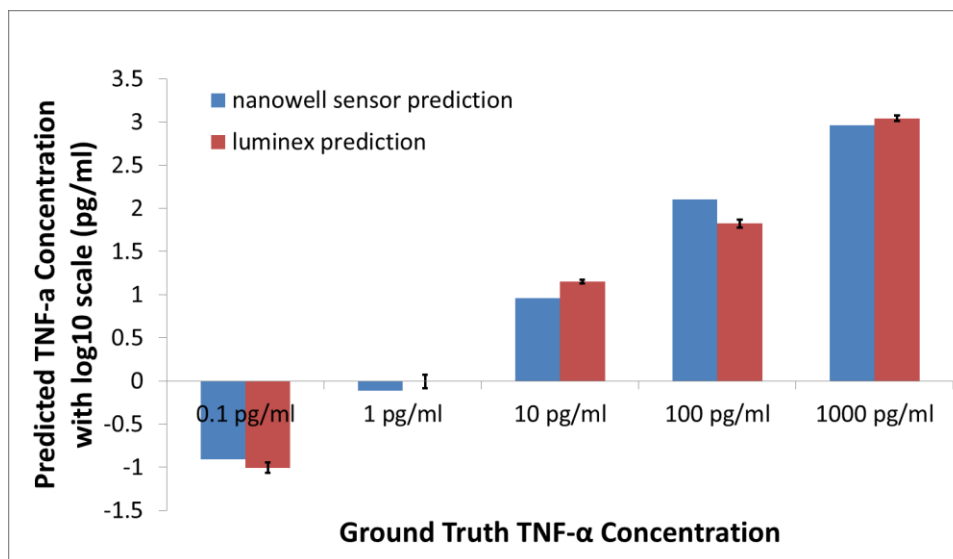


Figure 6-10 Prediction of standard concentration sample of TNF- α

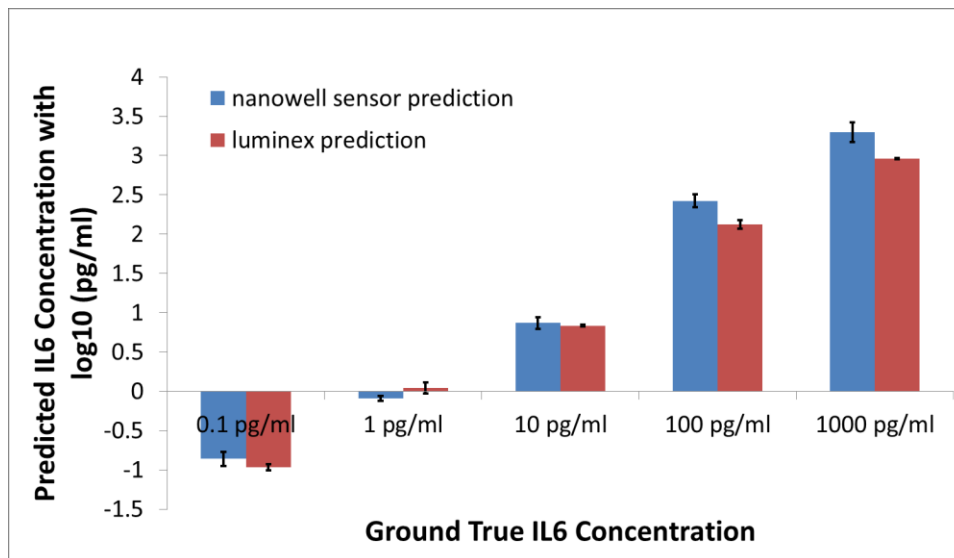


Figure 6-11 Prediction of standard concentration sample of IL6

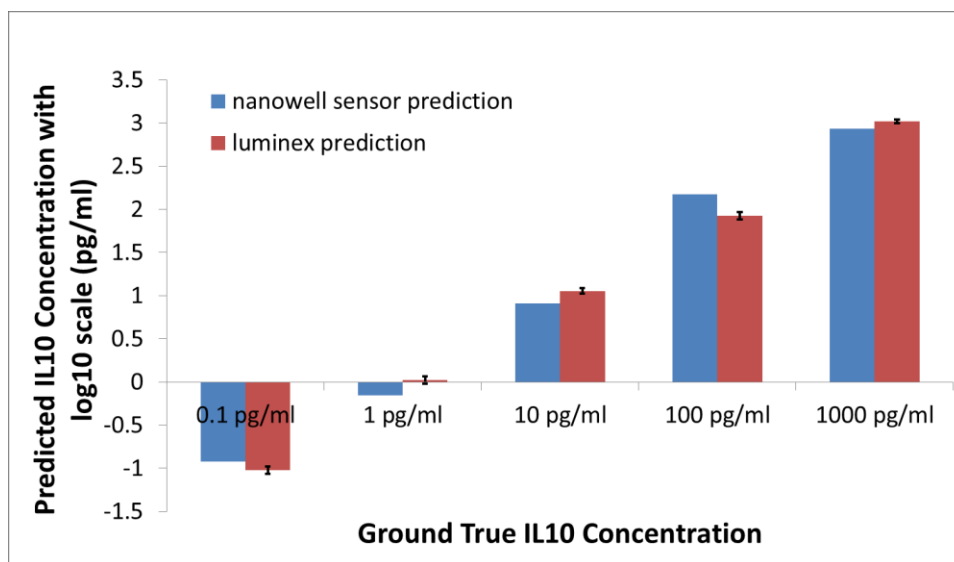


Figure 6-12 Prediction of standard concentration sample of IL10

As shown above, the predicted results of the standard concentration of all three types of protein for both the nanowell sensor and the Luminex technique are comparable and relatively accurate.

6.3 Quantification of cytokine level with human samples

After deriving the formula of the regression model of each titration curve, we established the connection between the measured values of the nanowell sensor and the Luminex technique to the concentration of specific target proteins, TNF- α , IL-6, and IL-10. We then moved to the human sample measurements. The human samples were provided by Dr. Hubert Lim's lab at the University of Minnesota. There are 12 patients in total, with four samples of different time points for each patient. The samples from patient 3, patient 6, and patient 7 comprise the sham group, which is also the control group. The rest of the samples comprise the stim group (patients received therapy). The samples are the serum sample of patients on day 1, day 7, day 14, and day 21. Each sample was measured with the nanowell sensor and the Luminex technique, and then its concentration was calculated using the regression formula shown in previous paragraphs. Figure 6-13 shows representative results for all three types of protein for a single patient at four-time points.

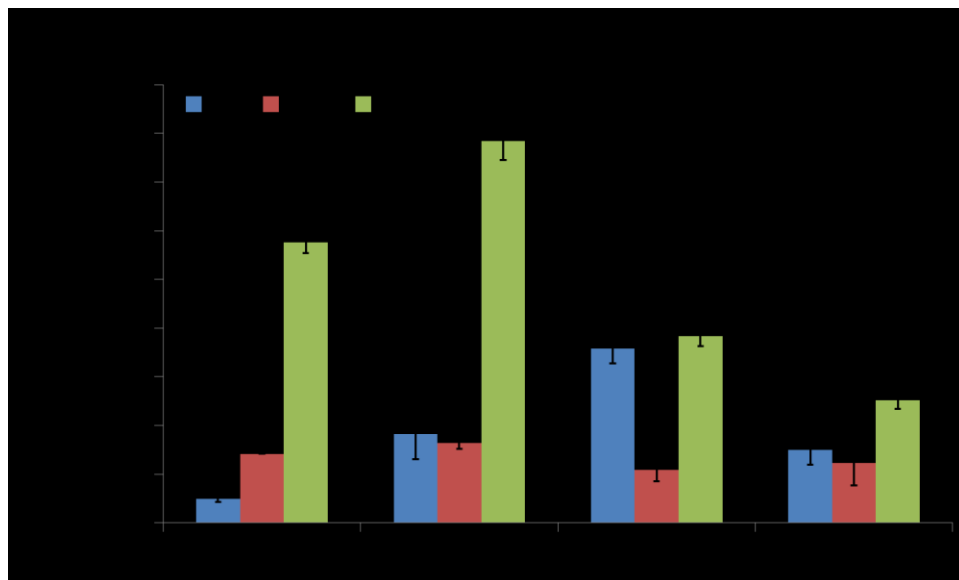


Figure 6-13 Representative results of all 3 proteins of single patient

Figure 6-14 shows a comparison of the calculated concentration of IL-6 between the nanowell sensor and the Luminex technique for the same patient as above. There are four samples at different time points, and each sample is measured duplicate of both techniques.

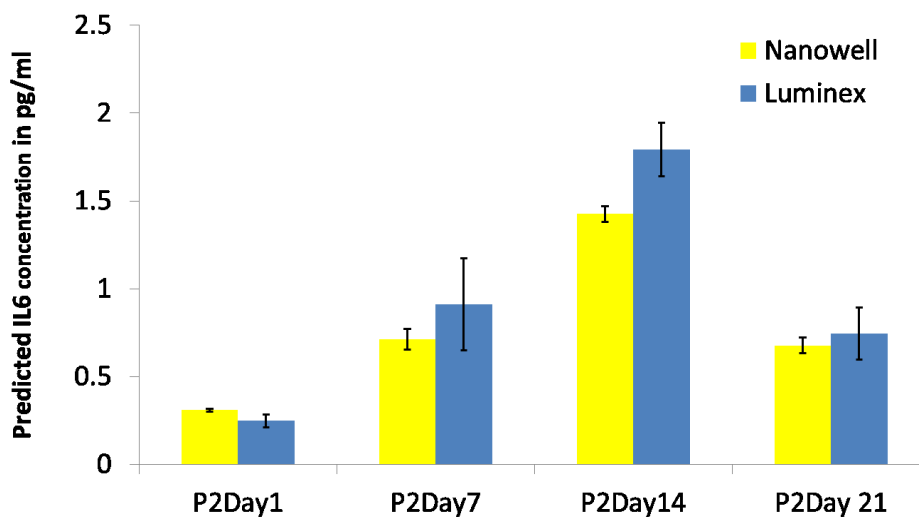


Figure 6-14 Comparison of nanowell sensor and Luminex

Figures 6-15, 6-16, and 6-17 show a comparison of predicted TNF- α , IL-6, and IL-10 levels of the stim and sham groups.

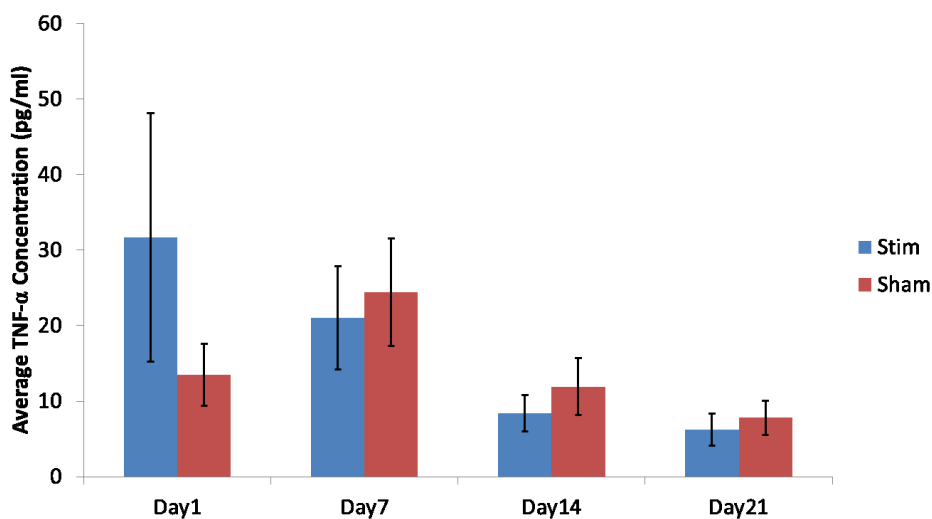


Figure 6-15 Comparison of TNF- α concentration of stim and sham group

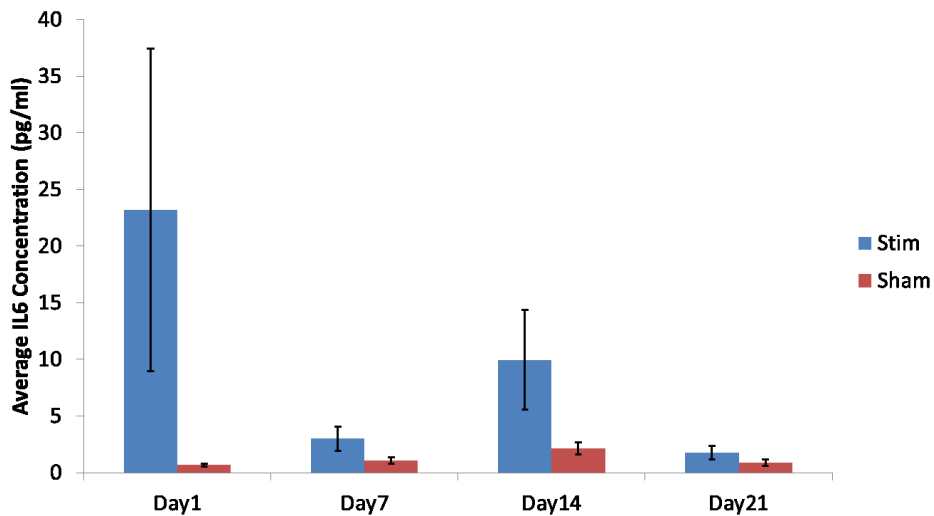


Figure 6-16 Comparison of IL6 concentration of stim and sham group

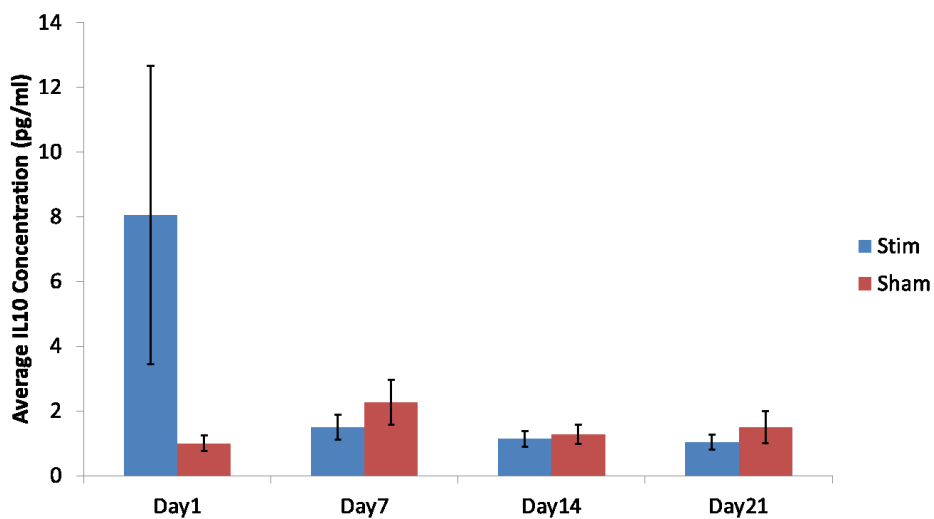


Figure 6-17 Comparison of IL10 concentration of stim and sham group

Figures 6-18, 6-19, and 6-20 show a comparison of predicted TNF- α , IL-6, and IL-10 levels for the different techniques.

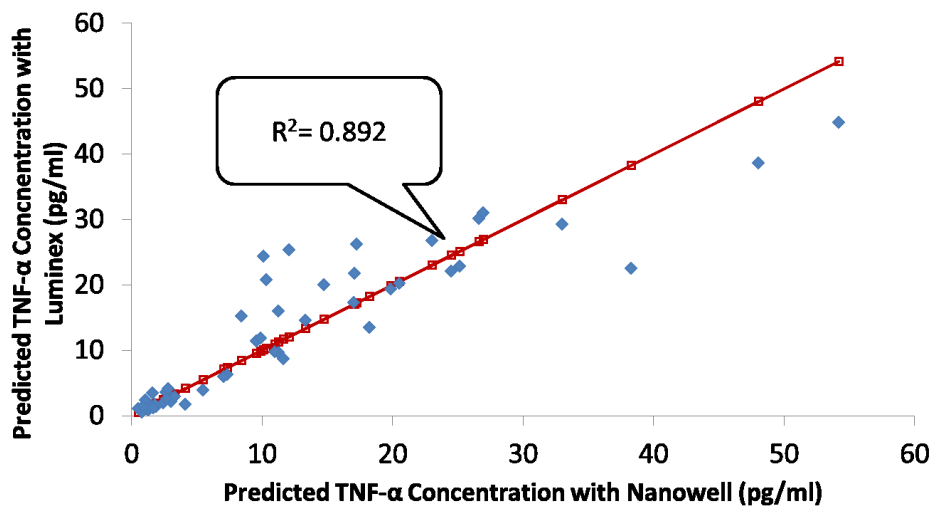


Figure 6-18 Correlation between nanowell sensor and Luminex of TNF- α

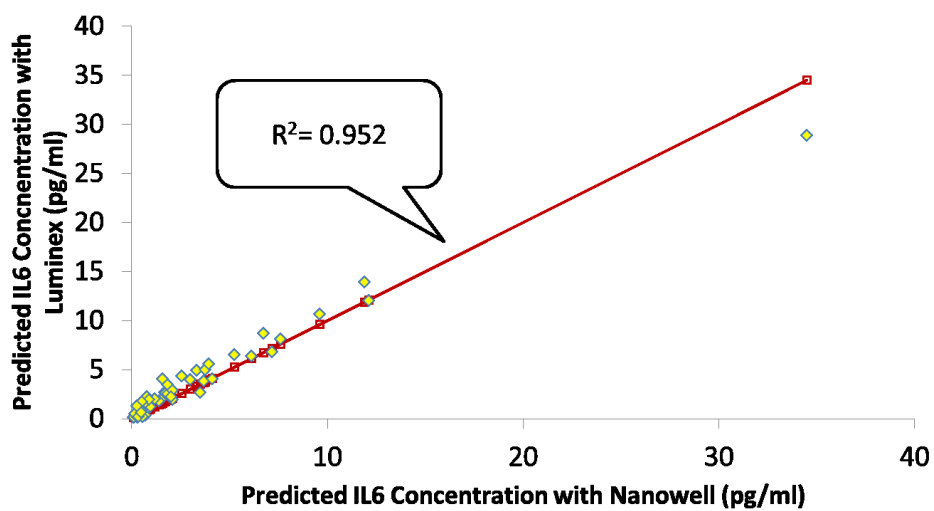


Figure 6-19 Correlation between nanowell sensor and Luminex of IL6

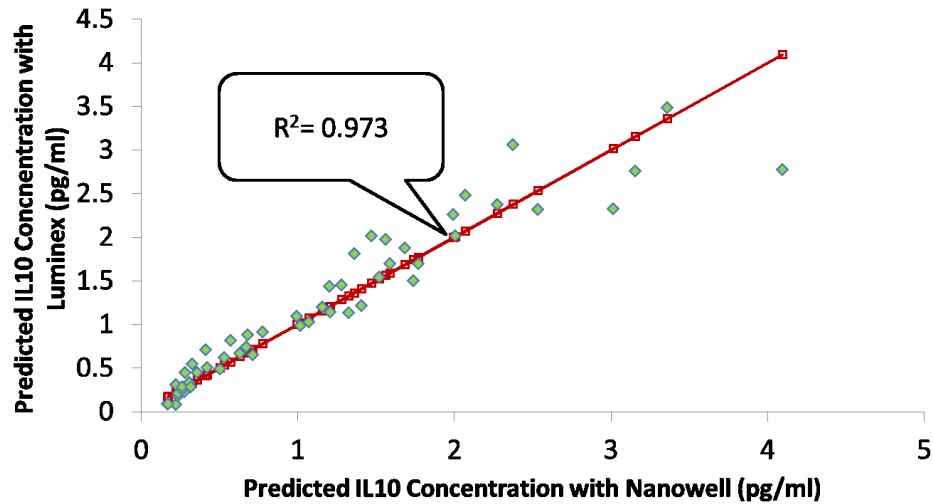


Figure 6-20 Correlation between nanowell sensor and Luminex of IL10

For all three cytokines, the nanowell sensing technique and the Luminex technique showed a high correlation, which indicates the two techniques are comparable and of the same quality.

6.4 Conclusion

We performed a series of experiments on samples from patients with inflammatory arthritis. The titration curves of three different proteins, TNF- α , IL-6, and IL-10, were acquired for both the nanowell sensor technique and the Luminex technique. Following the formula to calculate the target protein concentration, with knowing the nanowell sensor response or Luminex MFI counts, were derived based on the regression model and simulation. The results showed a down to single pg/ml quantification of nanowell sensor, and a good correlation curve to the gold standard Luminex technique, for all three types of cytokines. The study shows that the cytokine levels of patients changed due to their treatment therapies and curing

process, which proves that the nanowell sensor technique is a good candidate for quantifying cytokine levels accurately and rapidly.

Chapter 7: Conclusion and future works

In conclusion, we have designed, fabricated, and validated a sensor array platform with the ability of time multiplex, analysis of more than 10 types of target cytokines. Our experimental results show that repeatable and reliable titration curves of different target proteins in different serum matrixes of both the human and animal kind of concentration down to pg/ml, which is comparable to the gold standard ELISA method. The platform also enables a long time continuous monitoring function of the technique. The response to target proteins with different concentrations shows a linear increase with increasing concentrations. Using the combination of the implement of the system with an embedded microcontroller and the nanowell sensor array, we were able to qualify three different target proteins in serum within 10 minutes. Although in this work, certain proteins were used as biomarkers for testing in multiple samples, we emphasize that this method can be used to detect a wide variety of proteins as long as a comparable high-affinity antibody pair is available.

Our next focus will be integrating and expanding the system, pushing the lower detection limits, seeking a larger dynamic range, and applying more different types of target cytokines. After the characterization of certain concentrations of target proteins, we will apply the technique with some clinical utilities, even for in vivo measurements.

References:

- [1] D. Pacheco-Alvarez, R. S. Solórzano-Vargas, and A. L. Del Río, “Biotin in metabolism and its relationship to human disease,” *Arch. Med. Res.*, vol. 33, no. 5, pp. 439–447, 2002, doi: 10.1016/S0188-4409(02)00399-5.
- [2] L. Fucci, C. N. Oliver, M. J. Coon, and E. R. Stadtman, “Inactivation of key metabolic enzymes by mixed function oxidation reactions: possible implication in protein turnover and ageing,” *Proc. Natl. Acad. Sci. U. S. A.*, vol. 80, no. 6 I, pp. 1521–1525, 1983, doi: 10.1073/pnas.80.6.1521.
- [3] R. P. Nagarkar, S. E. Miller, S. Zhong, D. J. Pochan, and J. P. Schneider, “Dynamic protein folding at the surface of stimuli-responsive peptide fibrils,” *Protein Sci.*, vol. 27, no. 7, pp. 1243–1251, 2018, doi: 10.1002/pro.3394.
- [4] M. S. Wold, “REPLICATION PROTEIN A:A Heterotrimeric, Single-Stranded DNA-Binding Protein Required for Eukaryotic DNA Metabolism,” *Annu. Rev. Biochem.*, vol. 66, no. 1, pp. 61–92, 1997, doi: 10.1146/annurev.biochem.66.1.61.
- [5] C. O. Pabo and R. T. Sauer, “Transcription Factors: Structural Families and Principles of DNA Recognition,” *Annu. Rev. Biochem.*, 1992, doi: 10.1146/annurev.bi.61.070192.005201.
- [6] G. W. Hatfield and D. A. Roth, “Optimizing scaleup yield for protein production: Computationally Optimized DNA Assembly (CODA) and Translation Engineering™,” *Biotechnology Annual Review*. 2007, doi: 10.1016/S1387-2656(07)13002-7.
- [7] K. Ohe, E. Lalli, and P. Sassone-Corsi, “A direct role of SRY and SOX: Proteins in pre-mRNA splicing,” *Proc. Natl. Acad. Sci. U. S. A.*, 2002, doi: 10.1073/pnas.022645899.
- [8] D. Dubnau, “Binding and transport of transforming DNA by *Bacillus subtilis*: The role of type-IV pilin-like proteins - A review,” in *Gene*, 1997, doi: 10.1016/S0378-1119(96)00804-9.
- [9] J. W. Harbour and D. C. Dean, “Rb function in cell-cycle regulation and apoptosis,” *Nature Cell Biology*. 2000, doi: 10.1038/35008695.
- [10] D. A. Dartt, “Signal transduction and control of lacrimal Gland protein secretion: A review,” *Current Eye Research*. 1989, doi: 10.3109/02713688908995762.
- [11] J. V. Olsen *et al.*, “Global, In Vivo, and Site-Specific Phosphorylation Dynamics in Signaling Networks,” *Cell*, 2006, doi: 10.1016/j.cell.2006.09.026.
- [12] T. Köcher and G. Superti-Furga, “Mass spectrometry-based functional proteomics: From molecular machines to protein networks,” *Nature Methods*. 2007, doi: 10.1038/nmeth1093.
- [13] A. Belle, A. Tanay, L. Bitincka, R. Shamir, and E. K. O’Shea, “Quantification of protein half-lives in the budding yeast proteome,” *Proc. Natl. Acad. Sci. U. S. A.*, 2006, doi: 10.1073/pnas.0605420103.
- [14] Y. Ishihama *et al.*, “Exponentially modified protein abundance index (emPAI) for estimation of absolute protein amount in proteomics by the number of sequenced peptides per protein,” *Mol. Cell. Proteomics*, 2005, doi:

- 10.1074/mcp.M500061-MCP200.
- [15] B. Blagoev, I. Kratchmarova, S. E. Ong, M. Nielsen, L. J. Foster, and M. Mann, "A proteomics strategy to elucidate functional protein-protein interactions applied to EGF signaling," *Nat. Biotechnol.*, 2003, doi: 10.1038/nbt790.
- [16] F. M. Boisvert, Y. W. Lam, D. Lamont, and A. I. Lamond, "A quantitative proteomics analysis of subcellular proteome localization and changes induced by DNA damage," *Mol. Cell. Proteomics*, 2010, doi: 10.1074/mcp.M900429-MCP200.
- [17] G. T. Hanson *et al.*, "Investigating Mitochondrial Redox Potential with Redox-sensitive Green Fluorescent Protein Indicators," *J. Biol. Chem.*, 2004, doi: 10.1074/jbc.M312846200.
- [18] J. C. Moore, J. W. DeVries, M. Lipp, J. C. Griffiths, and D. R. Abernethy, "Total protein methods and their potential utility to reduce the risk of food protein adulteration," *Comprehensive Reviews in Food Science and Food Safety*. 2010, doi: 10.1111/j.1541-4337.2010.00114.x.
- [19] G. Marko-Varga, J. Nilsson, and T. Laurell, "New directions of miniaturization within the proteomics research area," *Electrophoresis*. 2003, doi: 10.1002/elps.200305666.
- [20] G. A. Marko-Varga, J. Nilsson, and T. Laurell, "New directions of miniaturization within the biomarker research area," *Electrophoresis*. 2004, doi: 10.1002/elps.200406109.
- [21] X. Li, E. A. Foley, K. R. Molloy, Y. Li, B. T. Chait, and T. M. Kapoor, "Quantitative chemical proteomics approach to identify post-translational modification-mediated protein-protein interactions," *J. Am. Chem. Soc.*, 2012, doi: 10.1021/ja210528v.
- [22] T. Sayd *et al.*, "Proteome analysis of the sarcoplasmic fraction of pig Semimembranosus muscle: Implications on meat color development," *J. Agric. Food Chem.*, 2006, doi: 10.1021/jf052569v.
- [23] M. Pompa, M. M. Giuliani, C. Palermo, F. Agriesti, D. Centonze, and Z. Flagella, "Comparative analysis of gluten proteins in three durum wheat cultivars by a proteomic approach," *J. Agric. Food Chem.*, 2013, doi: 10.1021/jf304566d.
- [24] R. Gupta and S. Brunak, "Prediction of glycosylation across the human proteome and the correlation to protein function.," *Pac. Symp. Biocomput.*, 2002, doi: 10.1142/9789812799623_0029.
- [25] B. Thiede *et al.*, "Peptide mass fingerprinting," *Methods*, 2005, doi: 10.1016/j.ymeth.2004.08.015.
- [26] D. C. Chamrad, G. Körting, K. Stühler, H. E. Meyer, J. Klose, and M. Blüggel, "Evaluation of algorithms for protein identification from sequence databases using mass spectrometry data," *Proteomics*, 2004, doi: 10.1002/pmic.200300612.
- [27] M. Mann and O. N. Jensen, "Proteomic analysis of post-translational modifications," *Nature Biotechnology*. 2003, doi: 10.1038/nbt0303-255.
- [28] N. Blom, T. Sicheritz-Pontén, R. Gupta, S. Gammeltoft, and S. Brunak, "Prediction of post-translational glycosylation and phosphorylation of proteins

- from the amino acid sequence,” *Proteomics*. 2004, doi: 10.1002/pmic.200300771.
- [29] R. E. Higgs, M. D. Knierman, V. Gelfanova, J. P. Butler, and J. E. Hale, “Comprehensive label-free method for the relative quantification of proteins from biological samples,” *J. Proteome Res.*, 2005, doi: 10.1021/pr050109b.
- [30] G. Van Den Bergh and L. Arckens, “Fluorescent two-dimensional difference gel electrophoresis unveils the potential of gel-based proteomics,” *Current Opinion in Biotechnology*. 2004, doi: 10.1016/j.copbio.2003.12.001.
- [31] R. Marouga, S. David, and E. Hawkins, “The development of the DIGE system: 2D fluorescence difference gel analysis technology,” *Analytical and Bioanalytical Chemistry*. 2005, doi: 10.1007/s00216-005-3126-3.
- [32] K. Petritis *et al.*, “Improved peptide elution time prediction for reversed-phase liquid chromatography-MS by incorporating peptide sequence information,” *Anal. Chem.*, 2006, doi: 10.1021/ac060143p.
- [33] P. Picotti *et al.*, “High-throughput generation of selected reaction-monitoring assays for proteins and proteomes,” *Nat. Methods*, 2010, doi: 10.1038/nmeth.1408.
- [34] Z. Roth, G. Yehezkel, and I. Khalaila, “Identification and Quantification of Protein Glycosylation,” *Int. J. Carbohydr. Chem.*, 2012, doi: 10.1155/2012/640923.
- [35] M. Vaudel, A. Sickmann, and L. Martens, “Peptide and protein quantification: A map of the minefield,” *Proteomics*. 2010, doi: 10.1002/pmic.200900481.
- [36] S. Feng, S. Sekine, V. Pessino, H. Li, M. D. Leonetti, and B. Huang, “Improved split fluorescent proteins for endogenous protein labeling,” *Nat. Commun.*, 2017, doi: 10.1038/s41467-017-00494-8.
- [37] K. Gevaert, F. Impens, B. Ghesquière, P. Van Damme, A. Lambrechts, and J. Vandekerckhove, “Stable isotopic labeling in proteomics,” *Proteomics*. 2008, doi: 10.1002/pmic.200800421.
- [38] T. Anabuki, M. Tsukahara, H. Matsuura, and K. Takahashi, “Tandem photoaffinity labeling of a target protein using a linker with biotin, alkyne and benzophenone groups and a bioactive small molecule with an azide group,” *Biosci. Biotechnol. Biochem.*, 2016, doi: 10.1080/09168451.2015.1104240.
- [39] I. Chen, M. Howarth, W. Lin, and A. Y. Ting, “Site-specific labeling of cell surface proteins with biophysical probes using biotin ligase,” *Nat. Methods*, 2005, doi: 10.1038/nmeth735.
- [40] M. E. Aubin-Tam, W. Hwang, and K. Hamad-Schifferli, “Site-directed nanoparticle labeling of cytochrome c,” *Proc. Natl. Acad. Sci. U. S. A.*, 2009, doi: 10.1073/pnas.0807299106.
- [41] K. A. Neilson *et al.*, “Less label, more free: Approaches in label-free quantitative mass spectrometry,” *Proteomics*. 2011, doi: 10.1002/pmic.201000553.
- [42] P. S. Waggoner and H. G. Craighead, “Micro- and nanomechanical sensors for environmental, chemical, and biological detection,” *Lab Chip*, 2007, doi: 10.1039/b707401h.
- [43] G. N. M. Ferreira, A. C. da-Silva, and B. Tomé, “Acoustic wave biosensors: physical models and biological applications of quartz crystal microbalance,”

- Trends in Biotechnology*. 2009, doi: 10.1016/j.tibtech.2009.09.003.
- [44] J. Homola, "Present and future of surface plasmon resonance biosensors," *Analytical and Bioanalytical Chemistry*. 2003, doi: 10.1007/s00216-003-2101-0.
- [45] B. Sepúlveda, P. C. Angelomé, L. M. Lechuga, and L. M. Liz-Marzán, "LSPR-based nanobiosensors," *Nano Today*. 2009, doi: 10.1016/j.nantod.2009.04.001.
- [46] S. Watanabe, K. Usui, K. Y. Tomizaki, K. Kajikawa, and H. Mihara, "Anomalous reflection of gold applicable for a practical protein-detecting chip platform," *Mol. Biosyst.*, 2005, doi: 10.1039/b513075c.
- [47] B.-Y. Chang and S.-M. Park, "Electrochemical impedance spectroscopy of composite adhesive joints," *Annu. Rev. Anal. Chem. (Palo Alto, Calif.)*, vol. 3, no. 6, pp. 207–229, 2010, doi: 10.1146/annurev.anchem.012809.102211.
- [48] F. Ciucci, "Modeling electrochemical impedance spectroscopy," *Current Opinion in Electrochemistry*. 2019, doi: 10.1016/j.coelec.2018.12.003.
- [49] X. Liu, J. Xiong, Y. Lv, and Y. Zuo, "Study on corrosion electrochemical behavior of several different coating systems by EIS," *Prog. Org. Coatings*, 2009, doi: 10.1016/j.porgcoat.2008.08.012.
- [50] B. R. Hinderliter, S. G. Croll, D. E. Tallman, Q. Su, and G. P. Bierwagen, "Interpretation of EIS data from accelerated exposure of coated metals based on modeling of coating physical properties," *Electrochim. Acta*, 2006, doi: 10.1016/j.electacta.2005.12.047.
- [51] Z. Deng, Z. Zhang, Y. Lai, J. Liu, J. Li, and Y. Liu, "Electrochemical Impedance Spectroscopy Study of a Lithium/Sulfur Battery: Modeling and Analysis of Capacity Fading," *J. Electrochem. Soc.*, 2013, doi: 10.1149/2.026304jes.
- [52] J. M. Hu, J. Q. Zhang, and C. N. Cao, "Oxygen evolution reaction on IrO₂-based DSA® type electrodes: Kinetics analysis of Tafel lines and EIS," *Int. J. Hydrogen Energy*, 2004, doi: 10.1016/j.ijhydene.2003.09.007.
- [53] C. C. Hu and C. H. Chu, "Electrochemical impedance characterization of polyaniline-coated graphite electrodes for electrochemical capacitors - Effects of film coverage/thickness and anions," *J. Electroanal. Chem.*, 2001, doi: 10.1016/S0022-0728(01)00385-0.
- [54] R. Radhakrishnan, I. I. Suni, C. S. Bever, and B. D. Hammock, "Impedance biosensors: Applications to sustainability and remaining technical challenges," *ACS Sustain. Chem. Eng.*, vol. 2, no. 7, pp. 1649–1655, 2014, doi: 10.1021/sc500106y.
- [55] S. J. Wilks, T. J. Richner, S. K. Brodnick, D. R. Kipke, J. C. Williams, and K. J. Otto, "Voltage biasing, cyclic voltammetry, & electrical impedance spectroscopy for neural interfaces," *J. Vis. Exp.*, 2012, doi: 10.3791/3566.
- [56] E. B. Bahadir and M. K. Sezginürk, "A review on impedimetric biosensors," *Artif. Cells, Nanomedicine Biotechnol.*, vol. 44, no. 1, pp. 248–262, 2016, doi: 10.3109/21691401.2014.942456.
- [57] S. Ray, G. Mehta, and S. Srivastava, "Label-free detection techniques for protein microarrays: Prospects, merits and challenges," *Proteomics*, vol. 10, no. 4, pp. 731–748, 2010, doi: 10.1002/pmic.200900458.
- [58] M. E. Hudson, I. Pozdnyakova, K. Haines, G. Mor, and M. Snyder,

- “Identification of differentially expressed proteins in ovarian cancer using high-density protein microarrays,” *Proc. Natl. Acad. Sci. U. S. A.*, vol. 104, no. 44, pp. 17494–9, 2007, doi: 10.1073/pnas.0708572104.
- [59] B. Schweitzer, P. Predki, and M. Snyder, “Microarrays to characterize protein interactions on a whole-proteome scale,” *Proteomics*, vol. 3, no. 11, pp. 2190–2199, 2003, doi: 10.1002/pmic.200300610.
- [60] B. Kersten, A. Possling, F. Blaesing, E. Mirgorodskaya, J. Gobom, and H. Seitz, “Protein microarray technology and ultraviolet crosslinking combined with mass spectrometry for the analysis of protein-DNA interactions,” *Anal. Biochem.*, vol. 331, no. 2, pp. 303–313, 2004, doi: 10.1016/j.ab.2004.05.008.
- [61] I. Chamritski, M. Clarkson, J. Franklin, and S. W. Li, “Real-time detection of antigen-antibody reactions by imaging ellipsometry,” *Aust. J. Chem.*, vol. 60, no. 9, pp. 667–671, 2007, doi: 10.1071/CH07115.
- [62] X. Yu, D. Xu, and Q. Cheng, “Label-free detection methods for protein microarrays,” *Proteomics*, vol. 6, no. 20, pp. 5493–5503, 2006, doi: 10.1002/pmic.200600216.
- [63] B. B. Haab, “Methods and applications of antibody microarrays in cancer research,” *Proteomics*, vol. 3, no. 11, pp. 2116–2122, 2003, doi: 10.1002/pmic.200300595.
- [64] G. Zheng, F. Patolsky, Y. Cui, W. U. Wang, and C. M. Lieber, “Multiplexed electrical detection of cancer markers with nanowire sensor arrays,” *Nat. Biotechnol.*, vol. 23, no. 10, pp. 1294–1301, 2005, doi: 10.1038/nbt1138.
- [65] A. M. Armani, R. P. Kulkarni, S. E. Fraser, R. C. Flagan, and K. J. Vahala, “Label-free, single-molecule detection with optical microcavities,” *Science (80-.)*, 2007, doi: 10.1126/science.1145002.
- [66] M. L. Sin, K. E. Mach, P. K. Wong, and J. C. Liao, “Advances and challenges in biosensor-based diagnosis of infectious diseases,” *Expert Review of Molecular Diagnostics*. 2014, doi: 10.1586/14737159.2014.888313.
- [67] J. H. T. Luong, K. B. Male, and J. D. Glennon, “Biosensor technology: Technology push versus market pull,” *Biotechnology Advances*. 2008, doi: 10.1016/j.biotechadv.2008.05.007.
- [68] M. Fivash, E. M. Towler, and R. J. Fisher, “BIAcore for macromolecular interaction,” *Curr. Opin. Biotechnol.*, 1998, doi: 10.1016/S0958-1669(98)80091-8.
- [69] J. Concepcion *et al.*, “Label-Free Detection of Biomolecular Interactions Using BioLayer Interferometry for Kinetic Characterization,” *Comb. Chem. High Throughput Screen.*, 2009, doi: 10.2174/138620709789104915.
- [70] L. Liu *et al.*, “Comparison of next-generation sequencing systems,” *Journal of Biomedicine and Biotechnology*. 2012, doi: 10.1155/2012/251364.
- [71] R. Esfandyarpour, M. Javanmard, Z. Koochak, H. Esfandyarpour, J. S. Harris, and R. W. Davis, “Label-free electronic probing of nucleic acids and proteins at the nanoscale using the nanoneedle biosensor,” *Biomicrofluidics*, 2013, doi: 10.1063/1.4817771.
- [72] N. Gao, W. Zhou, X. Jiang, G. Hong, T. M. Fu, and C. M. Lieber, “General strategy for biodetection in high ionic strength solutions using transistor-based nanoelectronic sensors,” *Nano Lett.*, 2015, doi: 10.1021/acs.nanolett.5b00133.

- [73] S. Das, H. Vikalo, and A. Hassibi, "On scaling laws of biosensors: A stochastic approach," *J. Appl. Phys.*, 2009, doi: 10.1063/1.3116125.
- [74] Z. Chen *et al.*, "Protein microarrays with carbon nanotubes as multicolor Raman labels," *Nat. Biotechnol.*, vol. 26, no. 11, pp. 1285–1292, 2008, doi: 10.1038/nbt.1501.
- [75] Q. Yu and G. Golden, "Probing the protein orientation on charged self-assembled monolayers on gold nanohole arrays by SERS," *Langmuir*, 2007, doi: 10.1021/la7007073.
- [76] P. Actis, A. C. Mak, and N. Pourmand, "Functionalized nanopipettes: Toward label-free, single cell biosensors," *Bioanal. Rev.*, 2010, doi: 10.1007/s12566-010-0013-y.
- [77] P. R. Srinivas, S. Srivastava, S. Hanash, and J. Wright, "Proteomics in early detection of cancer," in *Clinical Chemistry*, 2001, doi: 10.1093/clinchem/47.10.1901.
- [78] M. F. Lopez *et al.*, "A novel, high-throughput workflow for discovery and identification of serum carrier protein-bound peptide biomarker candidates in ovarian cancer samples," *Clin. Chem.*, 2007, doi: 10.1373/clinchem.2006.080721.
- [79] E. Gorelik *et al.*, "Multiplexed immunobead-based cytokine profiling for early detection of ovarian cancer," *Cancer Epidemiol. Biomarkers Prev.*, 2005, doi: 10.1158/1055-9965.EPI-04-0404.
- [80] Y. Zheng *et al.*, "A multiparametric panel for ovarian cancer diagnosis, prognosis, and response to chemotherapy," *Clin. Cancer Res.*, 2007, doi: 10.1158/1078-0432.CCR-07-1409.
- [81] O. Poetz *et al.*, "Protein microarrays for antibody profiling: Specificity and affinity determination on a chip," in *Proteomics*, 2005, doi: 10.1002/pmic.200401299.
- [82] P. Mitchell, "A perspective on protein microarrays," *Nature Biotechnology*. 2002, doi: 10.1038/nbt0302-225.
- [83] S. M. Chan, J. Ermann, L. Su, C. G. Fathman, and P. J. Utz, "Protein microarrays for multiplex analysis of signal transduction pathways," *Nat. Med.*, 2004, doi: 10.1038/nm1139.
- [84] M. Shingyoji, D. Gerion, D. Pinkel, J. W. Gray, and F. Chen, "Quantum dots-based reverse phase protein microarray," *Talanta*, 2005, doi: 10.1016/j.talanta.2005.06.064.
- [85] G. Zheng, F. Patolsky, Y. Cui, W. U. Wang, and C. M. Lieber, "Multiplexed electrical detection of cancer markers with nanowire sensor arrays," *Nat. Biotechnol.*, 2005, doi: 10.1038/nbt1138.
- [86] H. F. Ji, H. Gao, K. R. Buchapudi, X. Yang, X. Xu, and M. K. Schulte, "Microcantilever biosensors based on conformational change of proteins," *Analyst*. 2008, doi: 10.1039/b713330h.
- [87] S. Ghosh, A. K. Sood, and N. Kumar, "Carbon nanotube flow sensors," *Science (80-.)*, 2003, doi: 10.1126/science.1079080.
- [88] M. Pumera, S. Sánchez, I. Ichinose, and J. Tang, "Electrochemical nanobiosensors," *Sensors and Actuators, B: Chemical*. 2007, doi: 10.1016/j.snb.2006.11.016.

- [89] R. S. Gaster *et al.*, “Matrix-insensitive protein assays push the limits of biosensors in medicine,” *Nat. Med.*, vol. 15, no. 11, pp. 1327–1332, 2009, doi: 10.1038/nm.2032.
- [90] F. B. Myers and L. P. Lee, “Innovations in optical microfluidic technologies for point-of-care diagnostics,” *Lab on a Chip*. 2008, doi: 10.1039/b812343h.
- [91] B. Kuswandi, Nuriman, J. Huskens, and W. Verboom, “Optical sensing systems for microfluidic devices: A review,” *Analytica Chimica Acta*. 2007, doi: 10.1016/j.aca.2007.08.046.
- [92] B. Weigl, G. Domingo, P. LaBarre, and J. Gerlach, “Towards non- and minimally instrumented, microfluidics-based diagnostic devices,” *Lab on a Chip*. 2008, doi: 10.1039/b811314a.
- [93] N. Gao *et al.*, “Specific detection of biomolecules in physiological solutions using graphene transistor biosensors,” *Proc. Natl. Acad. Sci. U. S. A.*, 2016, doi: 10.1073/pnas.1625010114.
- [94] X. Lin, C. Cheng, P. Terry, J. Chen, H. Cui, and J. Wu, “Rapid and sensitive detection of bisphenol a from serum matrix,” *Biosens. Bioelectron.*, 2017, doi: 10.1016/j.bios.2016.12.024.
- [95] X. Duan, Y. Li, N. K. Rajan, D. A. Routenberg, Y. Modis, and M. A. Reed, “Quantification of the affinities and kinetics of protein interactions using silicon nanowire biosensors,” *Nat. Nanotechnol.*, 2012, doi: 10.1038/nnano.2012.82.
- [96] S. Friedenauer and H. H. Berlet, “Sensitivity and variability of the Bradford protein assay in the presence of detergents,” *Anal. Biochem.*, 1989, doi: 10.1016/0003-2697(89)90636-2.
- [97] Y. A. Levine *et al.*, “Neurostimulation of the cholinergic anti-inflammatory pathway ameliorates disease in rat collagen-induced arthritis,” *PLoS One*, 2014, doi: 10.1371/journal.pone.0104530.
- [98] J. A. Singh *et al.*, “2015 American College of Rheumatology Guideline for the Treatment of Rheumatoid Arthritis,” *Arthritis Care Res. (Hoboken)*., 2016, doi: 10.1002/acr.22783.
- [99] L. V. Borovikova *et al.*, “Vagus nerve stimulation attenuates the systemic inflammatory response to endotoxin,” *Nature*, 2000, doi: 10.1038/35013070.
- [100] F. O. The *et al.*, “Central activation of the cholinergic anti-inflammatory pathway reduces surgical inflammation in experimental post-operative ileus,” *Br. J. Pharmacol.*, 2011, doi: 10.1111/j.1476-5381.2011.01296.x.
- [101] D. P. Zachs *et al.*, “Noninvasive ultrasound stimulation of the spleen to treat inflammatory arthritis,” *Nat. Commun.*, 2019, doi: 10.1038/s41467-019-08721-0.
- [102] U. Andersson and K. J. Tracey, “Neural reflexes in inflammation and immunity,” *Journal of Experimental Medicine*. 2012, doi: 10.1084/jem.20120571.
- [103] M. A. van Maanen, M. J. Vervoordeldonk, and P. P. Tak, “The cholinergic anti-inflammatory pathway: Towards innovative treatment of rheumatoid arthritis,” *Nat. Rev. Rheumatol.*, 2009, doi: 10.1038/nrrheum.2009.31.
- [104] F. A. Koopman *et al.*, “Vagus nerve stimulation inhibits cytokine production and attenuates disease severity in Rheumatoid arthritis,” *Proc. Natl. Acad. Sci.*

- U. S. A.*, 2016, doi: 10.1073/pnas.1605635113.
- [105] J. C. Gigliotti *et al.*, “Ultrasound prevents renal ischemia-reperfusion injury by stimulating the splenic cholinergic anti-inflammatory pathway,” *J. Am. Soc. Nephrol.*, 2013, doi: 10.1681/ASN.2013010084.
- [106] C. J. Wright, J. Rothwell, and N. Saffari, “Ultrasonic stimulation of peripheral nervous tissue: An investigation into mechanisms,” in *Journal of Physics: Conference Series*, 2015, doi: 10.1088/1742-6596/581/1/012003.
- [107] J. F. Rossi, Z. Y. Lu, M. Jourdan, and B. Klein, “Interleukin-6 as a therapeutic target,” *Clinical Cancer Research*. 2015, doi: 10.1158/1078-0432.CCR-14-2291.
- [108] P. C. Ng *et al.*, “Proinflammatory and anti-inflammatory cytokine responses in preterm infants with systemic infections,” *Arch. Dis. Child. Fetal Neonatal Ed.*, 2003, doi: 10.1136/fn.88.3.f209.
- [109] J. R. Bradley, “TNF-mediated inflammatory disease,” *Journal of Pathology*. 2008, doi: 10.1002/path.2287.
- [110] H. Ishii and M. Yoshida, “Inflammatory cytokines,” *Nippon rinsho. Japanese journal of clinical medicine*. 2010, doi: 10.1007/978-1-4939-7101-5_302.
- [111] N. Turan *et al.*, “IL-6 pathway upregulation in subgroup of severe asthma is associated with neutrophilia and poor lung function,” *Clinical and Experimental Allergy*. 2018, doi: 10.1111/cea.13085.
- [112] P. L. dos Santos *et al.*, “The Severity of Visceral Leishmaniasis Correlates with Elevated Levels of Serum IL-6, IL-27 and sCD14,” *PLoS Negl. Trop. Dis.*, 2016, doi: 10.1371/journal.pntd.0004375.
- [113] S. Srirangan and E. H. Choy, “The role of Interleukin 6 in the pathophysiology of rheumatoid arthritis,” *Therapeutic Advances in Musculoskeletal Disease*. 2010, doi: 10.1177/1759720X10378372.
- [114] C. K. Wong *et al.*, “Plasma inflammatory cytokines and chemokines in severe acute respiratory syndrome,” *Clin. Exp. Immunol.*, 2004, doi: 10.1111/j.1365-2249.2004.02415.x.
- [115] C. K. Min *et al.*, “Comparative and kinetic analysis of viral shedding and immunological responses in MERS patients representing a broad spectrum of disease severity,” *Sci. Rep.*, 2016, doi: 10.1038/srep25359.
- [116] D. McGonagle, K. Sharif, A. O’Regan, and C. Bridgewood, “The Role of Cytokines including Interleukin-6 in COVID-19 induced Pneumonia and Macrophage Activation Syndrome-Like Disease,” *Autoimmunity Reviews*. 2020, doi: 10.1016/j.autrev.2020.102537.